2016

Nano Cost Nano Patterned Template for Surface Enhanced Raman Scattering (SERS) for IN-VITRO and IN-VIVO Applications

Hsuan-Chao Hou
Louisiana State University and Agricultural and Mechanical College

NANO COST NANO PATTERNED TEMPLATE FOR SURFACE ENHANCED RAMAN SCATTERING (SERS) FOR IN-VITRO AND IN-VIVO APPLICATIONS

A Dissertation

Submitted to the Graduate Faculty of the
Louisiana State University and
Agricultural and Mechanical College
in partial fulfillment of the
requirements for the degree of
Doctor of Philosophy

in

Division of Electrical and Computer Engineering
The School of Electrical Engineering and Computer Engineering

by
Hsuan-Chao Hou
B.S., Huafan, 2004
M.S., Feng Chia University, 2007
M.S., Louisiana State University 2015
August 2016

ACKNOWLEDGEMENTS

I would like to dedicate this dissertation to my lovely HOU family who has been the greatest metal and physical support of my strength in this journey. Without their spiritual support, this work would not be able to complete. I am grateful for their infinite love, patience and concern throughout these years. I love you, Mom, Dad and sisters.

I would like to express my gratitude to Dr Martin Feldman, my research advisor, for all advice, guidance and support throughout the entire Ph.D. program. I can not finish this dissertation without Dr Feldman (Marty). His methods to solve the problems are very intelligent and unique. His perspective has enriched my knowledge in optical and micro-electro-mechanical systems (MEMS) fields.

I feel truly honor to have Dr. Theda Daniels-Race, Dr. Kidong Park, Dr. Georgios Veronis, and Dr. Graca Vicente in my committee. Dr. Race is one of the great professors I have ever met in my life. She not only gives me academic advice but also cares about student's life. Dr. Park has given me a lot of knowledge for both lecture and research. I am thankful to Dr. Veronis and Dr. Vicente. Their receptive nature makes my interaction with them very comfortable.

I am thankful to Mr. Chris O'Laughlin for the years of technical support at EMDL. I would like to thank my group members: Dr. Daniel Herbert, Dr. Kim and Ms. Srismrita Basu for all the discussion and friendship. I am grateful to Dr. Kanakamedia, and Ms. Madhavi Divakar for the atomic force microscopy (AFM) scanning. I would like to acknowledge Dr. Sarkar and Mr. Subhodip Maulik for technical discussion. Last, I would like to appreciate all the people who have provided assistance to this research.

I am grateful to department of Division of Electrical and Computer Engineering of the School of Electrical Engineering and Computer Engineering for the financial support, especially the James R. Lewis Scholarship, Division of Electrical & Computer Engineering in 2014. This research partial was partially supported in by National Institutes of Health (NIH – R03EB012519-01A1). The majority of this work has been performed through both Electronic Material Device Laboratory (EMDL) at Electrical Engineering Department and Center for Advanced Microstructures and Devices (CAMD) at Louisiana State University.

TABLE OF CONTENTS

LIST OF TABLES

LIST OF FIGURES

ABSTRACT

Raman scattering is a well-known technique for detecting and identifying complex molecular level samples. The weak Raman signals are enormously enhanced in the presence of a nano-patterned metallic surface next to the specimens. This dissertation describes a technique to fabricate a novel, low cost, high sensitive, disposable, and reproducible metallic nanostructure on a transparent substrate for Surface Enhanced Raman Scattering (SERS). Raman signals can be obtained from the specimen surface of opaque specimens. Most importantly, the metallic nanostructure can be bonded on the end of a probe / a needle, and the other end is coupled to a distant spectrometer. This opens up the Raman spectroscopy for a use in a clinical environment with the patient simply sitting or lying near a spectrometer.

This SERS system, one of molecular level early diagnosis technologies, can be divided into four parts: SERS nanostructure substrates, reflection Raman signal (*in vitro*), transmission (*in vivo*) Raman signal, and a probe / a needle with a gradient-index (GRIN) lens in an articulated arm system. In this work, the aluminum metal was employed as not only a base substrate for a sputtered Au nanostructure (conventional view) but also a sacrificial layer for the Au nanostructure on a transparent substrate (transmission view). The enhanced Raman Signal from reflection and transparent SERS substrates depended on aluminum etching methods, Au deposition angles, and Au deposition thicknesses. Rhodamine 6G solutions on both sides of the SERS substrates were used to analyze and characterize. Moreover, preliminary Raman Spectra from R6G and chicken specimen were obtained through a remote SERS probe head and an articulated arm system. The diameter of the invasive probe head was shrunk to 0.5 mm. The implication is that this system can be applied in medical applications.

CHAPTER 1: BRIEF DESCRIPTION OF CHAPTER CONTENT

Chapter 1 gives a brief description of the chapters from 2 through 7 of this work.

Chapter 2 (Introduction and literature review) addresses the importance of early diagnosis, history of Raman Effect, and the principle of Surface Enhancement Raman Scattering (SERS). This chapter can be listed under three major topics. First, fundamental concepts of detection technologies, the purpose is to diagnose diseases. In terms of recent detection technologies, this subchapter contains the differences between the Raman Effect technology and the conventional technology. Second, it describes the background and principle of Raman Effect. Third, the methods to enhance the weak Raman scattering to the surface enhanced Raman scattering (SERS) is interpreted on this subchapter. In terms of SERS, the materials, structures, measurement methods, and measurement system are mentioned.

Chapter 3 (motivation and research goal) presents the objectives and the motivations of this dissertation. The research goals can be divided into five main topics. (1) Reducing the fabrication cost for bulk production. (2) Demonstrating the reproducible of this fabrication. (3) Maximizing the SERS signal to identify a specific Raman line. (4) Coupling the SERS substrate to a probe head and an articulated arm system. (5) Minimizing the diameter of the probe head for less invasive clinical measurement. (6) Obtaining the preliminary Raman Spectrum measurements from chemical and biological specimens.

Chapter 4 (fabrication methods, AFM and SEM imaging of the SERS substrates) outlines the fabrication processes of sputtered Au on aluminum substrates for *in vitro* and *in vivo* applications. In terms of the fabrication processes, it can be listed under six subchapters. (A) The

similarity between three kinds of aluminum samples after KOH wet etching. (B) The surface morphologies of three different kinds of aluminum foils: Non-etched, etched, and stirred-etched. (C) The principle of Au sputtering system. (D) The deposition of sputtered Au on three different kinds of aluminum foils. (E) The sputtered Au thicknesses with respect to the positions on the wafer. (F) The fabrication processes of *in vitro* and *in vivo* systems.

Chapter 5 (Raman spectrum measurement from a chemical specimen) introduces the measurement results of the SERS signals from Rhodamine 6G (R6G) in contact with different Au substrates and aluminum substrates. In terms of obtaining SERS signals, best optimized parameter was demonstrated in this work. It can be divided into seven topics. (a) A setup of a measurement system. (b) A serious of measurement from 1 nano molar to 1 milli molar R6G. (c) The Raman signals from different aluminum samples. (d) The Raman signals from sputtered Au on different etching time of aluminum foils. (e) The Raman signals with respect to deposition angels and positions. (f) The Raman signals from *in vitro* and *in vivo* systems. (g) The SERS signal from R6G, chicken cartilages and chicken bones.

Chapter 6 (Summary and future work) introduces a comprehensive summary of this work. It contains the defeat of this work from different aspects. It also offers recommendation for future improvement. For the future work, the fabrication and design of a SERS probe head and an articulated arm system for chemical and biological measurements of the future work contains an evolution of the probe head which follows four steps: ① Coupling SERS substrates to a probe. ② Coupling the remote SERS probe head to an articulated arm system. ③ Reducing the diameter of probe size from 2 mm -> 1 mm -> 0.5 mm (needle probe). ④ Develop other cost efficient SERS substrates with this fabrication steps.

CHAPTER 2: INTRODUCTION

2.1 Importance of Early Diagnosis

Hundreds of people die from cancers and diseases around the world every minute [1]. From 2015 statistic data, 1.6 million people had been diagnosed with cancers, and one- third of them had passed away in the United States [2]. Until today, the numbers of people suffering from diseases and cancers keeps raising, because the people are addicted to processed foods, suffered from polluted environments, and lack of regular life habits. Those factors increase the risk of cell mutation, and it turns into the cancers and diseases [3]. Therefore, in order to increase the survival rate, early diagnosis has been accounted for a very important technology for the human kind. The early diagnosis technology has been investigated and developed since late twentieth century. Cancers and diseases can be treated successfully once they are diagnosed in early stage, which prevents it from spreading [4]. Molecular level detections for early diagnosis is required while identifying specific mutated genes, proteins, or cells. In terms of molecular level detections, it is based on two main categories. (a) Molecular diagnostics. (b) Molecular imaging.

(a) The principle of molecular diagnostics is based on biometrics which contain the technologies of tracking and analyzing a specific biomarker from proteome. Proteome includes a given type of genome, cell, tissue, or organism [5]. Typically, a biopsied human specimen is required such as blood, tissue, saliva, skin and etc for molecular diagnostics [6]. For example: Proteomic image from mass spectrometry and microarray image from gene chip are two kinds of methods to obtain the patterning of proteins and genes [7, 8]. The applications cover a cancer, a disease risk management, an infectious

disease, a treatment, a prenatal, and etc. Although advanced molecular diagnostics technology possesses advantages of sensitivity, low cost, convenience due to accuracy and consistent measurements, a biopsied human specimen required an operation.

(b) The foundation of molecular imaging is built on the intersection of in *vivo* imaging and molecular biology. This technology can be employed to visualize functions and molecular structures of the living organisms without any surgeries. The principle of the molecular imaging is based on interactions between targeted cells and imaging agents. The cancers or diseases can be localized by applying different forms of energy. In terms of image agents, it covers different radiopharmaceuticals (^{99m}Tc, ^{1}H, ^{111}ln, ^{64}Cu, 11C, ^{16}F, ^{18}F, and etc.), Fluorochromes, Photoproteins, and Luciferins [9, 10]. In terms of energy, it contains radiations / magnetisms / radiofrequencies (RF)/ sound waves / photon emissions and etc. For example: Magnetic resonance imaging (MRI) [11], Computed tomography (CT) [12], Ultrasound [13], Positron emission tomography (PET) [14], single photon emission computed tomography (SPECT) [15], Fluorescence [16], Bioluminescence [17], and Intravital microscopy[18]. The comparisons of each technique is shown on table 1.1[10] (COPYRIGHT).

Table 1.1 The comparison of molecular imaging system. [10] (COPYRIGHT)

Table 1 | Overview of imaging systems

Technique	Resolution*	Depth	Time†	Quantitative‡	Multi-channel	Imaging agents	Target	Cost*§	Main small-animal use	Clinical use
MRI	10–100 μm	No limit	Minutes to hours	Yes	No	Paramagnetic chelates, magnetic particles	Anatomical, physiological, molecular	$$$	Versatile imaging modality with high soft-tissue contrast	Yes
CT	50 μm	No limit	Minutes	Yes	No	Iodinated molecules	Anatomical, physiological	$$	Imaging lungs and bone	Yes
Ultrasound	50 μm	cm	Seconds to minutes	Yes	No	Microbubbles	Anatomical, physiological	$$	Vascular and interventional imaging‖	Yes
PET	1–2 mm	No limit	Minutes to hours	Yes	No	^{18}F-, ^{64}Cu- or ^{11}C-labelled compounds	Physiological, molecular	$$$	Versatile imaging modality with many tracers	Yes
SPECT	1–2 mm	No limit	Minutes to hours	Yes	No	^{99m}Tc- or ^{111}In-labelled compounds	Physiological, molecular	$$	Imaging labelled antibodies, proteins and peptides	Yes
Fluorescence reflectance imaging	2–3 mm	<1 cm	Seconds to minutes	No	Yes	Photoproteins, fluorochromes	Physiological, molecular	$	Rapid screening of molecular events in surface-based disease	Yes
FMT	1 mm	<10 cm	Minutes to hours	Yes	Yes	Near-infrared fluorochromes	Physiological, molecular	$$	Quantitative imaging of fluorochrome reporters	In development
Bioluminescence imaging	Several mm	cm	Minutes	No	Yes	Luciferins	Molecular	$$	Gene expression, cell and bacterium tracking	No
Intravital microscopy¶	1 μm	<400–800 μm	Seconds to hours	No	Yes	Photoproteins, fluorochromes	Anatomical, physiological, molecular	$$$	All of the above at higher resolutions but limited depths and coverage	In development#

*For high-resolution, small-animal imaging systems. (Clinical imaging systems differ.) †Time for image acquisition. ‡Quantitative here means inherently quantitative. All approaches allow relative quantification. §Cost is based on purchase price of imaging systems in the United States: $, <US$100,000; $$, US$100,000–300,000; $$$, >US$300,000. ‖Interventional means used for interventional procedures such as biopsies or injection of cells under ultrasound guidance. ¶Laser-scanning confocal or multiphoton microscopy. #For microendoscopy and skin imaging. (Table adapted, with permission, from ref. 85.)

Molecular imaging systems overcome the disadvantage of molecular diagnostics systems but are not attractive by high cost effectiveness, and inconvenience diagnosis. Besides that, CT and MRI are unable to detect clear molecular level image due to their limited resolutions and low sensitivity [19, 20]. However, there is still one more molecular imaging system called surface enhancement Raman scattering (SERS) which overcomes the downsides of molecular imaging and molecular diagnostics systems.

SERS is based on the development of regular Raman scattering and Raman spectrum which will be discussed on the next subchapter. Raman spectroscopy is a powerful tool, because it is cost-effective, time-efficient, stable, and safe. In addition, it does not need any sophisticated image processing techniques as the CT and MRI. However, Raman spectroscopy has a low signal-to-noise ratio (SNR) and requires biopsies for tissues or body fluids examinations. It has been found that the Raman signal strength can be amplified by a factor of 10^6-10^9 when the specimen is placed in contact with a nano-rough metallic surface. This will become a significant technique for early disease-diagnosis, so that it can be widely applied in clinics, hospitals, and government institutes in order to identify the diseases and so reduce the huge numbers of the people suffering from cancers and diseases.

2.2. Raman Scattering

The Raman Effect has been well known for almost a hundred years. The first Raman spectrometer (figure 2.1) was built in 1928 by C.V Raman who was awarded The Nobel Prize in Physics in 1930 [21]. The Raman Effect happens when a molecular vibration interacts with a

photon from a light source. Light scattering can be divided into two parts: Rayleigh (elastic) scattering and Raman (inelastic) scattering.

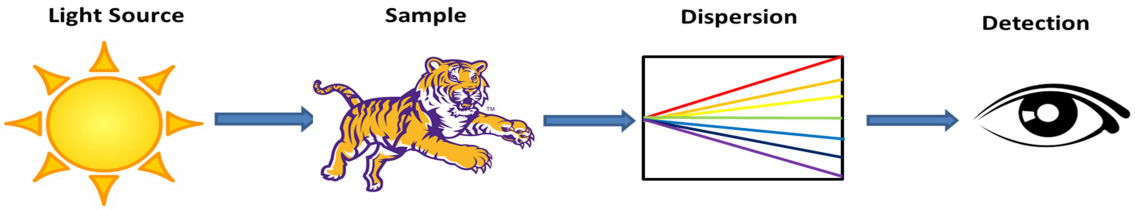

Figure 2.1 The first Raman spectrometer was built by C.V. Raman in 1930 [21].

In Rayleigh (elastic) scattering, the majority of the scattered photons have the same energy and wavelength as the incident photons. In other words, the oscillating vibration of a molecule does not couple with any oscillating vibration from the incident photons; therefore, the molecule remains at its original oscillating vibrational state after the photon emission. Then, emitted photons have the same energy as the incident photons, which can be interpreted as no energy transfers between a photon and a molecular vibration.

In Raman (inelastic) scattering, a minority of the scattered photons have a different energy and wavelength from the incident photons. In this case, the oscillating vibration of a molecule does couple to any oscillations from incident photons; therefore, the molecule changes vibrational state, and the emitted photon has a different energy from the incident photon. It can be explain as energy transfers between a photon and a molecular vibration.

Raman (inelastic) scattering can be separated into two categories: Stokes and anti-Stokes scattering, respectively. For the Stokes scattering($\Delta E = E_i - E_s > 0$), the molecular vibration absorbs the energy from the incident photon and then emit the photon (E_s) which has a lower energy than the incident photon (E_i). In contrast, for the anti-Stokes scattering($\Delta E = E_i - E_s <$

0), the emitted photon has higher energy. Therefore, Stokes scattering produces lower energy photons than the incident light while anti-Stokes scattering produces higher energy photons. However, the probability of Stokes transition is much higher than Anti-stokes, so Stokes scattering is mainly target in the research[22]. The different types of Raman Effect are shown in figure 2.2.

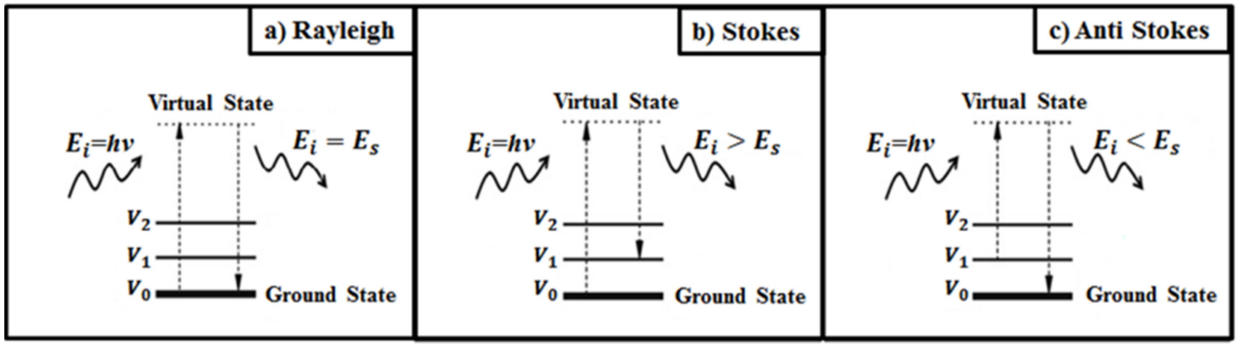

Figure 2.2 Raman Effect (a) Rayleigh scattering, (b) (c) Raman scattering by Stokes and Anti-Stokes [22].

Typically at room temperature, most of the molecules are in the ground state, but a few of them will be in excited states due to the energy absorption from the photon. The Planck's equation (1): the change of the energy is related to the change of the photon frequency. Then, the change of the photon frequency results on the change of photon wavelength according to the wave equation (2). Therefore, the change of photon energy at a given wavelength indicates that there is a corresponding change of molecular vibration in the excited or ground state.

$E = h\nu$ (E= Energy of a photon Joules, $h = 6.626 \times 10^{-34}$ J*s Planck's constant) (1)

$C = \lambda \nu$ (C = 3 x 10^8 m/s, λ=wavelength, ν=frequency Hz=1/second) (2)

In other word, a molecular vibration mode is generated when the molecule absorbs a quantum of energy. The vibration mode is depended on the changes of covalent bond caused by molecular dipole moment between each atom inside the molecule. When a molecular vibration interacts with an external oscillating electric field E, the induced dipole moment is generated:

$$P = \alpha E$$

(where α is the polarizability of the molecule).

$$\alpha = \alpha_0 + \Delta\alpha cos2\pi\upsilon_k t$$

(where α is the polarizability of the molecule with respect to time, the α_0 is initial polarizability, $\Delta\alpha$ is the change rate of polarizability, υ_k is the molecule oscillating frequency).

$$E = E_0 cos2\pi\upsilon_0 t$$

(where E is an external oscillating electric field from the photon with respect to the time, E_0 is the amplitude of the electric field, υ_0 is the frequency of the incident photon).

$$P = \alpha E = (\alpha_0 + \Delta\alpha cos2\pi\upsilon_k t)(\, E_0 cos2\pi\upsilon_0 t)$$

Solving by trigonometric identity: $\cos A \times \cos B = \frac{cos(A-B)+\cos(A+B)}{2}$

$$P = \alpha_0 E_0 \cos 2\pi\upsilon_0 t + \frac{1}{2}\Delta\alpha E_0 \cos 2\pi\,(\upsilon_0 + \upsilon_k)t + \frac{1}{2}\Delta\alpha E_0 \cos 2\pi\,(\upsilon_0 - \upsilon_k)t$$

Therefore, the final equation shows the order of Rayleigh, Anti-Stokes, and Stokes scattering, and those are generated simultaneously when the incident light interacts with the

molecular vibration. The shape of the Raman signal is independent of the frequency or wavelength of the incident light, but the intensity will be changed by frequency or wavelength of the incident light [23].Therefore, a property of the material/ molecule can be identified by detecting the change of photon energy or wavelength, because every molecule has their own unique Raman Spectrum. The frequency range of molecular vibration is from a few Hz to 10^{14} Hz. [24].

The definition of Raman shift is the energy lost by the photon $\Delta E = E_i - E_s$; therefore, it is positive for Stokes and negative for anti-Stokes. The Raman spectrum is formed by Raman shifts (horizontal axis) dependence of the Raman scattered intensity at a given incident wavelength (vertical axis) (figure 2.6). The unit of Raman shift is a wavenumbers ($\tilde{\nu} = {}^{1}/_{\lambda} = {}^{\nu_s}/_{C} = \frac{E}{hC}$, where ν_s is a frequemcy in hertz, $\mathrm{C} = 3 \times 10^{8} \frac{\mathrm{m}}{\mathrm{s}}$, $\mathrm{E} =$ Energy of a photon Joules, $h = 6.626 \times 10^{-34}\ \mathrm{J} * \mathrm{s}$ Planck's constant), which has units of inverse wavelength as this value is directly related to energy. In fact, it is convenient to use the wavenumber scale instead of energy scale or wavelength scale to express the molecular vibration mode. Typically, Raman scattered light is collected by a microscope objective and passed through Rayleigh rejection filter and diffracted by a grating and then analyzed by a computer. Normally a bandpass filter is used to reduce the noise. A schematic of a Raman spectrometer (figure 2.3) contains light source (laser instrumentation), detectors (collect Raman scattering), and optical filter technology (Rayleigh rejection filter, grating dispersion and Beam splitter), and computer (analyze signal). The Raman spectrometer (figure 2.4) (LabBRAM LAB300 visible/ near-infrared (400 to 2100 nm), LABRAM Confocal Raman Microscope in EMDL, LSU) was employed in this research. This Device equipped with three different objectives: 10x NA (numerical aperture) = 0.3 and WD (Working distance) =10.1 mm, 50x NA=0.5 and WD=0.66 mm, 100x NA=0.9 and

WD=0.21 mm. However, another 50x NA=0.55 and WD=10 mm objective was chosen in this research due to a better NA and WD, which represents a big angle of the light collection and more working space between the objective and specimen. The resolution is taken as (d=λ/2NA).

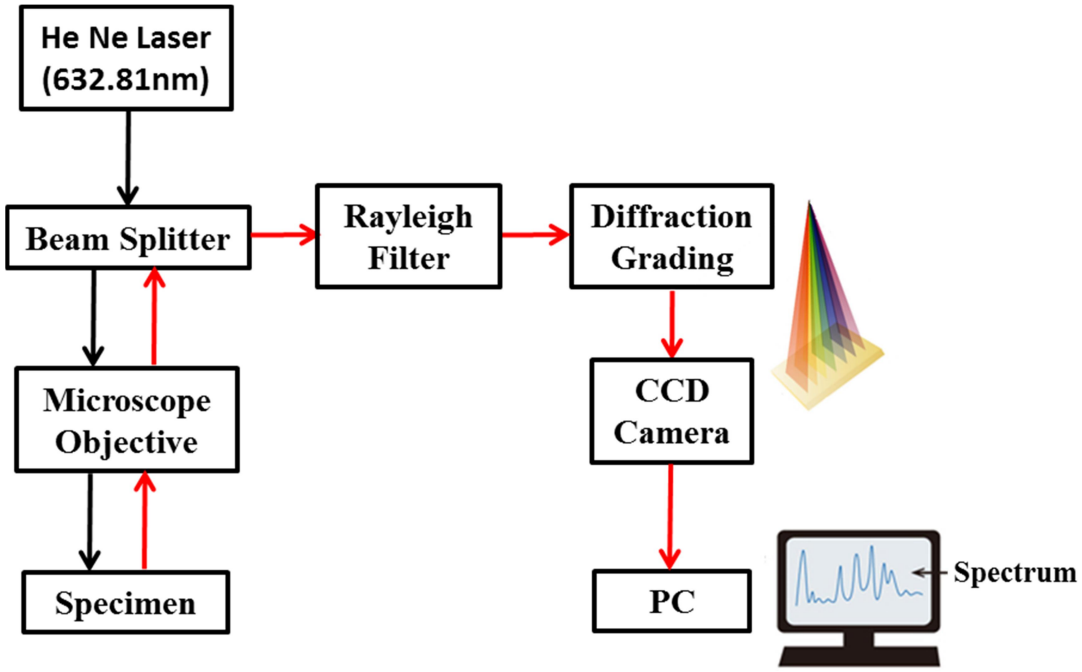

Figure 2.3. The schematic of the Raman Spectroscopy System.

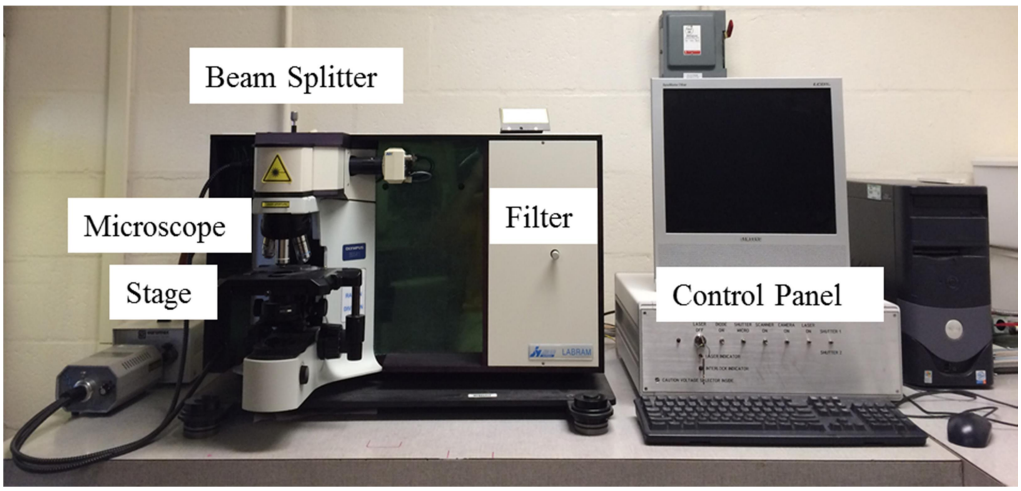

Figure 2.4 The LaBRAM Integrated Raman spectrometer system (EMDL, LSU).

2.3. Surface-Enhanced Raman Scattering (SERS)

Raman spectroscopy has been widely employed in different fields. For example, in life Sciences: bone structure, DNA, drug, and cell interactions analysis. In semiconductors and carbon materials: purity, defect, doping effects, and stress/strain analysis. In geology: mineral and phase distribution, and fluid inclusions. In pharmaceuticals and cosmetics: powder content, purity, and compound distribution in tablets [25, 26]. Recent applications in biosciences were published: painless laser device spot early signs of disease for cancer, muscle and skin [27, 28]. Raman spectroscopy can be employed in three different phases [29, 30]. Raman spectrometer becomes a popular tool due to a short time sample preparation, short time measurement, non-destructive method and small quantity samples. Therefore, Surface-Enhanced Raman Scattering (SERS) has been deeply investigated in order to increase the sensitivity and intensity of Raman signal.

Surface-Enhanced Raman Scattering (SERS) was discovered by Martin Fleischmann and his colleagues in 1973 by manipulating electrochemically roughened silver [31]. The Raman signal is amplified by several orders of magnitude (10^5-10^8) when a specimen is in contact with a rough metallic surface. The typical SERS arrangement is shown in figure 2.5. The illustration of SERS and non-SERS Rhodamine 6G Raman spectra is shown in figure 2.6 (logarithmic scale).

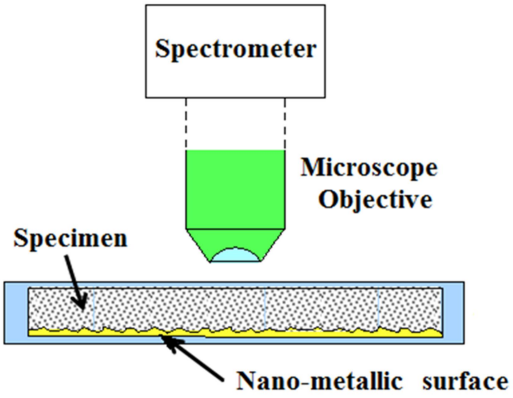

Figure 2.5 The typical of Surface-Enhanced Raman Scattering (SERS) arrangement.

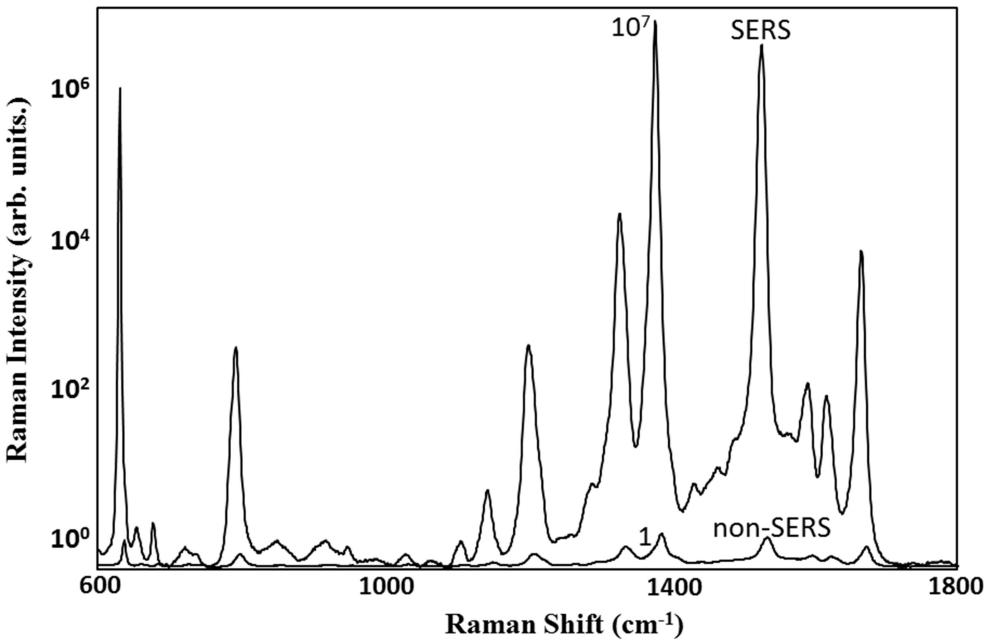

Figure 2.6 The illustration of SERS versus non-SERS Rhodamine 6G Raman spectra (logarithmic scale).

The exact principle of the SERS effect is still under debate. There are two main theories: First, electromagnetic theory is believed to explain the majority contribution for the SERS effect. Second, chemical theory is the minor contributor to the SERS effect.

Electromagnetic theory uses a surface plasmon resonance (SPR), which is generated when an incident light strikes on the metallic surface. The coherent oscillation electrons on metallic surface are excited by the electromagnetic radiation (EM). The scattering occurs on the metallic surface only when the direction of plasmon oscillations is perpendicular to the metallic surface. The SPR can be divided into two categories: The surface plasmon polaritions (SPPs) and localized surface plasmon resonances (LSPR). SPPs: If surface plasmon propagates only in both x- and y-directions along with the thin metallic surface about 10 to 100 μm, but evanescently decays in the z-direction with 1/e decay length of about 200 nm [32, 33]. LSPR: If a metallic nanoparticle is smaller than the wavelength of the incident light, the surface plasmon is trapped around the metallic nanoparticle, creating "hot spot" (figure 2.7). The LSPR is believed to be the main contribution of SERS effect [34, 35]. The electromagnetic theory applies for the majority of SERS phenomena, but still some phenomena have to be explained by chemical theory.

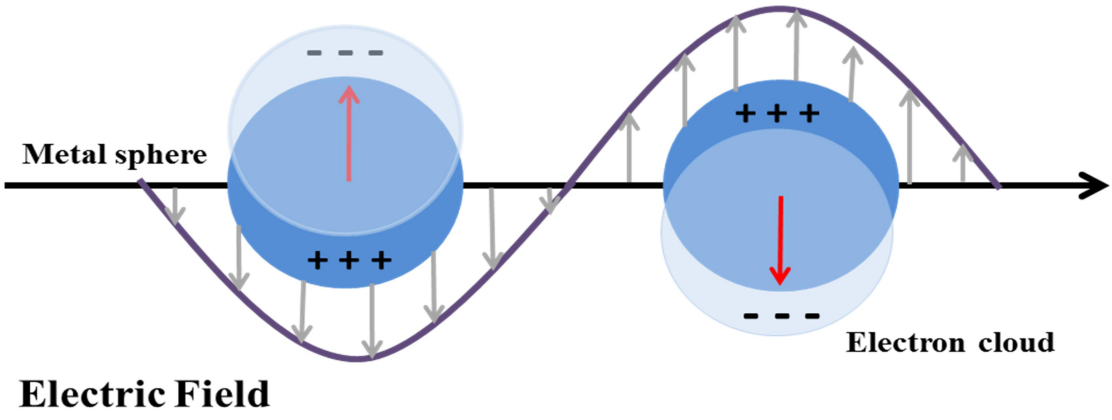

Figure 2.7 The schematic diagram of localized surface plasmon resonance (LSPR).

Chemical theory can be interpreted by the charge-transfer complex, which is the modification of the Raman polarizability on adsorption of the molecule on the metallic surface. A covalently bond complex is generated when a molecule is adsorbed to the metallic surface, and it changes the Raman polarizability of the molecule. Therefore, when the molecule and metallic surface are exposed to an incident light, two different cases occur [22]: 1. A covalently bond complex does not generate when the molecule is not adsorbed by metal. Then, electrons in the metal act as perturbation or direct excitation. 2. A covalently bond complex does generate when the molecule is adsorbed by metal. Then, the electrons have another channel to arrive the excited state (conduction band) which is called indirect ex excitation. This channel is from the highest occupied molecular orbital (HOMO) to conduction band of metal, and then to the lowest unoccupied molecular orbital (LUMO). 3. An emitted Raman shift photon is generated when an electron return to ground state for both case.

The SERS effect only occurs on high conductivity nano-metallic surfaces. Aluminum (Al), Gold (Au), Copper (Cu), and Silver (Ag) are widely employed on SERS metallic substrates [36-39]. Those are three main reasons. 1. Those material can be fabricated into nano-metallic substrates. 2. The high conductivity σ (S/m) (3.5 to 6.5 × 10^7) is required because of electrons produce Raman (inelastic) scattering. 3. A wider range of incident wavelength arises from localized surface plasmon resonance (LSPR) from ultraviolet to near infrared range (300 nm-1250 nm) shown in table 2.1.

Au metal is commonly used at majority of publication due to several main reasons [39, 40]: First, it has a good signal strength in SERS application. Second, it has a wide wavelength range (580-1250 nm). Third, the inert Au metal rarely interacts with other materials especially oxygen. Fourth, it has high reflectance and almost transparent in thin film for optical applications.

Fifth, it has high etching selectivity of Aluminum over Au in KOH. Sixth, it is non-toxic as silver (Ag). Therefore, Au is chosen as a metallic surface in this research.

Table 2.1 Different wavelength ranges of localized surface plasmon resonance (LSPR) from different metals.

Metal	**Wavelength Range (nm)**
Aluminum (Al)	300 - 600
Gold (Au)	580 – 1250
Copper (Cu)	550 – 1250
Silver (Ag)	400 - 1000

Different shapes and sizes of nono metallic substrate are related to different plasmon resonance spectra. For example, different shapes of SERS metallic substrates are fabricated such as nanoparticle/nanoislands/ nanocarters/ nanoclusters. Different intensities and colors of plasmon resonances are generated by a strong interaction between electromagnetic field enhancement and adsorbed molecule internal level [41-43]. The fabrication methods that have been used are electrospinning [44], self-assembled polyelectrolyte [45], nanoimprint lithography (NIL) [46], fission fragment [47], electrochemical deposition [48],electron beam induced deposition[49], and focus ion beam (FIB) [50].

Generally, the methods of Raman measurements can be divided into three categories (figure 2.8): backscattering, spatially offset Raman spectroscopy (SORS) and transmission [51].

First, the backscattering measurement performs the purest Raman signal of the material but with a subsampling problem (only measure one layer). Second, the SORS produces pure spectra for each layer, and it can do region scanning for a multilayer substrate but it comes with two disadvantages: 1. Layers have to be nearly transparent. 2. It produces low signal due to the Δd (inverse-square law, the signal intensity is inverse proportional to the distance square). Third, The transmission measurement overcomes the subsampling problem (able to measure multilayers) but it comes with two disadvantages.1. This method is scarifying the purity and intensity of the Raman signal due to passing the substrate. 2. The detector has to be setup on other side of the input source.

Typically, the SERS structure can be applied on the backscattering and transmission measurement methods (figure (a) and (c)). However, the backscattering measurement method allows the incident laser beam and Raman scattering light pass through the same optical path with higher signal intensity, compared to backscattering measurement method. Therefore, the backscattering method is employed for *in vivo* and *in vitro* applications in this research.

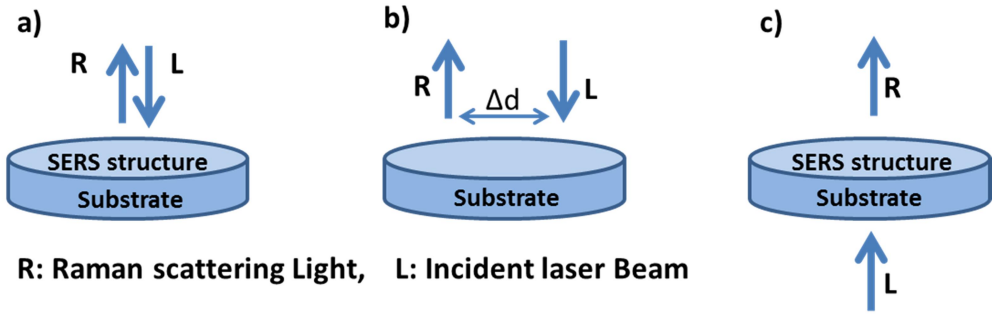

Figure 2.8 Three different types of Raman measurement methods (a) Backscattering, (b) Spatially Offset Raman Spectroscopy (SORS), and (c) Transmission.

CHAPTER 3: RESEARCH MOTIVATION AND GOAL

3.1. Research Motivation

Raman spectra have been employed to identify specimens for many years, because it overcomes the downsides of molecular imaging (CT, MRI) and molecular diagnostics (gene chip, proteomic image) systems which were mentioned in subchapter 2.1. For example: Molecular diagnostic requires biopsy for specimen measurements. CT and MRI have limitation in visualizing the molecular image due to low sensitivity. Raman scattering technology provides more accurate measurement on cellular or molecular specimen for either chemical or biological measurements. Raman spectroscopy has been widely used in many applications such as biosciences, vibrational chemistry, and pharmaceutical studies. Over the past decades, Raman spectrometers have been improved by limiting the background noise of detectors, and reducing transmission loss in optical systems [51]. Increasing the laser power is a limited option since it might damage the specimen. However, these improvements do not tremendously increase the initial Raman signal; therefore, SERS substrates have become an important method to increase the initial Raman signal. The generally weak Raman signal is enormously enhanced 10^6 to 10^9 larger when the specimen is in contact with a rough metallic surface. Therefore, how to fabricate a rough metallic surface becomes a challenge of SERS technology. In twenty century, the nano-patterning and nano-devices have been widely used in large range of applications. The implication is that expensive equipment has to be employed in order to produce the nano-scale technology, especially for the SRES substrates. This research aims to develop a cost efficient and reproducible SERS substrate by taking advantage of aluminum substrates, which has some existed patterns.

3.2. Research Goal

This research aims not only to increase the sensitivity of SERS effect *in vitro* and *in vivo* applications but also to decrease the fabrication cost of SERS substrates. Nowadays, costly lithographic steps have been widely employed to roughen the metallic surface, high density of metallic nanoislands, in order to boost the sensitivity and intensity of SERS. This research will be addressed by the following aspects:

I. A 0.005 cent value of 1 cm^2 aluminum foil as a cheap base and sacrificial substrate.
II. The characteristics of aluminum and processed aluminum substrates.
III. The characteristics of sputtered Au thin films on aluminum and silicon wafer substrates.
IV. An evolution of the SERS substrate coupled with a probe / a needle.
V. A probe head coupled with the articulated arm and spectrometer for chemical and biological measurements.

The final goal of this research is to develop, construct and demonstrate a novel, low cost, high sensitive, reusable, reproducible SERS substrates for *in vitro* and *in vivo* applications for clinical purposes. In terms of *in vivo* probes, a small diameter of the remotely positioned probes will be designed to be minimally invasive with specimens. Moreover, the optical path of the probe which contains a SERS substrate, GRIN, and epoxy will be constructed and optimized in order to reduce the transmission loss and maximize the Raman signal. Ideally, the SERS system may be performed on a patient simply sitting or lying near the spectrometer.

The following issues will also be discussed: rough metallic nanostructure fabrication, Au sputtered machine, wet etching, thickness of Au thin film, comparison of the SERS effect in reflectance and transmission systems, the substrate assembling, probe head design, and the optical path of articulated arm system.

CHAPTER 4: EXPERIMENT SETUP

4.1. Different Aluminum Substrates Preparation

4.1.1 Aluminum Substrates

Aluminum metal has been widely employed in microelectromechanical systems (MEMS) because of low cost, low density 2.7 g/cm^3 and low resistance 2.8×10^{-8} ρ (Ω · m) [52]. For example, aluminum is often used as conductors in integrated circuit due to the high conductivity in CMOS process. Aluminum sacrificial layer is removed by selected etching processes in order to released or lift the top layers or microstructures [53, 54]. In this research, Aluminum was chosen in this research because of the properties above: low cost, availability, and easiness to etch and high conductivity. In figure 4.1, different aluminum substrates shown were used in this research including aluminum foils (Price First Aluminum Foil: 25 square feet* NEW_LINE*Kosher, Walmart), aluminum pellets (aluminum shot, approx. 4-8 mm 99.999% stock # 10573 Lot # H18Q18, Puratronic, Alfa Aesar), and shop grade aluminums.

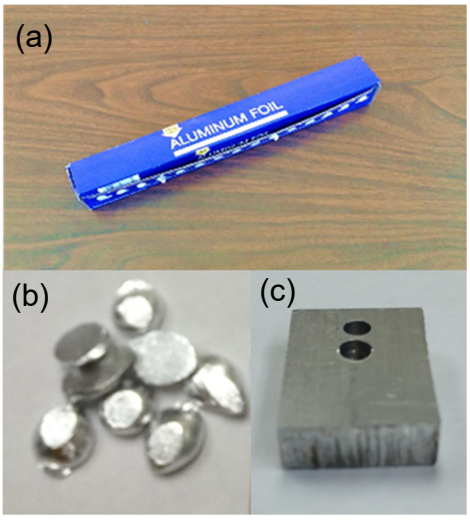

Figure 4.1 Different aluminum substrates (a) House Aluminum Foil, (b) Aluminum pellets (shot) 99.999%, (c) Shop grade aluminums.

All aluminum substrates were cleaned by a standard procedure in order to remove the any attached oil or contamination. The standard cleaning procedure was as follows: 1.Rinse the substrate in acetone. 2. Rinse in isopropyl alcohol (IPA). 3. Rinse in deionized water (DI water). 4. Dry the substrate with nitrogen gun.

In this work, atomic force microscope (AFM) and scanning electron microscope (SEM) were employed to obtain the surface topographies. Those data were converted into images and roughness [55]. In figure 4.2, the roughness (R_a) is the arithmetic average of the absolute values of the peak and valley heights from the mean line, which is described as: $R_a = \frac{1}{L}\int_0^L |Z\ (x)|dx$, where Z (x) is the profile height function, and L is evaluation length. However, R_a makes no distinguish between the peaks and valleys; therefore, the mean square (RMS) R_q is widely used, because it is more sensitive to the peaks and valleys by mean squared absolute values of surface roughness profile. R_q is described as: $R_q = \sqrt{\frac{1}{L}\int_0^L |Z\ (x)|^2 dx}$ [55, 56]. Therefore, the quantitative number of roughness is measured by AFM and represented by root mean square (RMS) in this work.

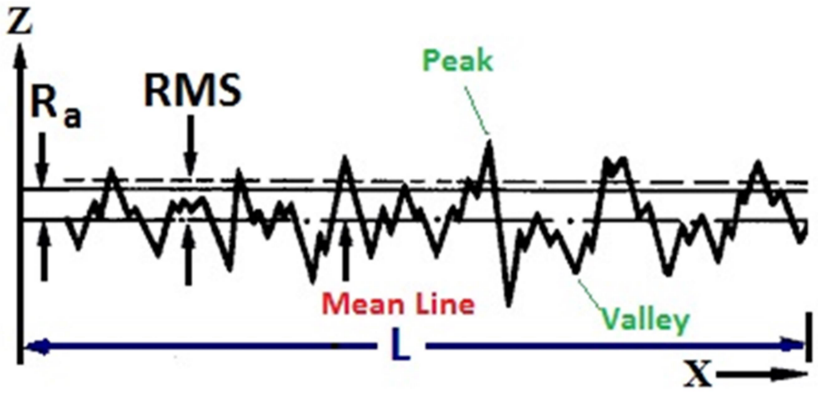

Figure 4.2 A surface profile contains the average roughness R_a and root mean square (RMS) R_q which are based on mean line.

AFM images of the front side (shiny) and back side (dull) of aluminum foils are shown in figure 4.3 and 4.4. In large surface morphologies [100 μm × 100 μm field of view] under 1400 nm scale bar, the RMS height variations and profiles from front and back side of aluminum foils are 140 nm and 200 nm, respectively (figure 4.3 (a) and (b)). In small surface morphologies [1.3 μm × 1.3 μm field of view] under 160 nm scale bar, the RMS height variations and profiles of front and back side foils are 7 nm and 12 nm, respectively (figure 4.4 (a) and (b)). Therefore, the back side of the aluminum foil was rougher than the front side of aluminum foil in both the large and small scales. Table 4.1 shows the comparisons of RMS between front and back side of aluminum foils. Therefore, in this research, the back side of the aluminum foil was employed as a base substrate for SERS substrate because it was rougher. Raman signals from the front and back sides of aluminum foils will be discussed on chapter 5.

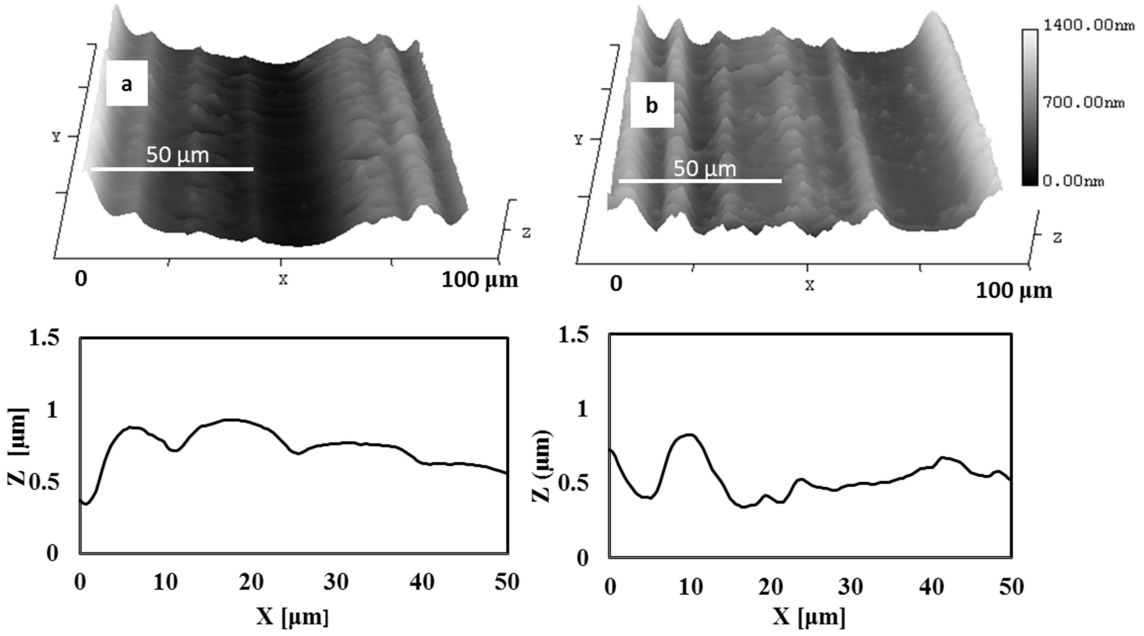

Figure 4.3 AFM images of the aluminum foil [100 μm × 100 μm field of view]. (a) The front side [shiny] and (b) The back side [dull]. The height distributions across 50 μm are shown below. The RMS height variations are 140 nm on front side and 200 nm on back side of the aluminum foil.

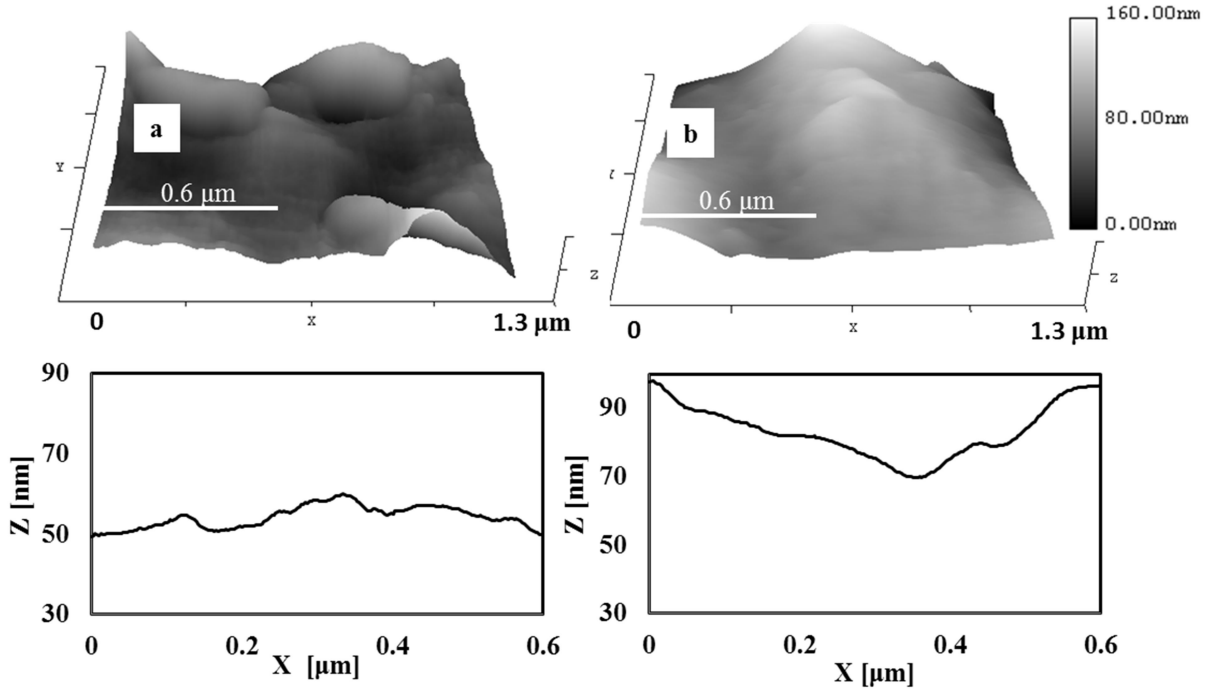

Figure 4.4 AFM images of the aluminum foil [1.3 µm × 1.3 µm field of view] (a) front side [shiny] and (b) back size [dull]. The height distributions across 0.6 µm are shown below. The RMS height variations are 7 nm on front side and 12 nm on back side of the aluminum foil.

Table 4.1 The comparisons of RMS between the front and back side of aluminum foils.

Al \ RMS	Large Scale [100 µm x 100 µm]	Small Scale [1.3 µm x 1.3 µm]
Front side	140 nm	7 nm
Back side	200 nm	12 nm

4.1.2 Wet Etching

In Micro Electro Mechanical Systems (MEMS), the etching processes such as dry etching, wet etching or combination etching have been widely employed to fabricate structures or remove the sacrificial layers in various applications. For instance: In micro or nano scale, a sacrificial layer can be removed by selected etching and then release the top layers or structures. Dry etching such as plasma etcher: Different patterns and etch rates can be manipulated by different gases, temperatures, and power sources [57, 58]. Wet etching such as chemical etching: Different shapes and etching rates can be employed by isotropic or anisotropic wet etching [54, 59]. Moreover, the combination of wet and dry etching for SERS applications were demonstrated in recent publication [60]. In this research, wet etching was chosen.

Potassium hydroxide (KOH) solution was employed to etch a variety of aluminum substrates in this research. The KOH solution was prepared by mixing 70 grams of KOH pellets in 230 mL of deionized (DI) water at 25 ^{o} C [61, 62]. Different aluminum substrates were etched by 30% KOH concentration for 60 seconds. KOH etches aluminum isotopically. The chemical reaction formula are the following [63] :

$$2\,Al\,(s) + 2\,KOH\,(aq) + 6\,H_2O\,(l) \rightarrow 2\,KAl\,(OH)_4\,(aq) + 3\,H_2\,(g) \quad (2)$$

s: Solid l: liquid g: gas aq: aqueous

The KOH etching procedure was as follows: 1.Rinse the substrate in acetone. 2. Rinse in isopropyl alcohol (IPA). 3. Rinse in deionized water (DI water). 4. Dry the substrate with nitrogen gun. 5. 30% KOH etching. (Aluminum substrates are placed inside 30% KOH solution for 1 minute). 6. Repeat from 3 to 4.

The 30 % KOH etch rate of the household aluminum foil at room temperature was 0.5 μm/min. The thickness of house hold aluminum foil changed from 18 um to 17 um after 1 minute of KOH etching. All the etching processes were performed at EMDL.

Figure 4.5 shows the atomic force microscope (AFM) images of etched aluminum foils. In large surface morphologies [100 μm × 100 μm field of view] under 1000 nm scale bar, the root mean square (RMS) height variation and the profile of the etched aluminum foil is 140 nm (figure 4.5 (a)). On the other hand, in small surface morphologies [1.3 μm × 1.3 μm field of view] under 100 scale bar, the RMS height variation and the profile of the etched aluminum foil is 17 nm (figure 4.5 (b)). The significant difference between non-etched and etched aluminum foil is shown in table 4.2. Therefore, according to the roughness of AFM analysis, the roughness increases under small scale; while it decreases under large scale, respectively. The schematic drawing is shown in figure 4.6. Besides roughness of AFM images, SEM images (figure 4.7) were taken in order to support AFM images. SEM images show the same result as AFM image, etched –stirred is rougher than etched aluminum substrate, and etched is rougher than non-etched aluminum substrate. The relationship between Raman signals, different aluminum substrates, and etching times will be discussed on chapter 5.

Table 4.2 The comparisons of RMS between non-etched and etched aluminum foil.

RMS / Al	Large Scale [100 μm x 100 μm]	Small Scale [1.3 μm x 1.3 μm]
Non- Etched	200 nm	12 nm
Etched	140 nm	17 nm

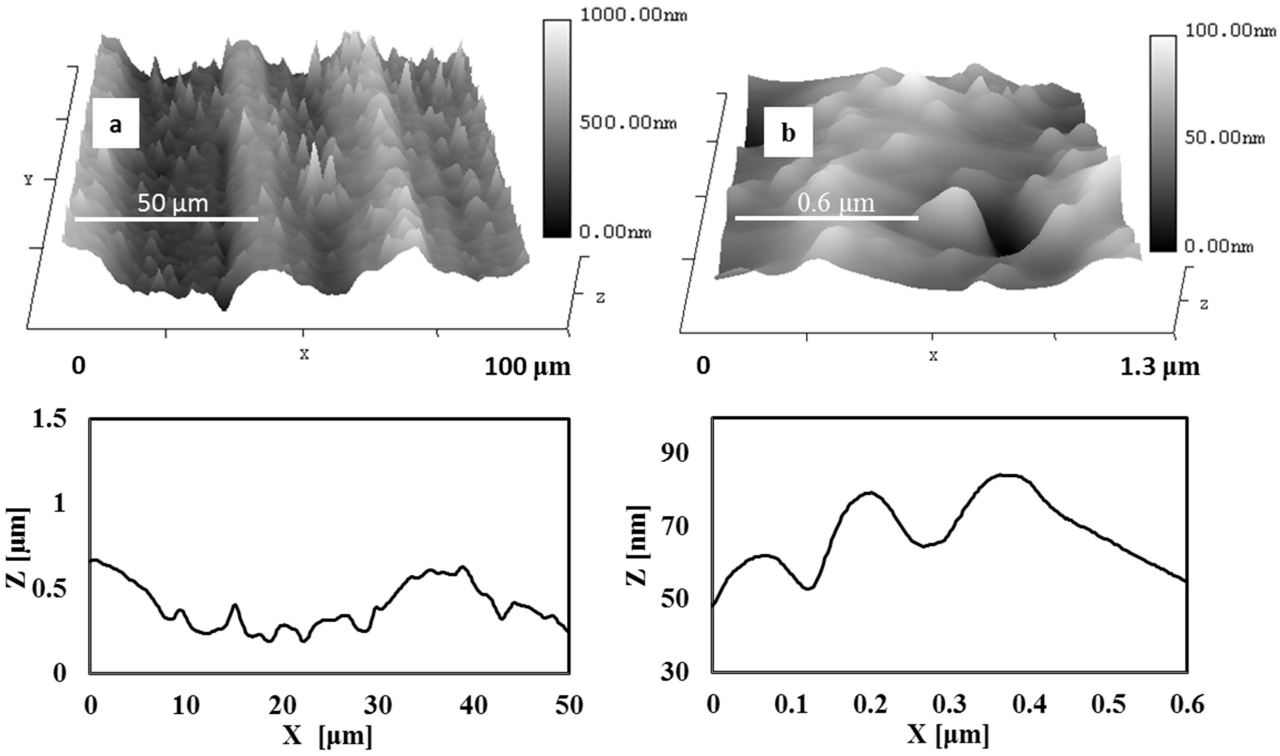

Figure 4.5 The AFM images of the etched aluminum foil (a) large field of view is 100 µm × 100 µm (b) small field of view is 1.3 µm × 1.3 µm. The height distributions across 50 µm and 0.6 µm are shown below. The RMS height variations are 140 nm and 17 nm.

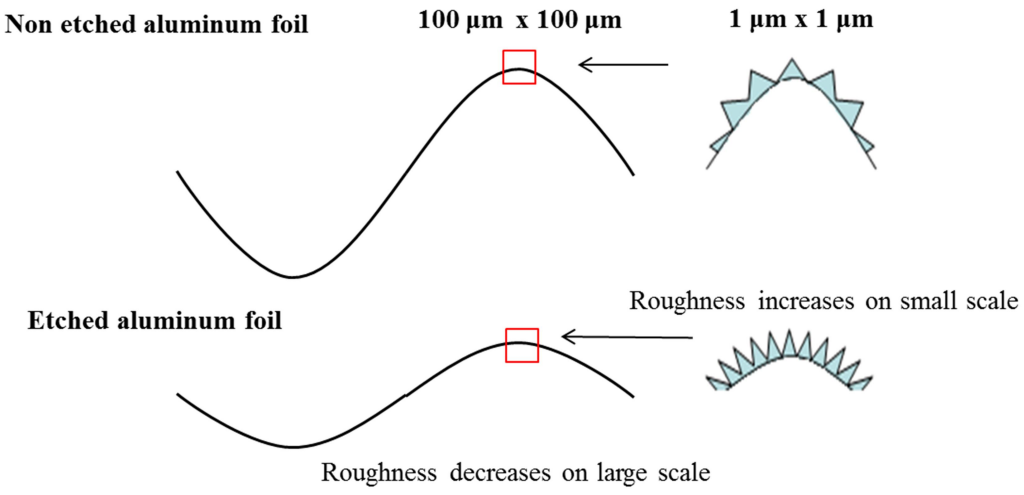

Figure 4.6 The schematic drawing for roughness between non-etched and etched aluminum foil.

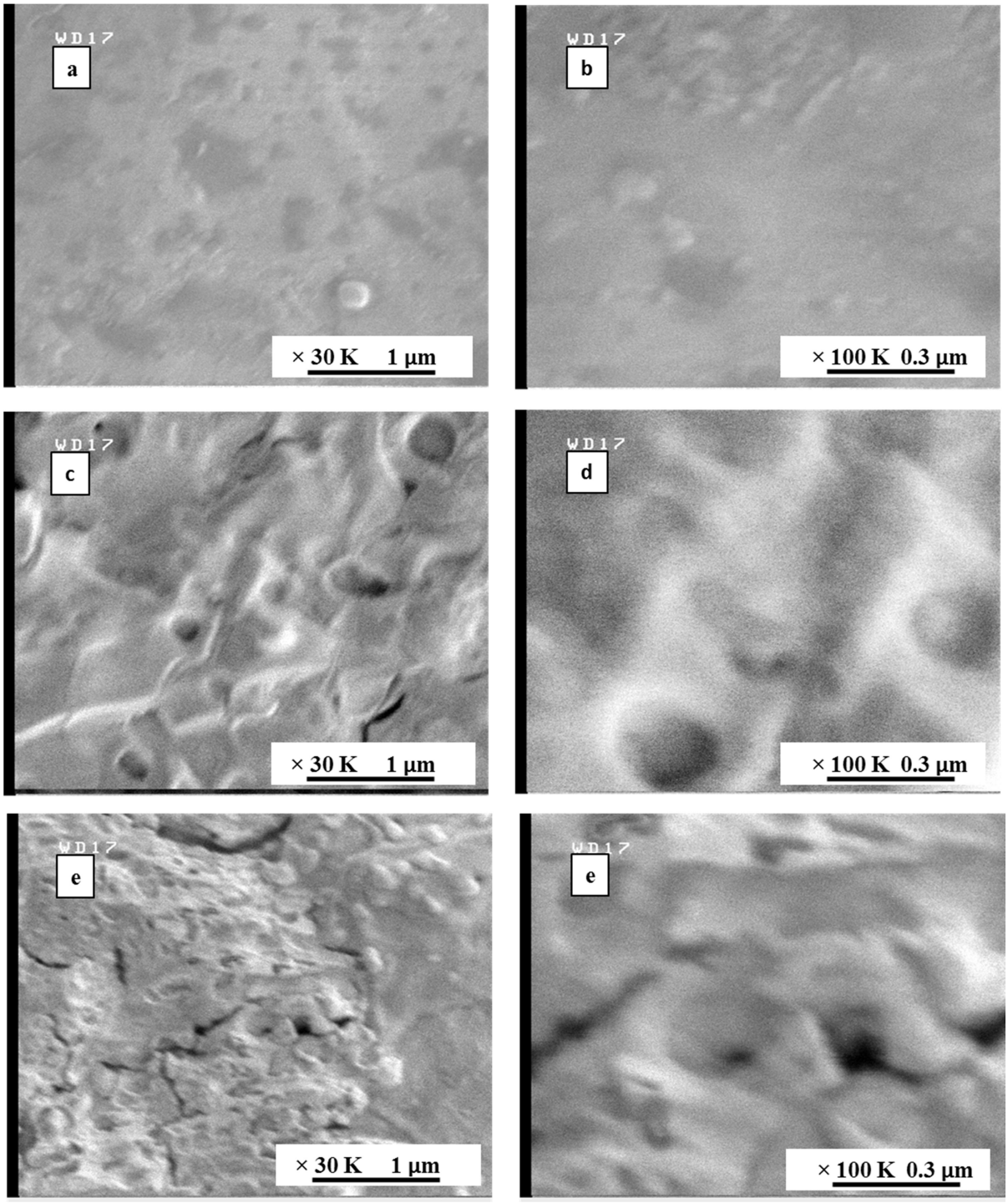

Figure 4.7 SEM images [1µm × 1 µm and 0.3 µm × 0.3 µm field of views] of different types of aluminum foils. (a)(b) non etched, (c)(b) etched, (e)(f) etched-stirred.

4.2. Nanostructure Deposition

A uniform thin film deposition technology has a significantly important place in MEMs technology. There are two main categories for fabricating a thin film shown on table 4.3 and 4.4: chemical and physical depositions. Chemical reactions between the substrate surface and reactant gases is the principle of chemical deposition such as atomic layer deposition (ALD), plasma enhanced chemical vapor deposition (PECVD), low pressure chemical vapor deposition (LPCVD) and electroplating. On the other hand, for physical method, the principle of physical deposition is that dynamic atoms pass through a low pressure gas and condense on the substrate, such as electrohydrodynamic, pulsed laser deposition, sputtering, electron beam evaporator, molecular beam epitaxy (MBE) and thermal evaporator.

In this work, sputtering deposition was chosen for two reasons:

I. The melting point of aluminum is 660.3 C°. Therefore, low deposition temperature protects the aluminum substrate being damage.
II. Small grain size of Au structure provides smaller gaps between each Au structure which produces higher SERS signal.
III. It performs a low impurity film and a low cost fabrication method.

The only disadvantage is possible stress or damage to the substrate surface during the process due to the physical deposition method. However, this is minimal for ductile aluminum. The ductility represents the physical property of any material. Ductility is the ability to be stretched or bent under tensile stress without fractures [64].

Table 4.4 Comparison of thin film chemical deposition technology.

Chemical Deposition	Cost	Substrate T (°C)	Deposition Rate (A°/s)	Film Density	Grain Size	Film Impurity	Material
Atomic layer deposition (ALD)	Extreme High	30~800	0.5~6	Excellent	0.1~0.5	Very Low	Metal Dielectric
LPCVD	Very High	600~1200	10~50	Excellent	1~10nm	Very Low	Dielectric
PECVD	Very High	200~300	10~100	Good	10~100nm	Very Low	Dielectric
Electroplating	Very Low	40~70	100~200	Good	50~100nm	Low	Metal

Table 4.3 Comparison of thin film physical deposition

Physical Deposition	Cost	Substrate T (°C)	Deposition Rate (A°/s)	Film Density	Grain Size	Film Impurity	Material
Electrohydrodynamic	Very Low	30~80	100~200	Good	30~100nm	Mid	Metal Dielectric
Pulsed laser deposition	Mid	25~600	2~10	Good	5~100nm	Poor	Metal Dielectric
Sputtering	Mid	200	Metal: 100 Dielectric: 1~10	Good	10nm	Low	Metal Dielectric
Electron beam evaporator	High	50~100	10~100	Poor	10~100 nm	Low	Metal Dielectric
Molecular beam epitaxy (MBE)	Extreme High	350~700	3~10	Excellent	0.7~7nm	Low	Metal Dielectric
Thermal evaporator	Very Low	50~100	1~20	Poor	10~100 nm	High	Metal

Au metal has been widely employed to fabricate nanostructure in MEMs application. For example: An average size of 10 nm to 50 nm partially embedded gold nano-islands with 4.5 nm initial thick gold film on a microscope glass slide were fabricated by high-end precision electron beam evaporator and followed with 500 °C thermal annealing processes; in addition, An average size 22 nm and roughness of 50 nm of AuNIs on the microscope glass were fabricated by thermal evaporator and thermal annealing (700 °C) processes [65, 66]. The shapes of AuNIs and the distance between each AuNIs could be manipulated by deposition and annealing times [67]. The profile of nano-gaps between the Au nanoislands (AuNIs) (clumps) on the silicon wafer on the SEM and AFM images are shown on figure 4.8 (copy right from RSC Advance). This kind of AuNIs structure are expected in this work, therefore; Au was chosen to be the target material for a sputtered thin layer.

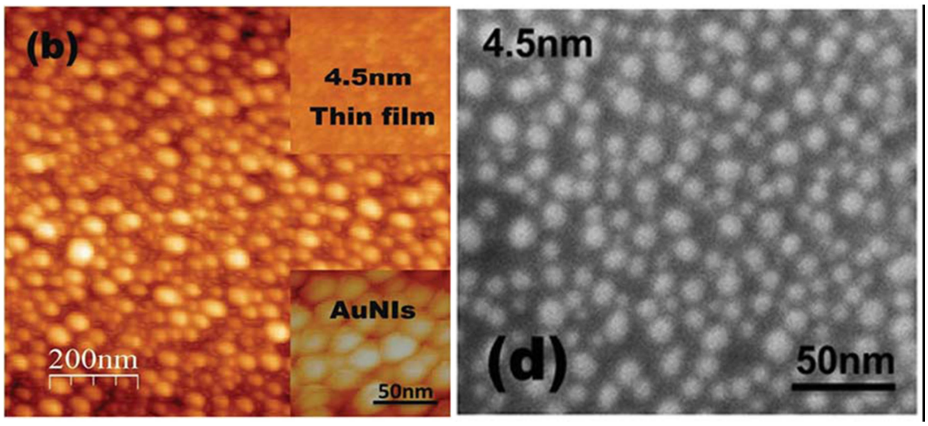

Figure 4.8 The SEM (b) and AFM (d) images of Au nanoislands (AuNIs) on silicon wafer [66] (COPYRIGHT).

4.2.1. Sputtering Chamber

In 1974, John S. Chapin invented the first planar magnetron sputtering source by manipulating a magnetic field to control the velocity and behavior of charged ions and electrons. Charged ions are trapped in a magnetic field close to the target, which produces faster deposition rates. This novel invention upgraded the conventional diode sputtering and overcame some technical problems such as the slow deposition rate, substrate overheat, and small substrate coverage [68]. Most magnetron cathodes are rectangular or circular. Rectangular magnetrons are more commonly used with larger substrates; while circular magnetrons are more commonly used with smaller substrates. Three main power sources inducing the high energy state of magnetrons sputtering are direct current (DC), alternating current (AC) and radio frequency (RF) magnetron sources. In this research, a circular DC magnetron sputtering system was used.

The DC powered magnetron sputtering chamber (Oxford Plasmalab System 400 Sputtering System in CAMD) was employed in this research for Au deposition. Figure 4.9 illustrates the principle of sputtering deposition. A high vacuum $10^{-6}\ torr$ and argon gas are applied inside the chamber. A negative DC voltage is applied to the argon gas creating a neutral plasma that contains free electrons and ionized argons. The free electrons are accelerated away from the Au target (cathode) by the negative electrical potential. The positive argon ions are accelerated toward the Au target bombarding the Au atoms (the radius of Au atom is 0.1441 nano-meter). Consequently, neutral Au atoms are ejected from the Au target and deposited on the grounded substrate. When the free electrons recombine with the positive argon ions, photons are emitted, introducing the deep purple color of plasma. A constant sputtering deposition rate remains until the desired thickness is achieved. In this research, the Au deposition was performed inside this sputtering chamber in figure 4.10. A 7.5 cm length of the Au target on the top of the

chamber was connected to a negative voltage (cathode), and a 10 cm length the stage at the bottom of the chamber was connected to ground where the sample was placed. The Au structures on the sample were not fully connected to each other due to the thin Au atomic deposition. A simulation of sputtered Au emitted toward the substrate formed clumpy cluster was presented [69].

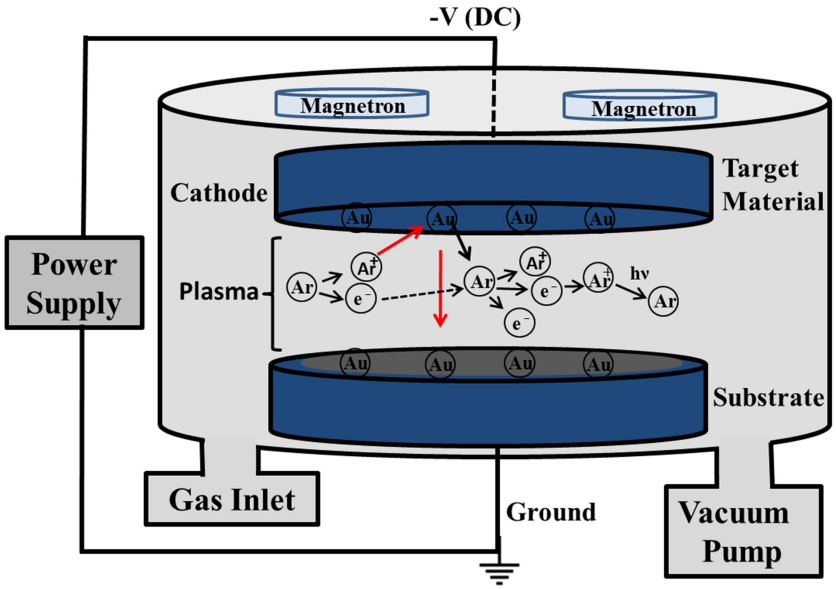

Figure 4.9 Schematic principle of DC powered magnetron sputtering system.

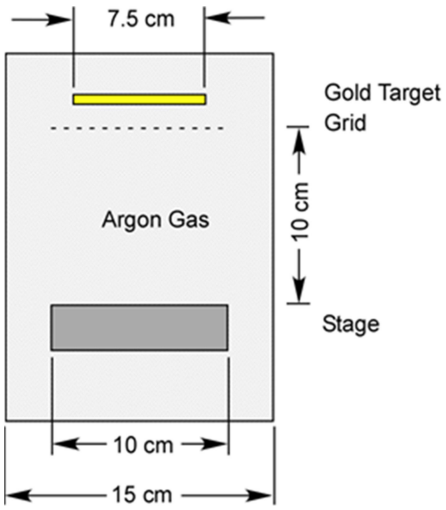

Figure 4.10 The dimensions of the DC powered magnetron sputtering system.

4.3. Au Deposition

As stated in subchapter 2.3, the main contributor to surface enhanced Raman scattering (SERS) localized surface plasmon resonances (LSPR), hot spots, are generated between the nano-gaps of metallic nanostructures. In this research, an Au thin film (figure 4.11) was deposited on a smooth side of the wafer by the DC powered magnetron sputtering system under 450 mA for 430 seconds. The Au thin film was measured by Alpha Step (D-100 KLA Tencor). The average thickness of sputtered Au was around 20 nm. The partially 80 nm thickness was caused by the thickness of the microscope slide on the wafer. A microscope slide was place on the wafer during the Au deposition, then it was removed during the thickness measurement, so accumulated 80 nm Au were observed.

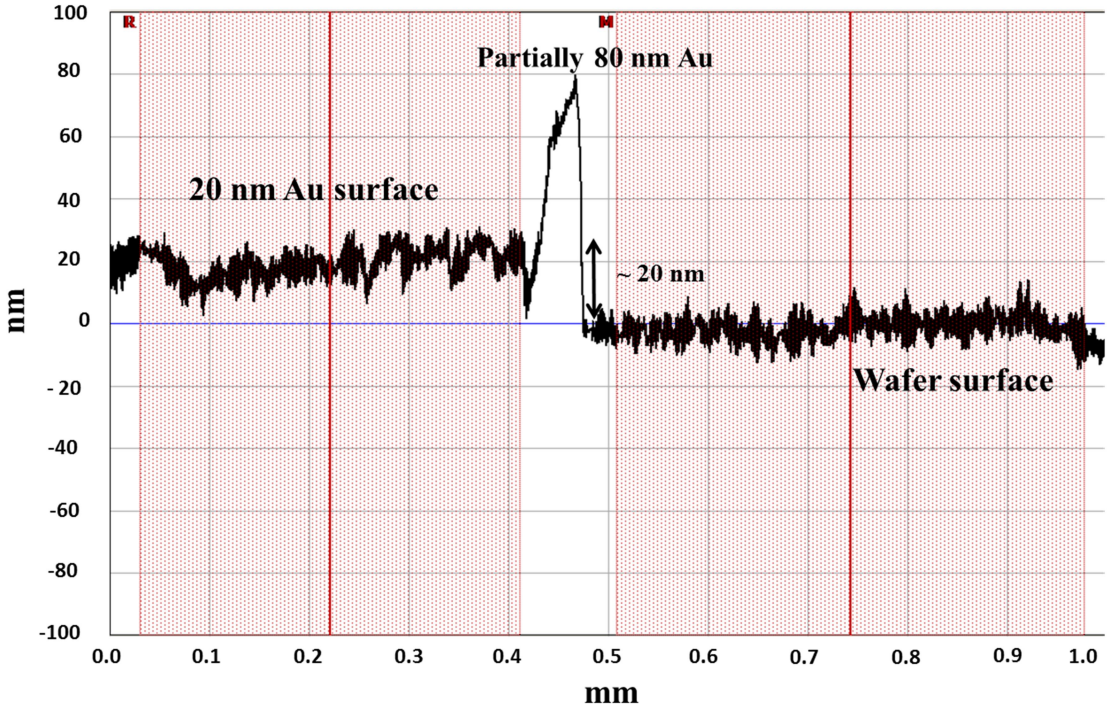

Figure 4.11 An 20 nm Au thin film on a smooth side of the wafer was fabricated by DC powered magnetron sputtering system and measured by Alpha Step (D-100 KLA Tencor).

The average sizes of 10 nm to 50 nm AuNIs are shown on the AFM and the SEM morphologic surface images in figure 4.12. The RMS of the AFM image [1.1 μm × 1.1 μm field of view] under 60 nm scale bar is around 9 nm. However, since the tip of AFM was blunt, not all the metallic nanostructures could be scanned thoroughly. The SEM image was therefore employed to resolve the metallic nanostructures shown in figure 4.12 (b) and (c). The RMS of Au thin film on the microscope slide is around 11 nm similar to the AFM measurement. All the SEM images were taken under 1k eV. The SEM morphologies of Au nanoislands (AuNIs) (clumps) on a microscope slide are similar to those on recent publication [65, 66, 70].

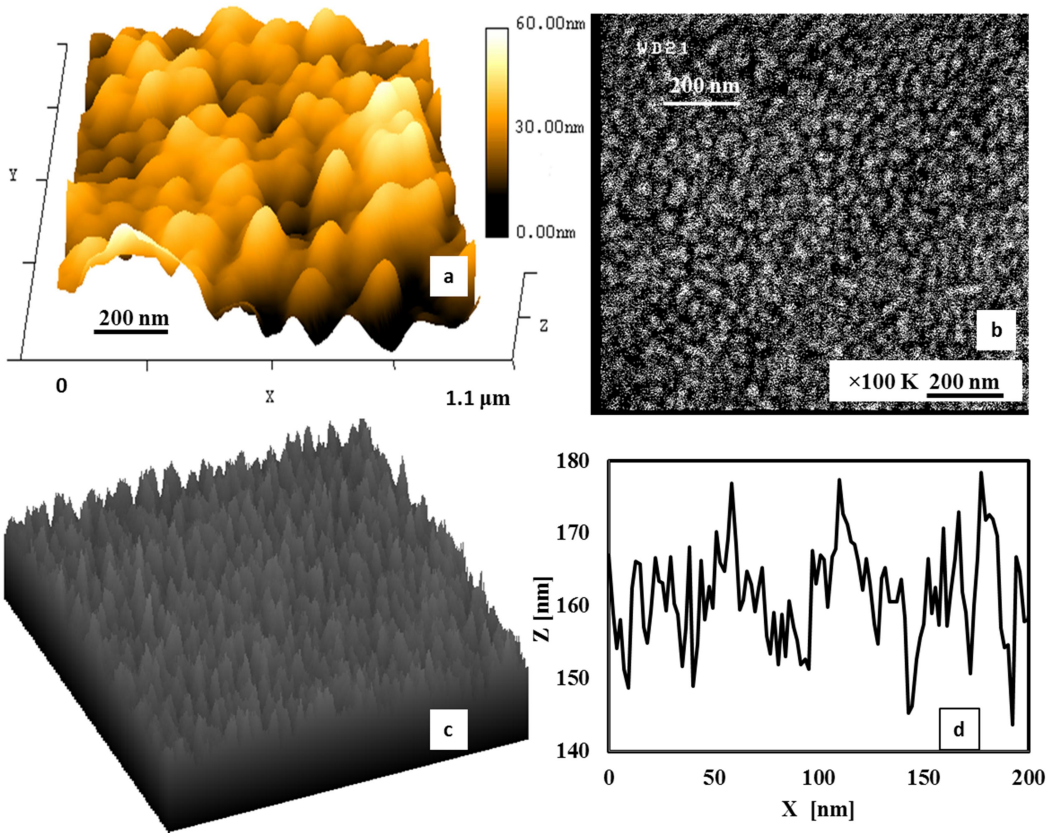

Figure 4.12 A 20nm Au thin film was sputtered on microscope slide. The field of view is 1.1 μm × 1.1 μm (a) The AFM image and the RMS is around 9 nm. (b) SEM image at 1kV. (c) Morphologic surface image. (d) The height distribution across the marked 200 nm line is shown below. The RMS height variation is 11 nm.

Aluminum foil was employed as a solid substrate for *in vitro* measurement and a sacrificial substrate for *in vivo* measurement. Three different types of aluminum foil substrates were prepared: 1. A non-etched aluminum foil. 2. An 60 second KOH etched aluminum foil. 3. An 60 second KOH etched-stirred aluminum foil. A 20 nm Au thin film was sputtered on non-etched, etched aluminum foils (figure 4.13). The AFM images [1.3 µm × 1.3 µm] under 135 nm scale bar shows that the quantity of AuNIs on the etched aluminum foil are more than its on the non-etched aluminum foil. The RMS height variations are (a) 12 nm and (b) 21 nm.

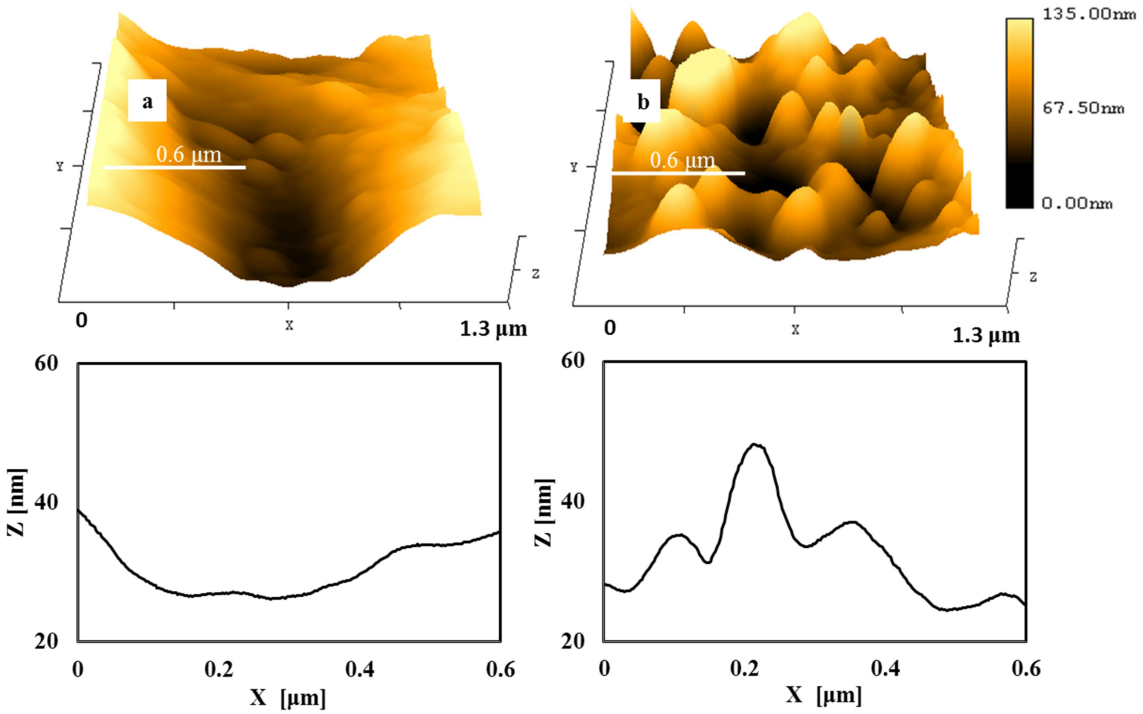

Figure 4.13 The AFM images [1.3 µm × 1.3 µm field of view] of a 20 nm Au thin film on (a) non etched aluminum foil (b) etched aluminum foil. The height distributions across 0.6 µm are shown below. The RMS height variations are (a)12 nm, and (b) 21 nm.

A 20 nm Au thin film was sputtered on the etched-stirred aluminum foil. Nano-gaps and sizes between AuNIs were observed by AFM and SEM (figure 4.14). The AFM image [1.3 µm × 1.3 µm field of view] under 35 m scale bar shows the AuNIs on the etched-stirred aluminum foil

is smaller on the etched aluminum foil. The quantity of AuNIs on the etched-stirred aluminum was more than the etched aluminum foil. Although the depths of grooves between AuNIs were not measurable, AFM images show considerable amount of saw-tooth shapes (AuNIs) on the Au surface (figure 4.14). The SEM height distribution across the marked 200 nm line is shown below, while the RMS height variation is 34 nm (figure 4.14). In summary, larger number of smaller AuNIs were obtained on an etched-stirred aluminum foil. Raman signals between 20 nm Au thin film on processed and unprocessed aluminum foils will be discussed on chapter 5.

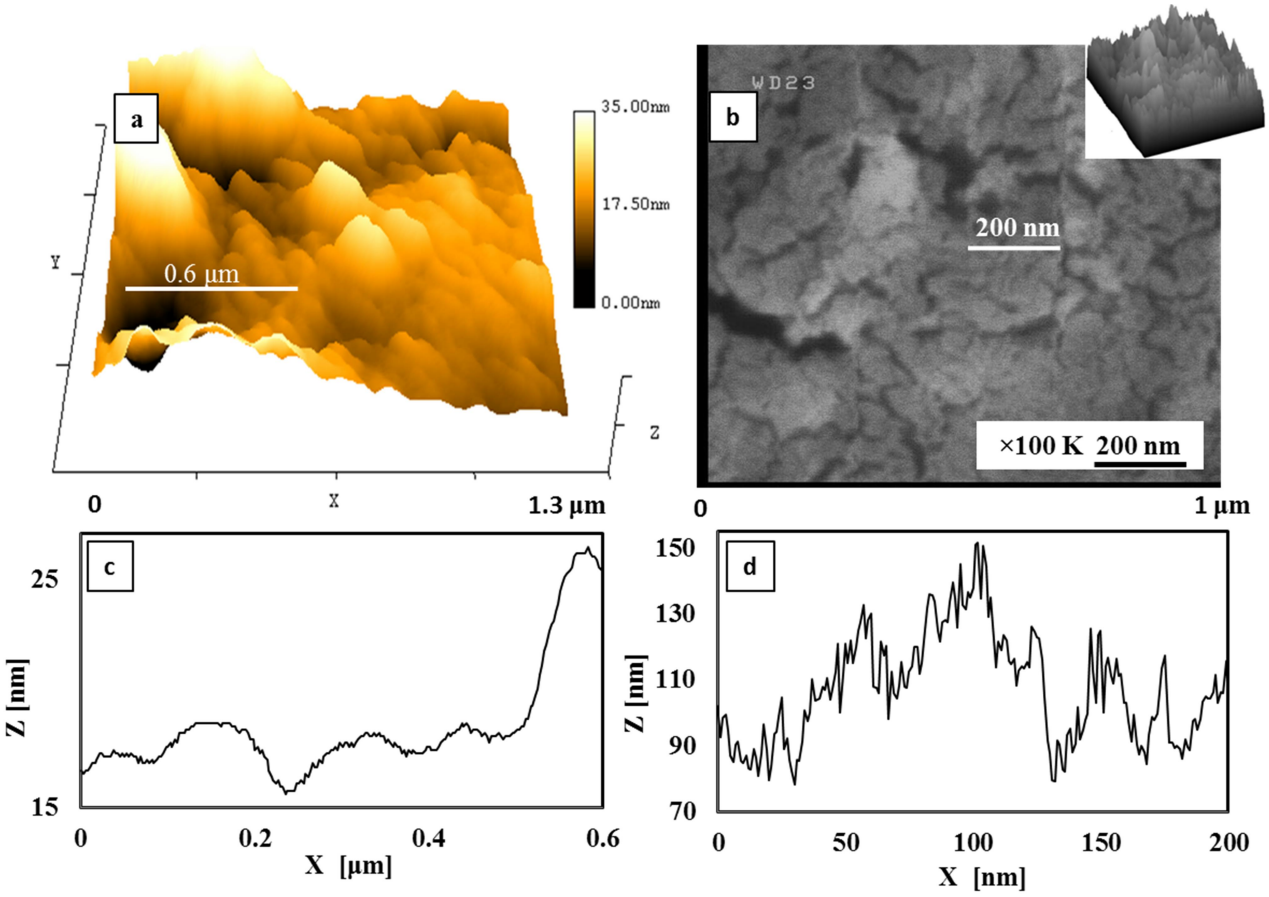

Figure 4.14 A 20nm Au thin film was sputtered on etched and stirred aluminum foil. The field of view is 1.3 µm × 1.3 µm (a) The AFM image (b) The SEM image under 1kV (c) The AFM height distribution across 0.6 µm, and the RMS variation is 7 nm (d) The height distribution across the marked 200 nm is shown below, and the RMS height variation is 34 nm.

4.3.1. Au deposition thicknesses and positions

Figure 4.9 shows the dimensions of the DC powered magnetron sputtering system. A wafer with etched-stirred, etched, non-etched aluminum foil substrates (figure 4.15) was placed on the stage between two walls of the chamber. A 14 cm length of the sample (2 sets of 7 cm strips) was placed inside the sputtering chamber. After Au deposition, the symmetric colors of the Au on aluminum substrates were violet, blue, light green, yellow, light green, blue and violet from edge to center and from center to edge (-7 cm to 7 cm) (figure 4.15 (b)). The color distribution shows that the Au was evenly disturbed on the center and gradually changed toward to the edges. Therefore, obtaining the Au thicknesses on aluminum substrates with respect to the colors by AFM image provides significant information for this SERS work, because it localizes the optimized Au thicknesses at strong Raman signals. However, it was difficult to measure the Au thicknesses distribution on the aluminum foil due to the initial large roughness of aluminum foils, but it was still doable if the thicknesses of Au on aluminum equals to the Au on the wafer. In order to minimize the distortion from initial roughness of aluminum foils, [1 μm x 1 μm field of view] small areas scanning is required.

The measurement of the Au thickness distribution on the wafer from position 2 cm to 7 cm is shown in figure 4.16. Position 2 cm to 7 cm (partially of the wafer) is taken out from -7 cm to 7cm (whole wafter). AFM (NT-MDT Titanium AFM) was operated to measure the Au thickness on the wafer across some positions. The Au thickness near the center was near 20 nm which is more less the same as the measurement in figure 4.11. The Au thicknesses from center to edge linearly decrease with respect to the positions from 17.9 to 6.6 nm (figure 4.16). The comparison of Au thicknesses on the wafer with respect to the positions is shown in table 4.5.

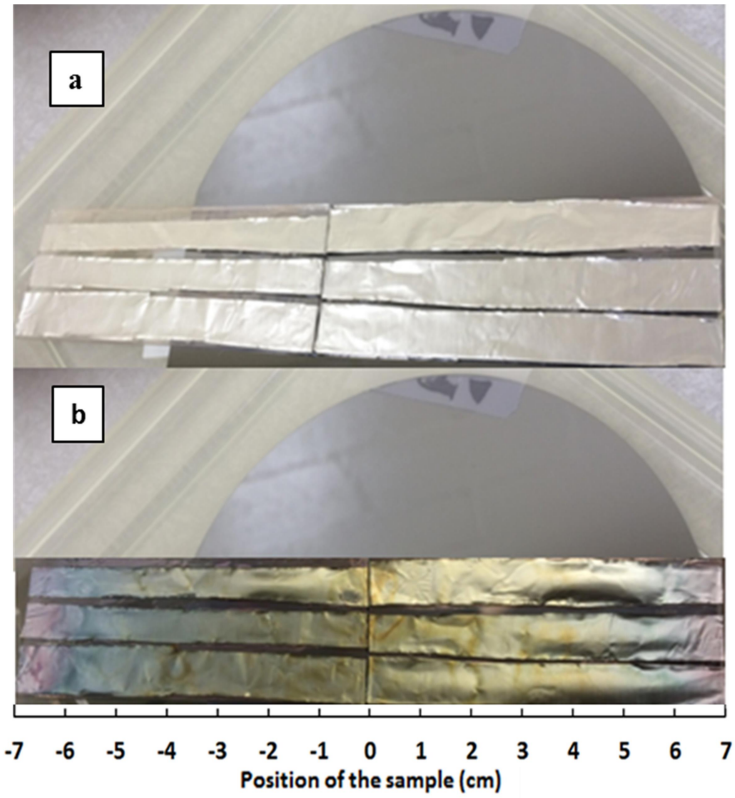

Figure 4.15 Sputtered Au on wafer with etched-stirred, etched, nonetched aluminum substrates (Position -7 cm to 7cm) (a) before, (b) after Au deposition.

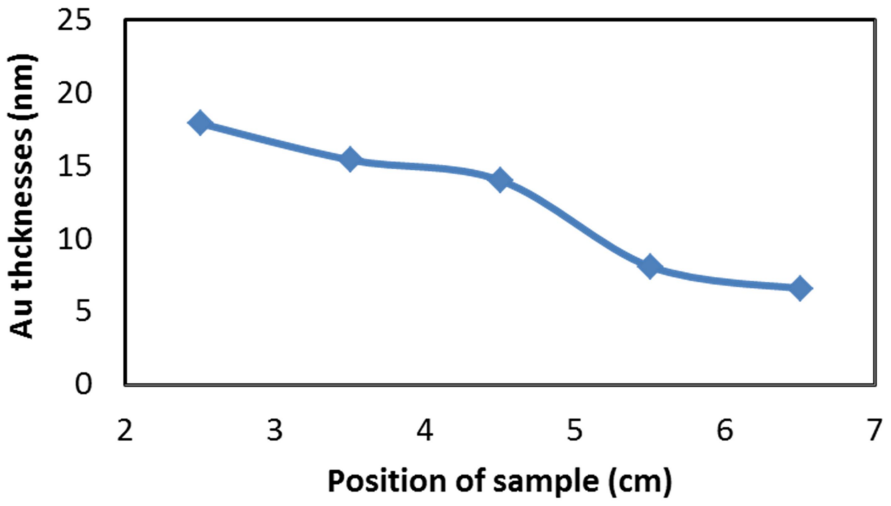

Figure 4.16 Au thicknesses on the wafer with respect to position (2 cm to 7cm).

Table 4.5 The comparison of Au thicknesses on the wafer with respect to the positions.

Position (cm)	**2~3**	**3~4**	**4~5**	**5~6**	**6~7**
Thickness (nm)	17.9	15.4	14	8.1	6.6
Average Size (nm)	29.7	28.3	44.3	31.7	23
Majority Size Range (nm)	15~35	15~35	30~60	20~35	15~25
Detected Particles (μm^2)$^{-1}$	101	135	323	640	1043

The AFM images [1 μm × 1 μm field of view] shows the 6.6 nm Au thickness with average 23.4 nm Au particle size (the majority size range 15~ 25 nm), and 1043 detected Au particles per μm^2 area at position of 6~7 cm (figure 4.17). This position produced the thinnest Au layer, the smallest Au particle size, and a large number of Au particles.

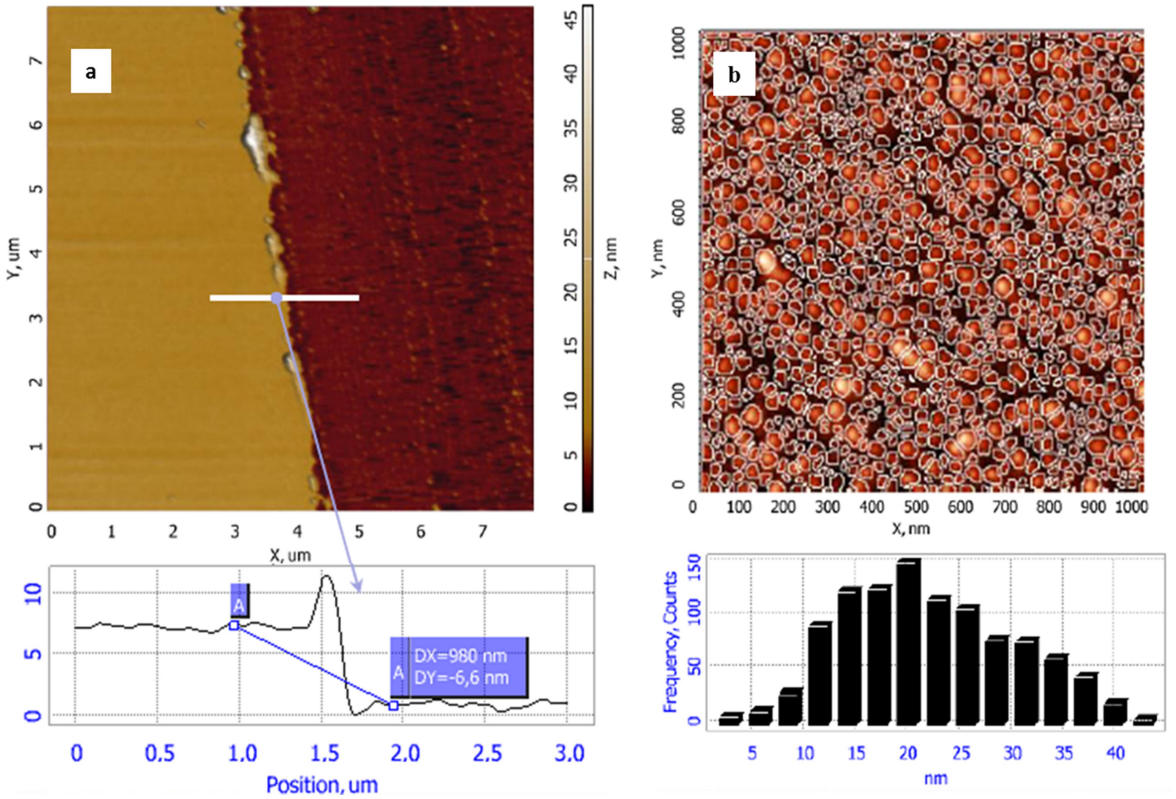

Figure 4.17 The AFM images at 6~7 cm position (a) Au thickness on the wafer, (b) detected Au particle sizes and numbers [1 μm × 1 μm field of view].

For 5~6 cm position (figure 4.18), the Au thickness was 8.1 nm with average 31.7 nm Au particle size (majority size range 20~ 35 nm), and 640 detected Au particles. At this point, the Au clumps accumulated into bigger and thicker clumps compared to the position 6.5 cm, so that the number of the Au particles decreased.

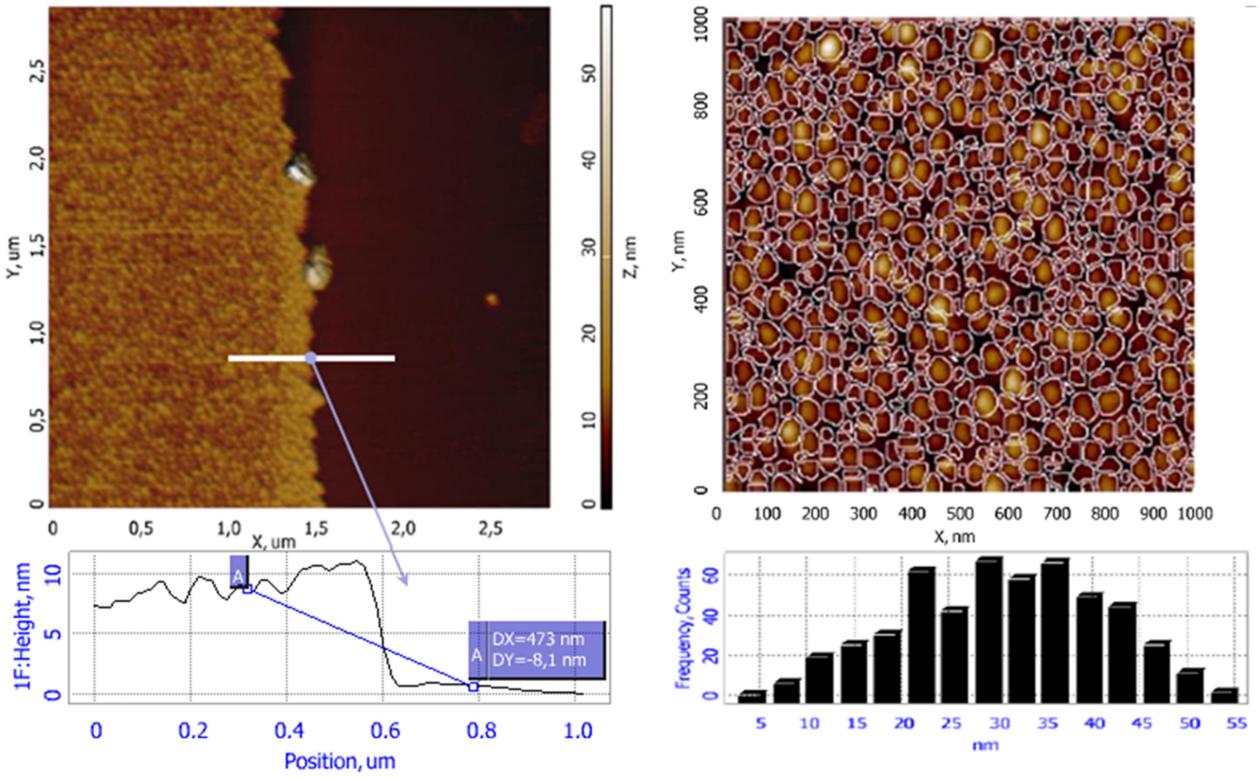

Figure 4.18 The AFM images at 5~6 cm position (a) the Au thickness on the wafer, (b) the detected Au particle sizes and numbers [1 μm × 1 μm field of view].

At position of 4~5 cm (figure 4.19), Au thickness was 14 nm with average 44.3 nm Au particle size (majority size range 30~60 nm) and 323 detected Au particles. This spot produced larger Au particle size and wider particle size range. At this point, the Au clumps accumulated

into bigger and thicker clumps compared to the position 5~6 cm, so that the number of the Au particles decreased again.

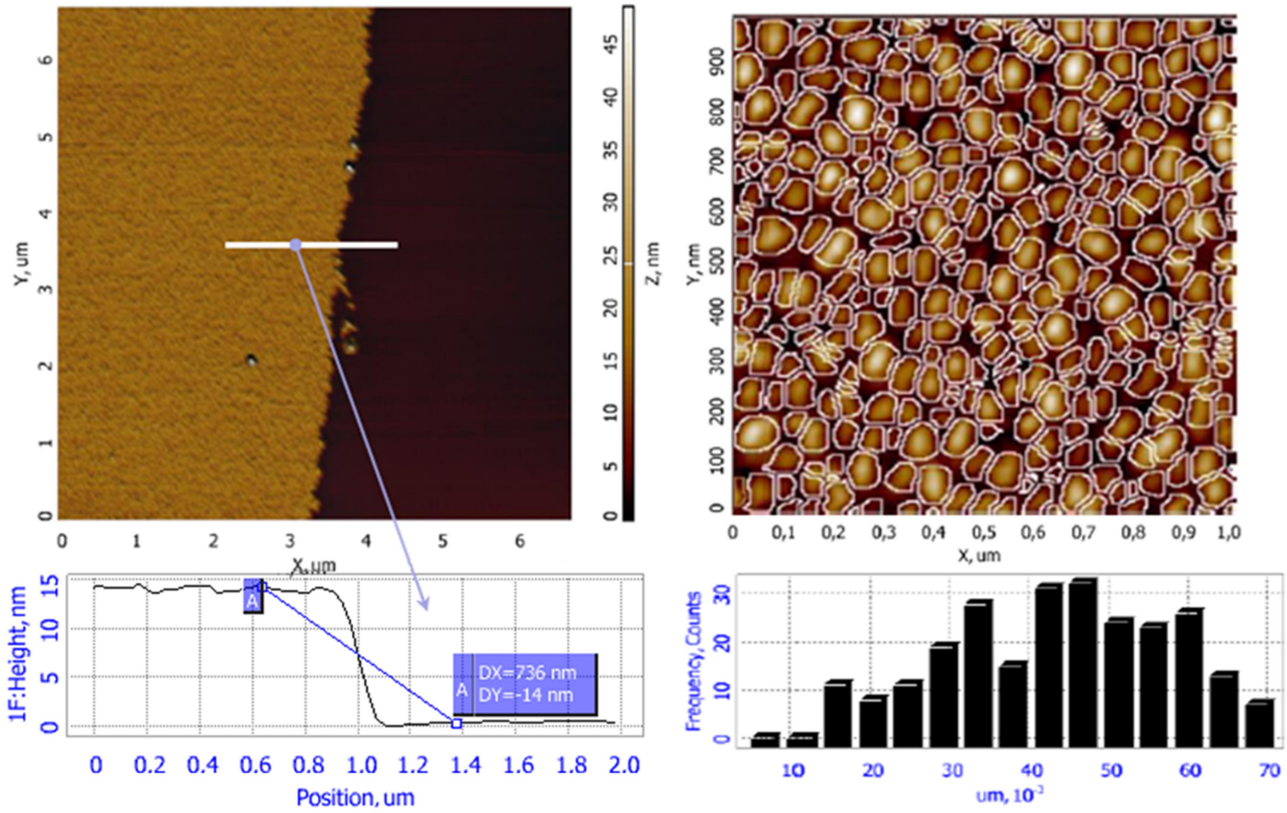

Figure 4.19 The AFM images at 4~5 cm position (a) the Au thickness on the wafer, (b) the detected Au particle sizes and numbers [1 μm × 1 μm field of view].

For position of 3~4 cm (figure 4.20), Au thickness was 15.4 nm with average 28.3 nm Au particle size (majority size range 15~ 35 nm) and 135 detected Au particles. At this point, the Au clumps accumulated thicker clumps but it shrunk on the size compared to the position 4~5 cm, so that the number of the Au particles decreased again.

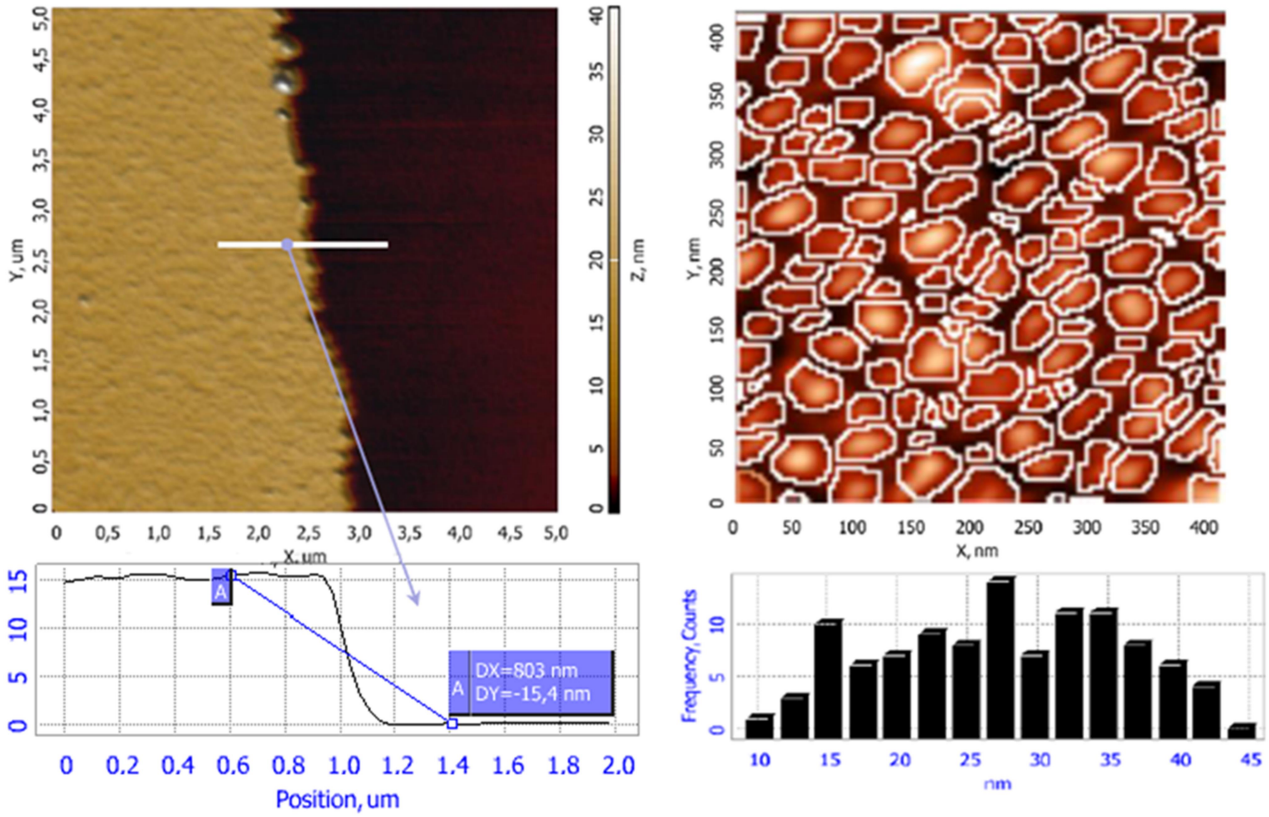

Figure 4.20 The AFM images at 3~4 cm position (a) the Au thickness on the wafer, (b) the detected Au particle sizes and numbers [1 μm × 1 μm field of view].

At 2~3 cm position (figure 4.21), Au thickness was 17.9 nm with average 29.7 nm Au particle size (majority size range 15~ 35 nm) and 101 detected Au particles. At this point, the Au clumps accumulated thicker clumps, but it remained at same size compared to the position 3~4 cm, so that the number of the Au particles decreased again.

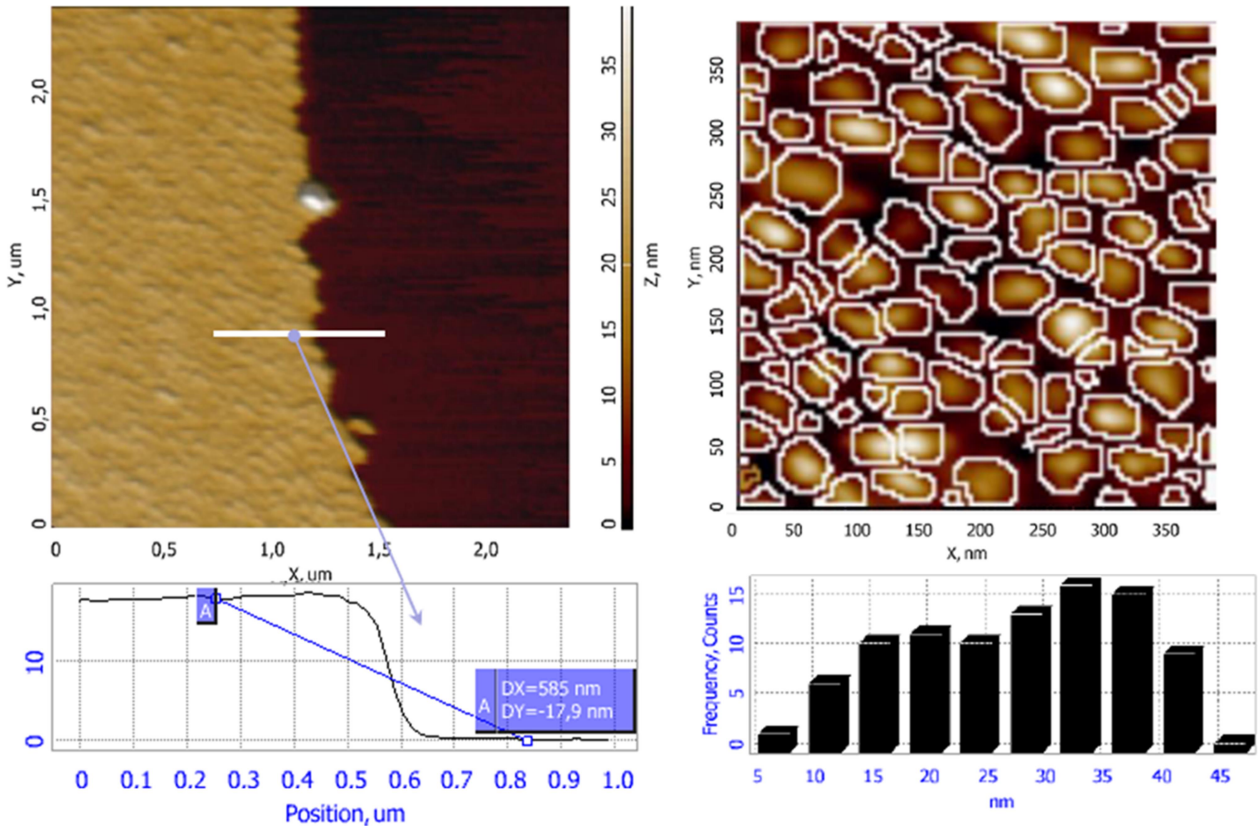

Figure 4.21 The AFM images at 2~3 cm position (a) the Au thickness on the wafer, (b) the detected Au particle sizes and numbers [1 μm × 1 μm field of view].

Around 14 nm Au thin film was sputtered on etched-stirred aluminum foil around position 4~5 cm. Nano-gaps and sizes between AuNIs were observed by AFM and SEM (figure 4.22). The AFM image [1.3 μm × 1.3 μm field of view] under 65 m scale bar shows that the AuNIs around the edge of the etched-stirred aluminum foil is smaller than on center of the etched-stirred aluminum foil. Moreover, table 4.5 shows that the quantity of AuNIs on edge of the etched-stirred aluminum is more than on center of the etched-stirred aluminum foil. Although the depths of grooves between AuNIs were not measurable, AFM image shows considerable amount of saw-tooth shapes (AuNIs) on the Au surface (figure 4.22). The SEM height

distribution across the marked 200 nm line is shown below, while the RMS height variation is 32 nm.

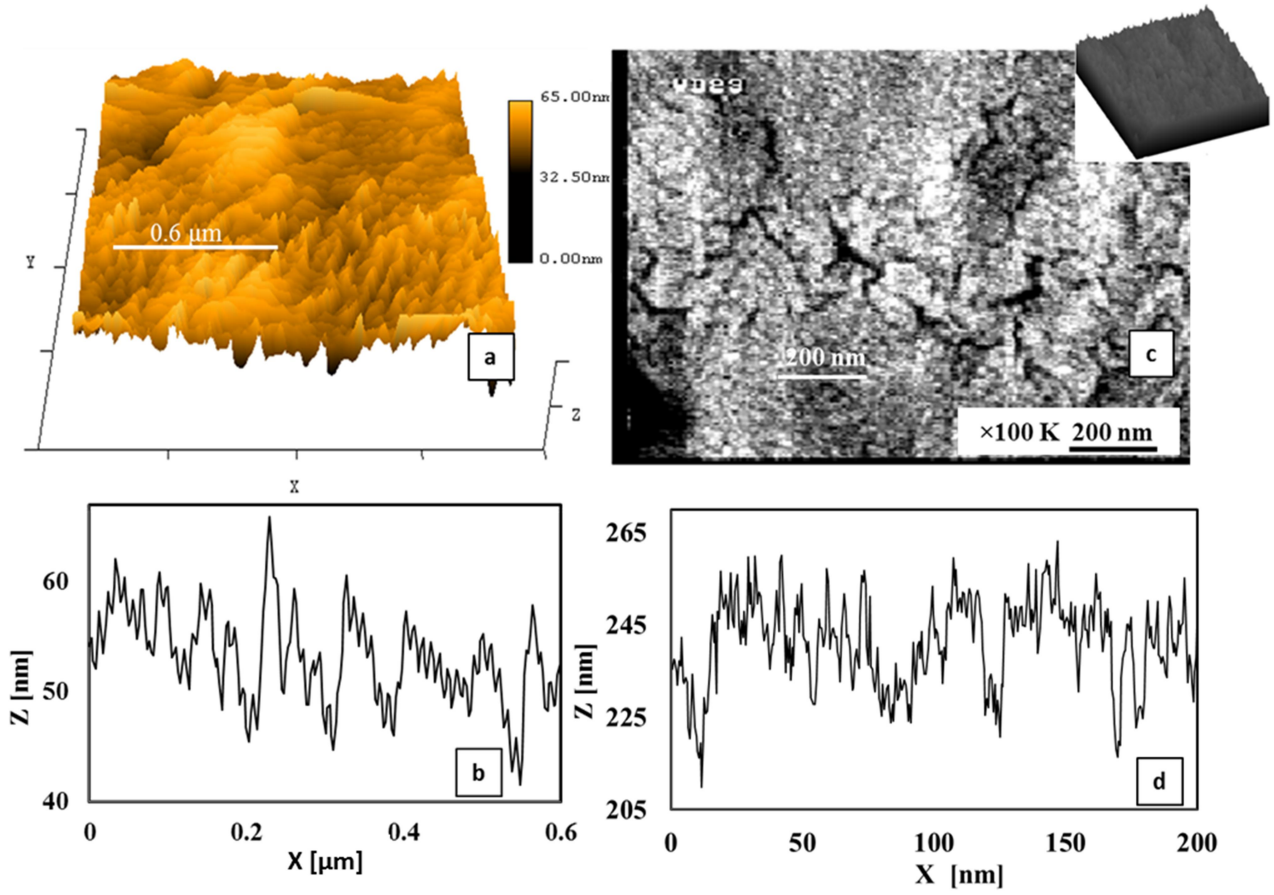

Figure 4.22 Around 14 nm Au sputtered on stirred etched aluminum foil on scale [1.3 µm × 1.3 µm] on the edge of the stage (a) The AFM images (b) The AFM height distributions across 0.6 µm, and the RMS variation is 13 nm (c) The SEM image under 100 K (d) The SEM height distributions across 200 nm, and the RMS height variation is 32 nm.

In summary, if the Au thicknesses on the aluminum foils equaled the Au thicknesses on the wafer, the different types of Au structures were fabricated across the stage inside the 15 cm length chamber: One was the Au structure around center of the stage, in which produced less numbers of average 30 nm size Au particles with 15~35 nm particle range (from 2~4 cm position). One was the Au structure around the edge of stage, in which produced more numbers of different sizes of Au particles with different particle size ranges (from 4~7 cm position). Moreover, table 4.6 shows the RMS from sputtered Au on different condition substrates. RMS from sputtered Au on etched aluminum (RMS= 21 nm) was rougher than on non-etched aluminum and on glass slide (RMS= 11, 12 nm). By adding etched-stirred parameter, the RMS increased from 21 to 34 nm. However, there is no significant RMS different between Au on etched-stirred aluminum (center) and Au on etched-stirred aluminum (edge). The Raman signals at each position of Au thin film on non-etched, etched, etched-stirred aluminum foils will be discussed on chapter 5.

Table 4.6 The comparison of RMS from sputtered Au on different condition substrates.

Sputtered Au on	**RMS (nm)**
Glass Slide	11
Non etched Al	12
Etched Al	21
Etched-stirred Al (Center)	34
Etched-stirred Al (Edge)	32

4.4. *In Vitro* and *In Vivo* applications

There were two types of applications in this research: *in Vitro* (conventional system) and *in Vivo* (Probe system). Figure 4.23 shows the differences in the setups between the conventional arrangement and the probe arrangement. For *in vitro* measurements, the specimen has to be transparent, so that laser light may pass through the specimen and reach the rough metallic surface. For *in vivo* measurement, the substrate has to be transparent, so that laser light may pass through substrate to reach the rough metallic surface. In other words, the conventional system looks down at the rough metallic surface through the specimen, and the probe system looks down at the specimen through the rough metallic surface. Since the specimen does not have to be transparent for the *in vivo* setup, opaque tissues can be observed even inside a patient's body.

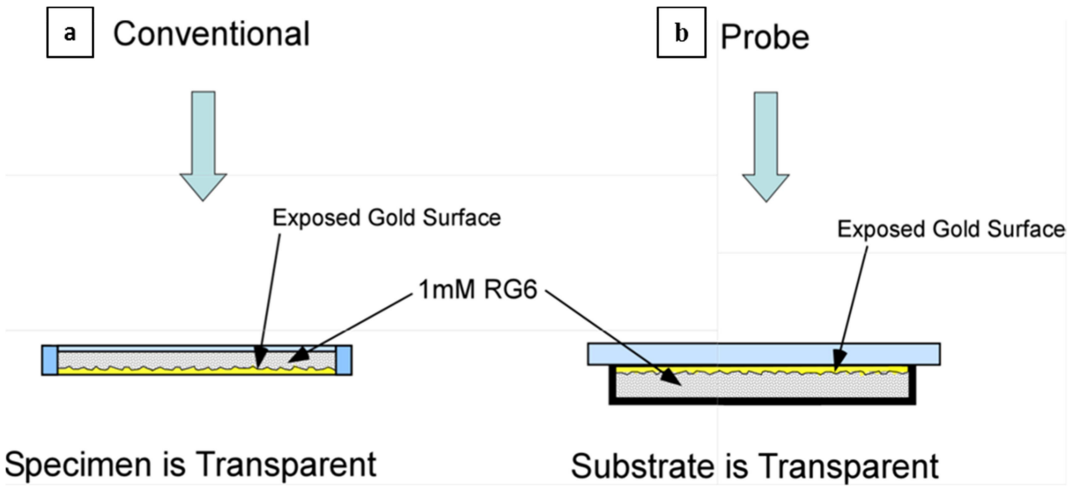

Figure 4.23 Schematic of clinical application systems (a) *in vitro* (b) *in vivo* observing a test specimen of R6G solution.

In this research, the *in vivo* (probe) system was fabricated by these standard steps:

1. The aluminum foil was etched-stirred by 30% KOH for 60 second, which removed 1 μm thickness.

2. A 20 nm Au thin film was sputtered on the etched-stirred aluminum.

3. A Few drops of transparent ultraviolet (UV) curable epoxy (Norland Optical Adhesive 68, Edmund Optics America) was applied between the Au layer and a cover slip or a graded- index lens (GRIN lens). The UV epoxy uniformly spread between the Au layer and the cover slip and formed a transparent plastic film around 400 μm thick. The thickness of UV epoxy was determined by the thickness of silicon walls at the edge of the sample. The UV epoxy was employed in this research, because it provides a strong mechanical bond between the glass and the deposited gold.

4. The UV Epoxy substrate was exposed under a 13 W UV lamp for 10 hours to cure.

5. The aluminum foil was etched in dilute 6% KOH at room temperature for 2 hours. Low concentration KOH has a lower etching rate and a lower reaction temperature protecting the Au layer on the UV epoxy substrate.

6. The partially transparent Au thin film attached on transparent epoxy substrate was rinsed in DI water.

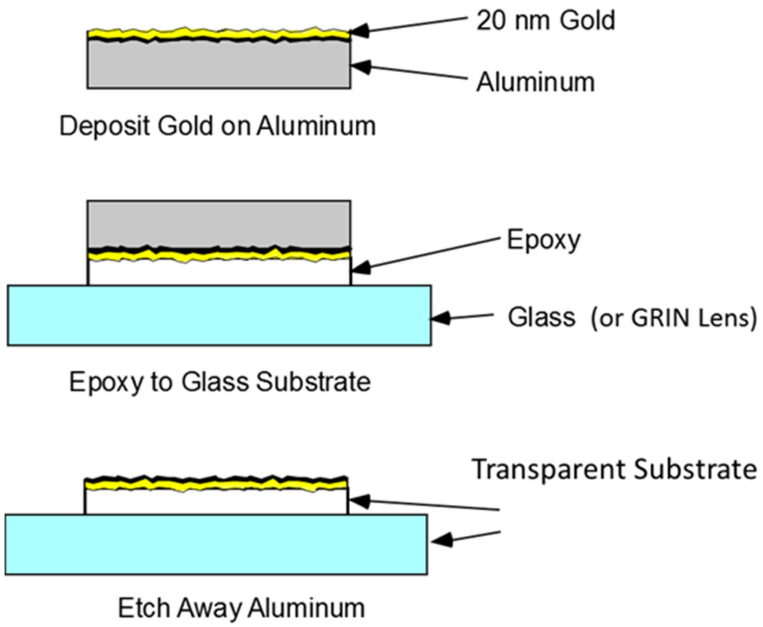

Figure 4.24 Schematic of the fabrication of in Vivo (probe) system.

The Au thin film on clear epoxy was fabricated by the procedures described in this chapter. Two AFM images over a 1.3 μm × 1.3 μm field of view with a 30 nm scale show RMS height variations of (a) 4 nm and (b) 8 nm, respectively. This Au thin film was deposited on the etched-stirred aluminum sacrificial substrate, so one might expect the AuNIs pattern on the surface to be the same as in figure 4.22. However, the images show that the surface structure of Au on clean epoxy is different from Au on the etched-stirred aluminum foil (figure 4.22 versus figure 4.25). The reason will be discussed on chapter 5. Raman signals from Au thin films on clear epoxy for *in vivo* applications will also be discussed on chapter 5.

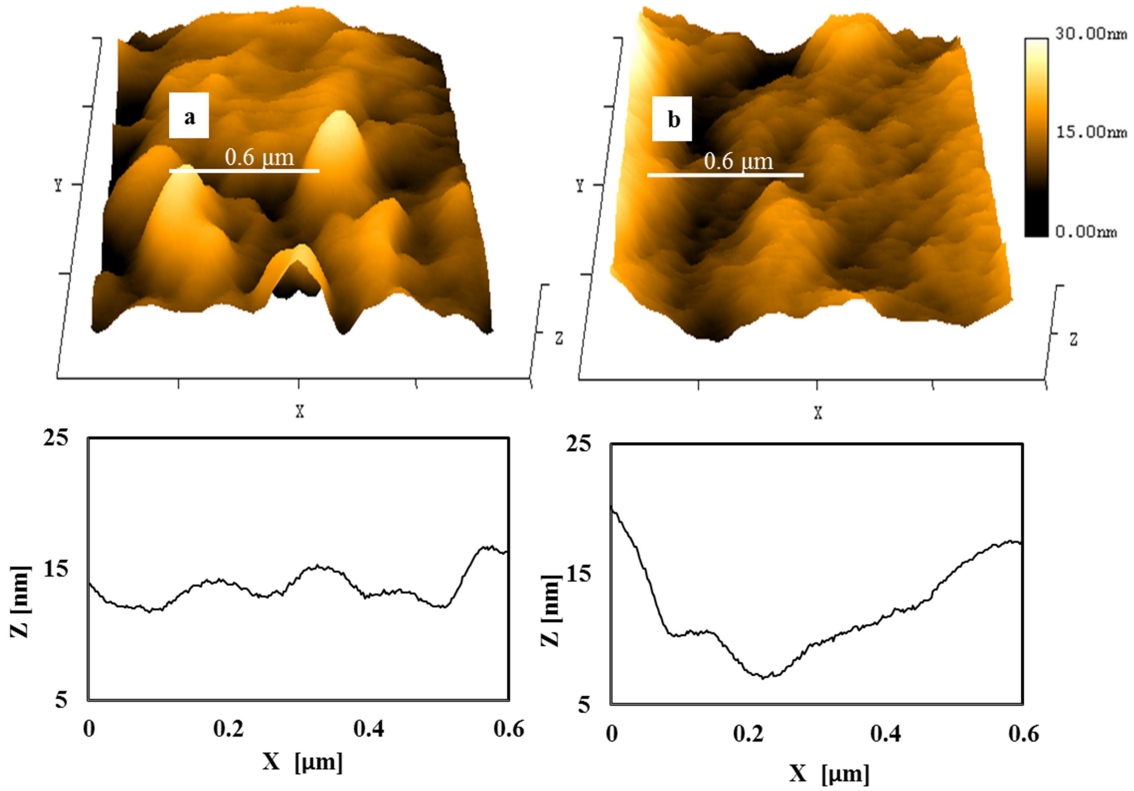

Figure 4.25 AFM images [1.3 µm × 1.3 µm field of view] of Au thin film on clear epoxy. The height distributions across 0.6 µm are shown below. The RMS height variations are (a) 4 nm, and (b) 8 nm.

CHAPTER 5: SURFACE-ENHANCED RAMAN SCATTERING (SERS) MEASUREMENTS

5.1 Preparation of Target Material

5.1.1. Rhodamine 6G (R6G) and Test Cells

Rhodamine 6G (R6G) dye is widely employed in biomedical applications due to its chemical stability and easy detection. The chemical formula of R6G is $C_{28}H_{31}N_2O_3Cl$. The solubility and molecular weight of R6G are 20 g/L and 479.01 g/mole [71]. Some examples of its use in enzyme-linked immune sorbent assay (ELISA) [72], fluorescence correlation spectroscopy [73], flow cytometry [74], fluorescence microscopy [75], and surface Raman enhanced scattering (SERS) [76]. In this research, R6G acted as a specimen solution for the SERS detection. The RG6 powder was dissolved in deionized water at temperature 50-60°C stirring thoroughly at least 3 to 4 hours with ultrasonic treatment, and then left at room temperature 1 hour to cool. It was prepared in steps of a factor of 10 in different concentrations from 1 mM to 1 nM. R6G solution is transparent at low concentrations, but it turns to reddish above 1 μM concentration as shown in figure 5.1. The recipe of 1nM to 1mM R6G was as follows: the atomic standard weight of $C_{28}H_{31}N_2O_3C$ is $12 \times 28 + 1.008 \times 31 + 14.007 \times 2 + 15.990 \times 3 + 12.011 = 479.0$. The molar concentration of 10 mM was made by 4.7901 *gram* R6G with 1 L deionized water (4.7901 *gram*/479.01)/ 1 *L*, which is under the saturation point 20 *gram* / 1 L. Then, it was diluted by successive factors of 10 for lower R6G concentration solutions. Other specimen solutions such as 2-mercaptoethanol citrate, azobenzene, pyridine and cyanine dyes are also employed for SERS detections.

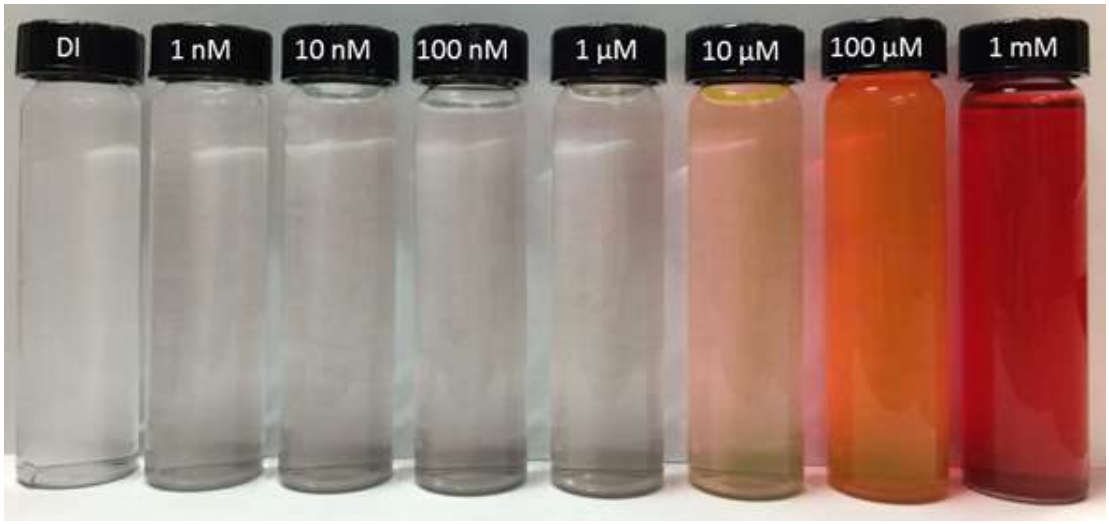

Figure 5.1 Different concentrations of Rhodamine 6G solutions from low to high.

5.1.2 Measurement Setup of Surface-Enhanced Raman Scattering (SERS)

Test cells (figure 5.2) were constructed from microscope slides (2"x3"and 1"x3"), cover slips (2"x2"), and stainless steel tubes (D=1 mm). Each part was bonded by a transparent epoxy. The volume of the cell was about 0.1 mL. 20 nm Au deposited on different substrates was placed inside the test cell in contact with the RG6 solutions (figure 5.2).

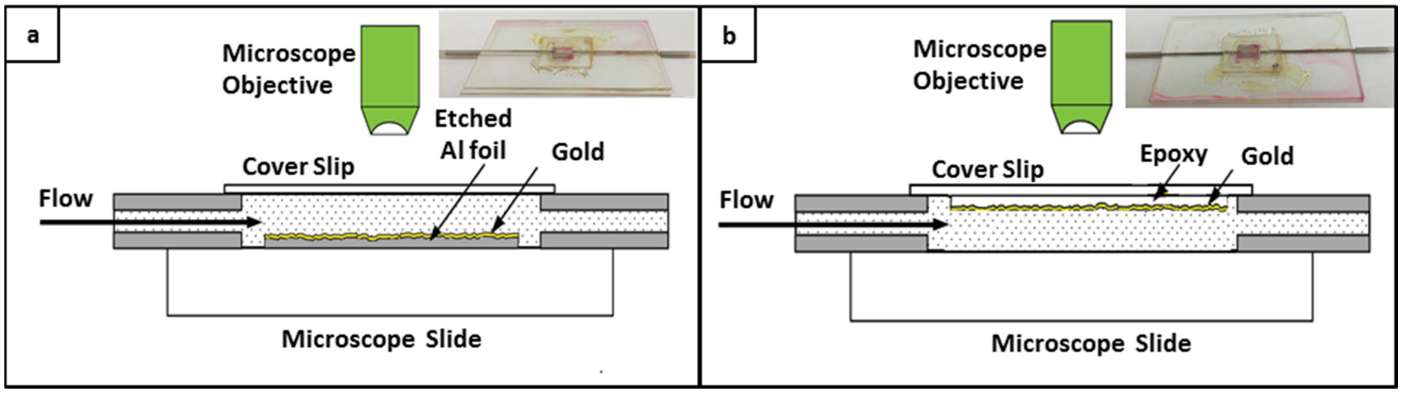

Figure 5.2 Test cells were filled with Rhodamine 6G. Laser light was focused on Au substrate in two cases by a 50 X microscope objective. (a) Au on etched aluminum foil (conventional view), (b) Au on UV epoxy (transmission view).

Raman spectra were obtained from a Raman spectrometer (LabRAM Raman Spectrometer) with an incident He Ne laser at 633 nm wavelength. By choosing a 50 X long working distance microscope objective, the laser light was focused either on the Au on processed aluminum foil (front surface of the gold) though the cover slip and the Rhodamine 6G solution (Fig. 5.2 a), or on Au on epoxy substrate through the cover slip and the epoxy substrate (Fig. 5.2 b). The measurements were taken in the order of 1 nM to 1mM R6G solution to minimize contamination errors. For each measurement, at least 1mL R6G solution was injected into the test cell by syringe to wash out the previous R6G concentration. Figure 5.3 shows prominent reference peaks of R6G Raman spectrum 614 cm^{-1}, 1310 cm^{-1}, 1363 cm^{-1} and 1509 cm^{-1}, in which 1363 cm^{-1} presents the highest intensity [77]. Therefore, the intensity at the prominent peak 1363 cm^{-1} was used as a measure of the Raman Signal in this research.

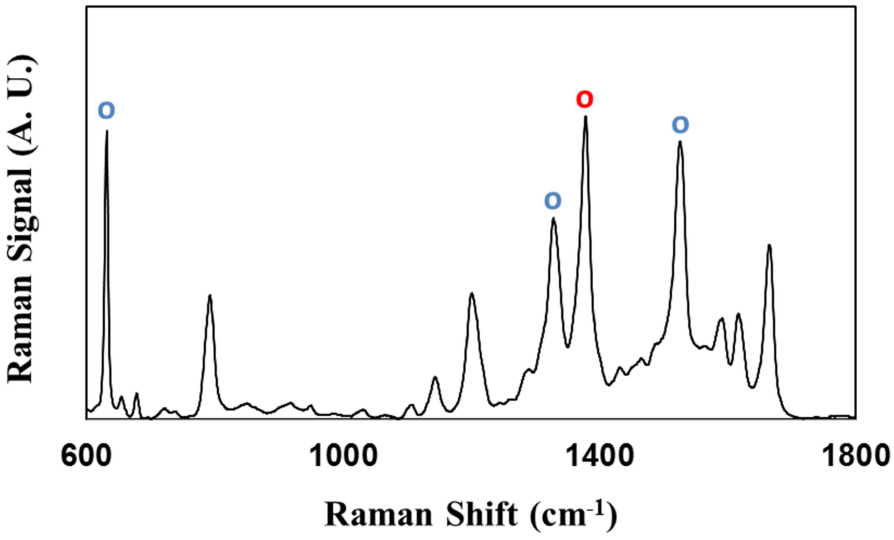

Figure 5.3 Prominent reference peaks of R6G Raman spectrum at 614 cm^{-1}, 1310 cm^{-1}, 1363 cm^{-1}, 1509 cm^{-1}, and the main peak at 1363 cm^{-1}[77].

5.2. Different Aluminum Substrates

Different aluminum substrates (aluminum foils, aluminum pellets (shot) 99.999%, and shop grade aluminums) were used followed by the cleaning, and etching procedures discussed in chapter 4. In this subchapter, three different aluminum substrates and six different aluminum foils in contact with 1mM R6G were analyzed by Raman spectrometer.

The Raman spectra were obtained from three different conditions of the front and back sides of aluminums foils in contact with 1 mM Rhodamine 6G solution (figure 5.4): Non-etched aluminum foils (a) front, and (b) back side. Etched aluminum foils (c) front, and (d) back side. Etched- stirred aluminum foils (e) front, and (f) back side. The Raman spectra were also obtained from (a) non-etched and (b) etched aluminums pellets in contact with 1 mM Rhodamine 6G solution (figure 5.5). Lastly, the Raman spectra were obtained from (a) non-etched and (b) etched shop grade aluminum in contact with 1 mM Rhodamine 6G solution (figure 5.6).

In summary, the Raman signals from the back side of bare aluminum foils were slightly stronger than the front side of bare aluminum foil. Moreover, the Raman signals from the etched aluminum substrates were stronger than non-etched aluminum substrate. The etching process increases the Raman signal by cleaning the surface of the aluminum and making its surface rougher. The results match the morphologies of AFM images in chapter 4, in that rougher surfaces produce stronger Raman signals. However, the Raman intensity at the 1363 cm^{-1} Raman line does not vary greatly from the back side of aluminum foils, aluminum pellets and shop grade aluminums.

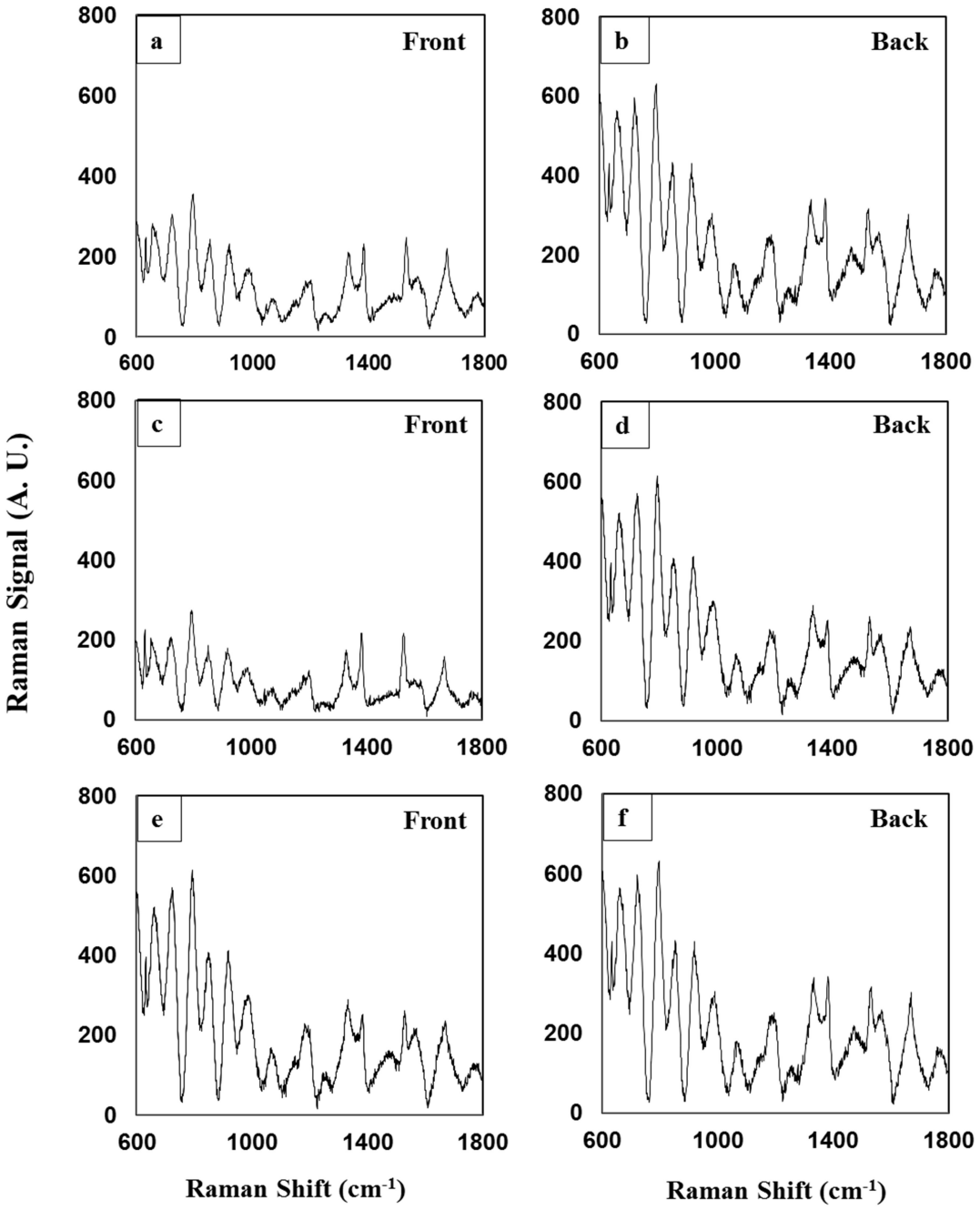

Figure 5.4 Raman spectra were obtained from different conditions of aluminum foils in contact with 1 mM Rhodamine 6G solution. Non-etched (a) front, and (b) back side. Etched (c) front, and (d) back side. Etched and stirred (e) front, and (f) back side.

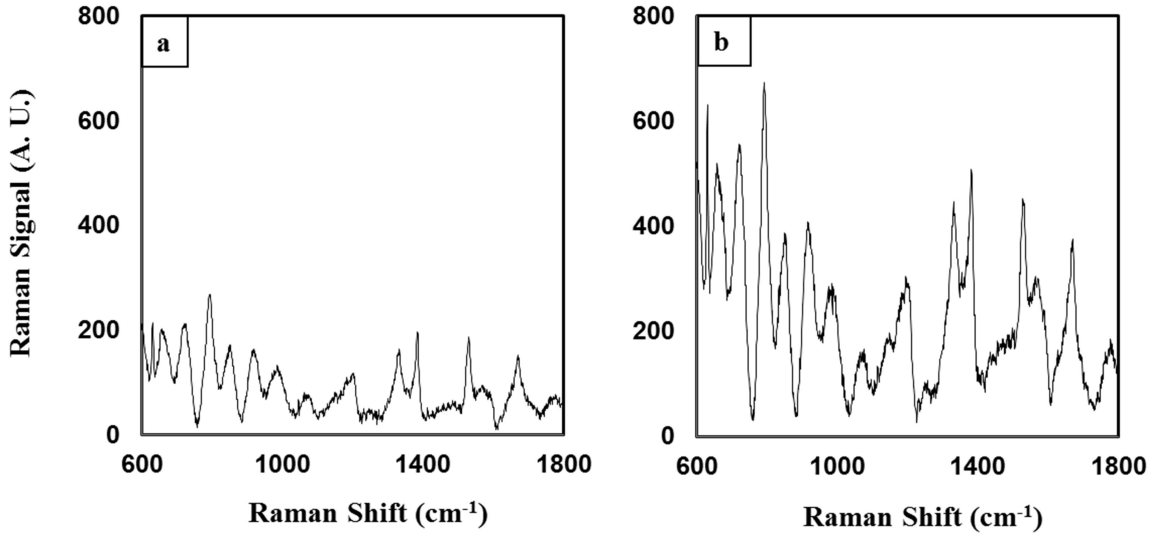

Figure 5.5 Raman spectra were obtained from different conditions of aluminum pellets in contact with 1 mM Rhodamine 6G solution (a) non-etched and (b) etched.

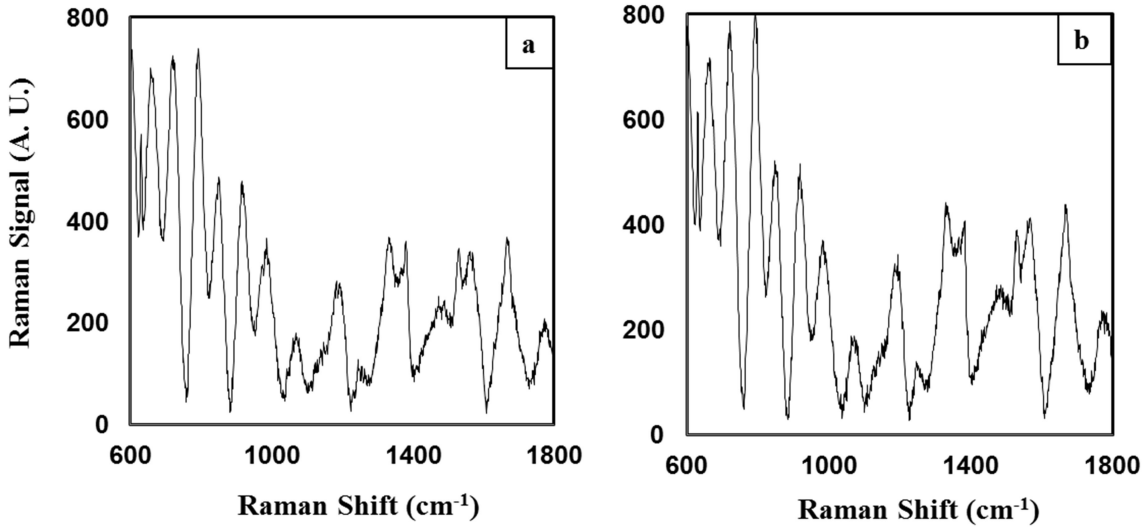

Figure 5.6 Raman spectra were obtained from different conditions of shop grade aluminums in contact with 1 mM Rhodamine 6G solution (a) non-etched and (b) etched.

5.3 Au on Aluminum Substrates with Different Wet Etching Times

In previous subchapter 5.2, Raman signals from three different aluminum substrates were similar. The etching process not only cleaned the substrate but also increased the surface roughness. Moreover, the AFM and SEM images in subchapter 4.1.2 show that the etched aluminum has more structure than non- etched aluminum. Therefore, SERS effect may be depend on etching time. The Raman signal from different etching time aluminum substrates and Au on different etching time aluminum foils will be discussed in this subchapter.

For bare aluminum substrates, the Raman spectra were obtained from different conditions of the substrates in contact with 1 mM Rhodamine 6G solution (figure 5.7 and table 5.1) Aluminum pellets and shop grade were etched at different times: 0, 10, 30, 60, and 120 seconds. The Raman intensity at the 1363 cm^{-1} Raman line shows that 60 seconds etching time on both samples produced a higher Raman signal. Au on aluminum pellets and aluminum foils with different etching times were also measured.

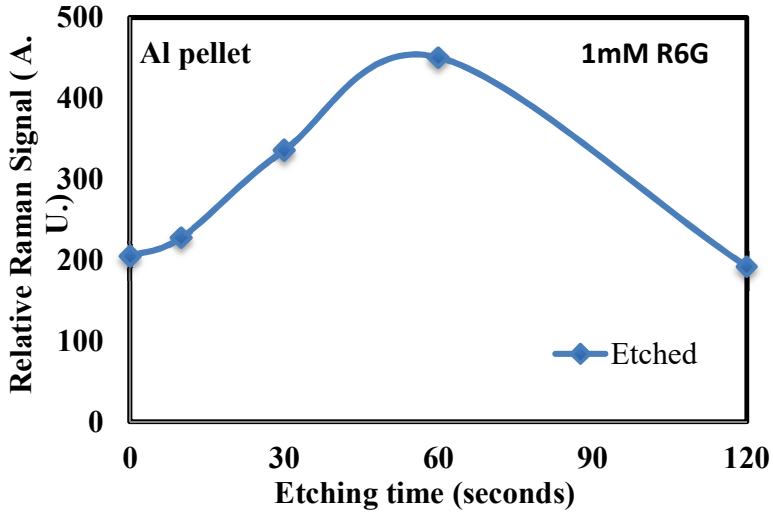

Figure 5.7 Raman signal with respect to different etching times at aluminum pellets.

Table 5. 1 Raman signal with respect to 7 different conditions of aluminum substrates.

Al Pellet and shop grade	Raman Signal (Ave.)
a. Non-Etched Pellet 0s	205
b. Etched Pellet 10s	228
c. Etched Pellet 30s	336
d. Etched Pellet 60s	451
e. Etched Pellet 120s	192
f. Non-Etched shop grade 0s	303
g. Etched shop grade 60s	422

Raman spectra were obtained from Au on 4 different conditions of aluminum foils in contact with 1 mM Rhodamine 6G solution (figure 5.8). Aluminum foils were etched at different times: 0, 10, 60, and 120 seconds. The Raman intensity at the 1363 cm^{-1} Raman line shows that Au on 60 seconds etching time aluminum foil produced the highest Raman signal.

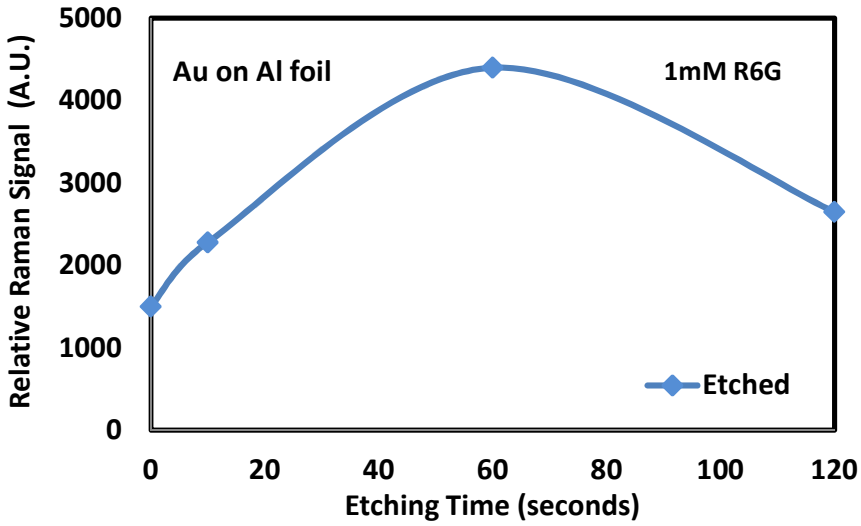

Figure 5.8 Raman signal with respect to Au on different etching time aluminum foils.

Etched-stirred parameter was also considered in this discussion. Raman spectra were obtained from Au on differently processed aluminum pellets in contact with 1 mM Rhodamine 6G solution (figure 5.9). Aluminum pellets were etched at different etching and etching-stirring times: 0, 10, 30, 60, 80, and 120 seconds). The Raman intensity at the 1363 cm^{-1} Raman line shows that Au on 60 seconds etching time aluminum pellet produced a higher Raman signal, the same as Au on stirred-etched aluminum pellets. The consistent Raman signal results from bare aluminum pellets, Au on aluminum foils, and Au on aluminum pellets show that 60 second etching and etching-stirred time produced the highest Raman intensity. Therefore, 60 seconds etching time for aluminum substrates was chosen as standard parameters of SERS effect in this research.

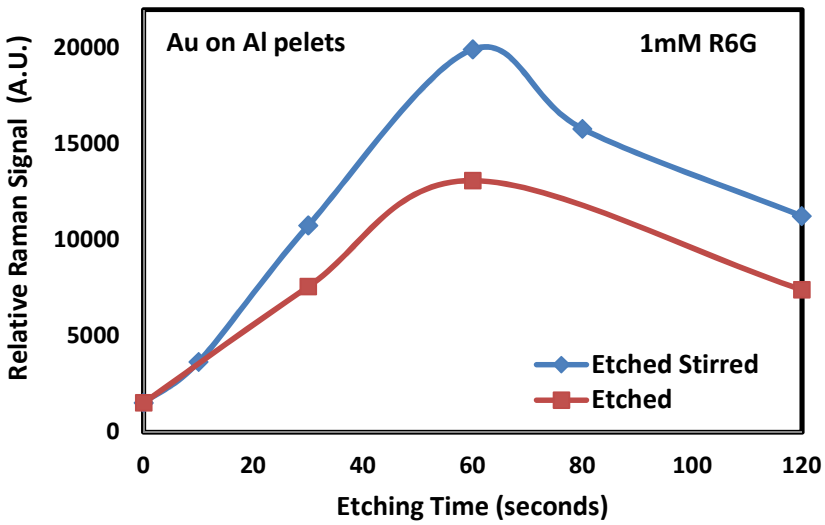

Figure 5.9 Raman signal with respect to Au on different etching time aluminum foils and pellets.

5.4. Au on Different Aluminum Substrates (Center)

In subchapter 4.3.1, Au was deposited on the 14 cm length of the three different aluminum foils (2 sets of 7 cm strips) inside the sputtering chamber. Raman spectra were obtained from Au nano metallic structures on three different types of aluminum foil (position -2.5 cm to 2.5 cm center area, figure 4.15) with 1mM R6G solution. The Raman intensities at 1363 cm^{-1} Raman line are about 1000 (Au on non etched aluminum foil), 5000 (Au on etched aluminum foil) and 8000 (Au on etched stirred aluminum foil) (figure 5.10). In subchapter 5.2, the Raman intensities at 1363 cm^{-1} Raman line from bare aluminum substrates are around 250. With an additional 20 nm Au on the aluminum surfaces, the Raman signal are enhanced by a factor of 4, a factor of 20, and factor of 40, respectively. 20 nm Au on etched stirred aluminum foil contains more Au nanoislands (AuNIs) and nano gaps than etched and non-etched aluminum foils. Localized surface plasmon resonances (LSPR) effect occurs because: 1. There are many nano-gaps between Au structures on the surface. 2. No oxidation occurs on the Au metallic surface. These results match with the morphologies of AFM and SEM images in chapter 4.

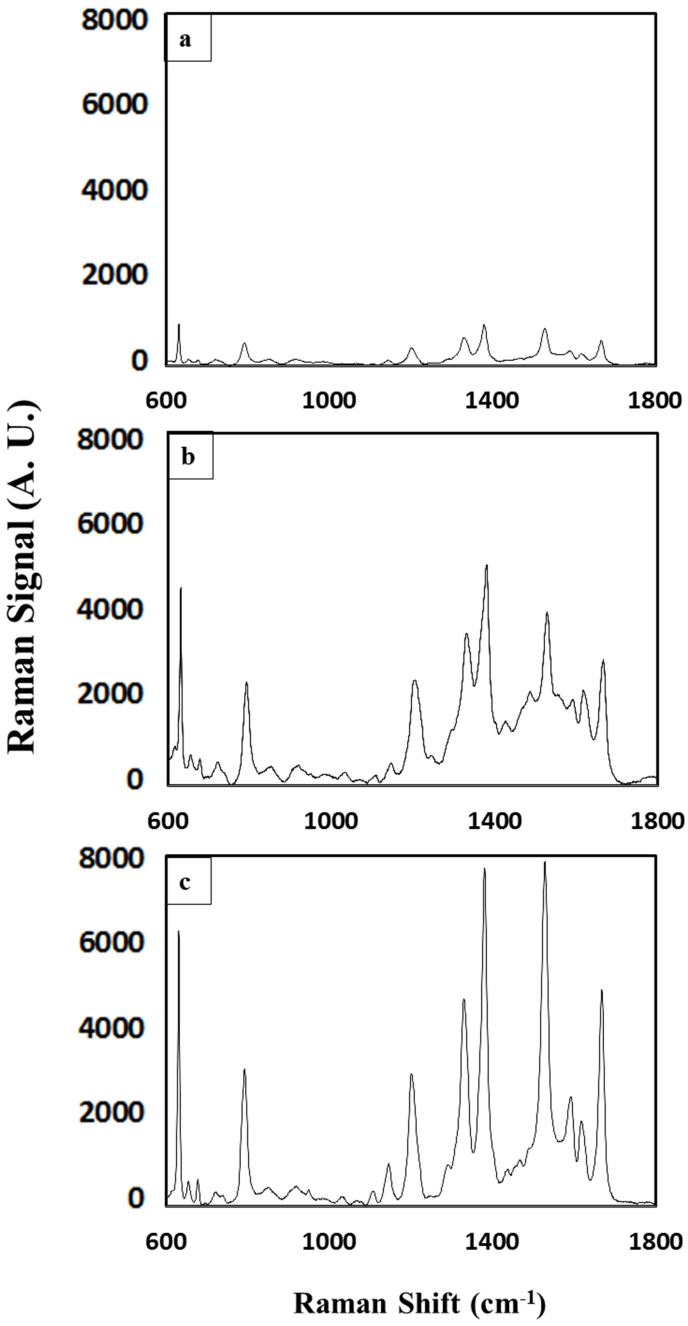

Figure 5.10 Raman spectra were obtained from the 20 nm Au nano metallic structure on three different types of aluminum foils in contact with 1 mM Rhodamine 6G solution (a) non-etched and (b) etched (c) etched-stirred.

5.5. Au on Different Aluminum Substrates (Edge)

In 4.3.1 subchapter, the SEM and AFM images show that there are more AuNIs around the edge of the etched-stirred aluminum foil than on the center of the foil. Two sets of Raman spectra were obtained in this subchapter: 1. sputtered Au on 10 cm length processed aluminum foil (2 sets of 5 cm strips). 2. sputtered Au on 14 cm length processed and non-processed aluminum foils (2 sets of 7 cm strips). The reason for two set of samples can also check the reproducibility of Raman signal with respect to the positions.

The first set of Raman spectra were obtained from Au nano metallic structures on 10 cm length etched stirred aluminum foil in contact with 1mM R6G solution. The Raman intensities at 1363 cm^{-1} Raman line are about 16000 around the edge of the sample and 4500 around the center (figure 5.11). The Raman signal is the smallest at $\pm$2.5 cm position and rises rapidly after passing $\pm$3.5 cm positions (Au target wide).

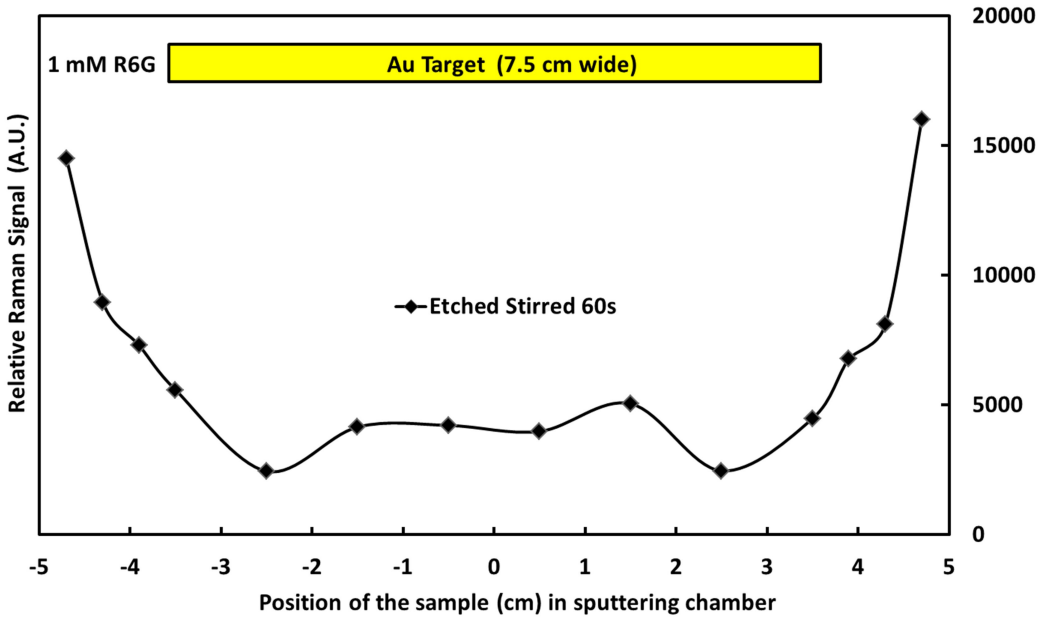

Figure 5.11 Raman spectra at 1363 cm^{-1}, obtained from Au nano metallic structures on 10 cm length etched stirred aluminum foils with 1mM R6G solution.

The second set of Raman spectra (figure 5.12) were obtained from Au nano metallic structures on 14 cm length non-etched, etched, and etched-stirred aluminum foils in contact with 1mM R6G solution. For Au on etched- stirred aluminum foil, Raman intensities at 1363 cm^{-1} Raman line are about 19000 at the edges of the sample and 7000 at the center. Next, for Au on etched aluminum foil, Raman intensities at 1363 cm-1 Raman line are about 14000 around the edge of the sample and 4000 around the center. Lastly, Raman intensities at 1363cm^{-1} Raman line are about 8000 around the edge of the sample and 1000 around the center for Au on non-etched aluminum foil. Same as figure 5.11, the Raman signal from Au on etched, and etched-stirred aluminum foils rises rapidly after passing ±3.5 cm positions (Au target wide) and falls down at the end of the both walls of chamber.

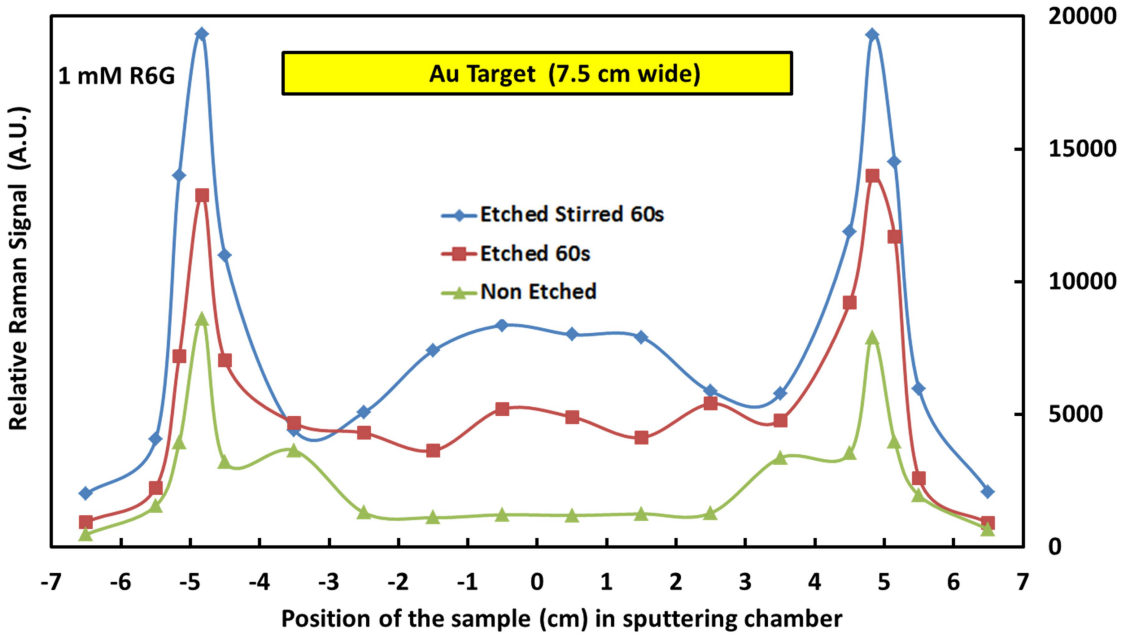

Figure 5.12 Raman spectra at 1363 cm^{-1}, obtained from Au nano metallic structures on 14 cm length etched stirred, etched, and non-etched aluminum foils with 1mM R6G solution.

For both sets of Raman spectra, the highest peaks are at 4 to 5 cm and -4 to -5 cm region, where the Au thickness is 14 nm with average 44.3 nm Au particle size (majority size range 30~60 nm). In addition, these results show that the Raman signal from Au on 60 seconds etched stirred aluminum foil is higher than Au on etched and non-etched aluminum foil. Several reasons to may explain the Raman signal peak at symmetric positions (4 cm to 5 cm and -4 cm to -5 cm) in this work.

5.6 Different deposition Au angles

Glancing angle deposition is a powerful technique which has been widely utilized for physical vapor deposition [78, 79]. Sputtered Au structures at certain angles normal to the substrate have been fabricated by tilting the angle of substrate during deposition [80]. Instead of tilting the angles of substrate, adjusting the angles of Au deposition during sputtering produced the same structure [81]. Moreover, the distribution of sputtered Au nanoparticles has been studied by using molecular dynamics simulations: For a spherical Au target, the sputtered Au is emitted isotopically [82]. For planar Au target, the majority of the sputtered Au is emitted toward the substrate [69, 83]. Au deposition angles shown on 5.13 can be divided into two components: 1. Directly from the Au target (region one). 2. Rebounded from the walls of the chamber (region two). The rebounded Au atoms deposit on the substrate at a certain angle. Therefore, the relationship between the Raman spectra and deposition angles was investigated.

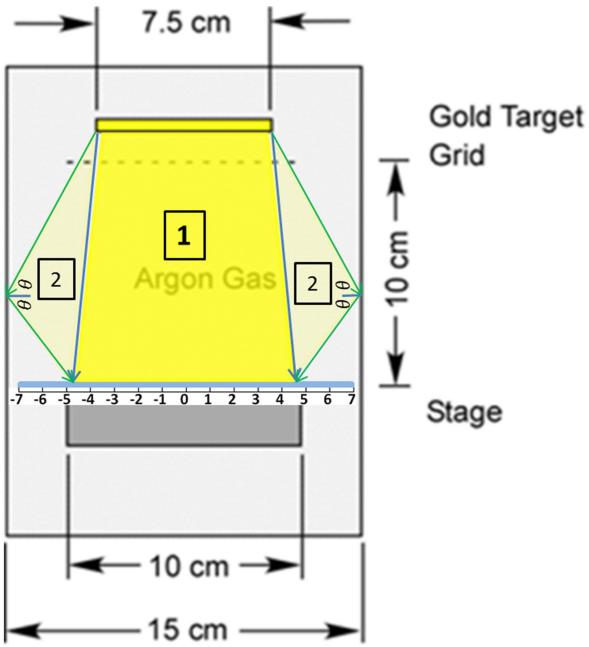

Figure 5.13 The schematic of possible Au depositions from Au target inside sputtering system. (1) Directly. (2) Indirectly.

Figure 5.14 shows the strength of the Raman spectra at different deposition angles. Raman spectra were obtained from Au nano metallic structures on aluminum pellets with 1mM R6G solution. The aluminum pellets were tilted at 0, 10, 25, and 55 deposition angles for the 20 nm Au depositions. The Raman intensity at the 1363 cm^{-1} Raman line shows that the 55 degree Au deposition generated the highest signal. The Raman signal increases while the deposition angles increases. The estimated reflected and emitted angles of Au atoms on the wall were around 52 degree ($90° - \tan^{-1}\frac{0.51}{0.65}$), which was computed by geometry math. This result suggests that the angles deposition is a factor in SERS.

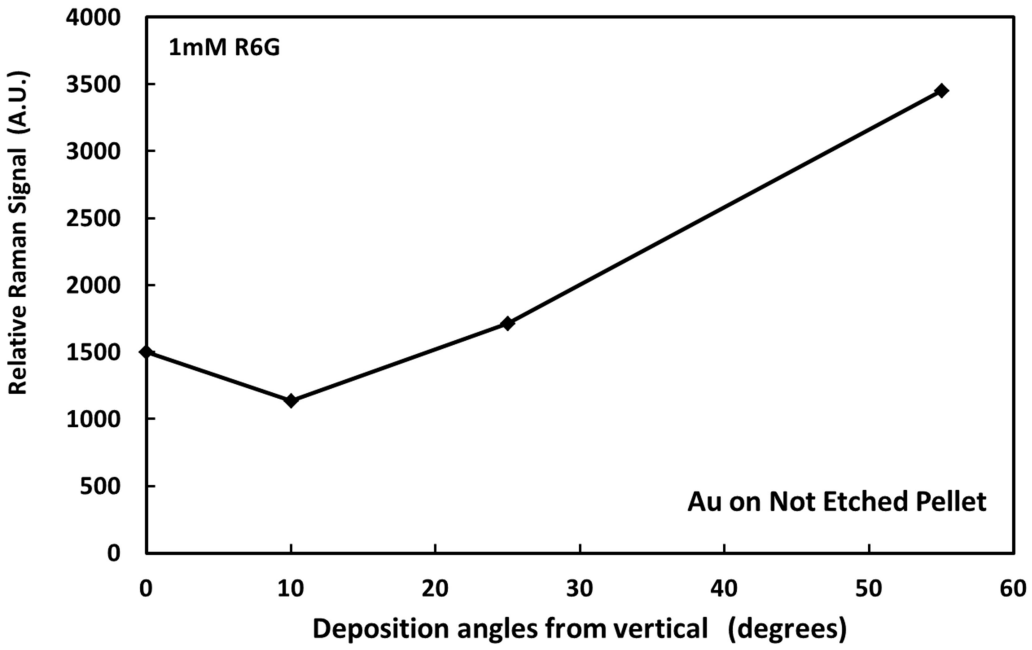

Figure 5.14 The Raman spectra with respect to different deposition angles (0, 10, 25, 55 degrees).

5.7. Reflection and Transmission (Center)

In the reflection view in figure 5.2(a), the Raman scattering signal was obtained from Au on etched-stirred aluminum foil though cover slip and the Rhodamine 6G. Raman signals were obtained at full range from 1nM to 1mM R6G (figure 5.15). Over a factor of one million change in R6G concentration, the Raman signal changed by a factor of 250. This is the evidence of SERS effect "hot spots" in the metallic surface that enhance the Raman signal enormously.

For the transmission view in figure 5.2(b), the Raman scattering signal was obtained from Au on epoxy substrate (back surface of the gold) through the cover slip and the epoxy substrate.

Raman signals were obtained at full range from 1nM to 1mM R6G (figure 5.16). Over a factor of one million changes in R6G concentration, the Raman signal changed by a factor of 10.

The difference between Raman signals in refection and transmission view may be caused by different topographies between Au on etched-stirred aluminum foil and Au on epoxy (figure 5.17). For the upper structure, when the Au is deposited on the etched-stirred aluminum foil, the top side of the Au has its own shape, and the bottom side of the gold follows the shape of the etched-stirred aluminum foil. For the bottom structure, the Au on the epoxy has a topography following the shape of the etched-stirred aluminum foil. Therefore, enhancement on upper structure may be stronger than on the bottom structure.

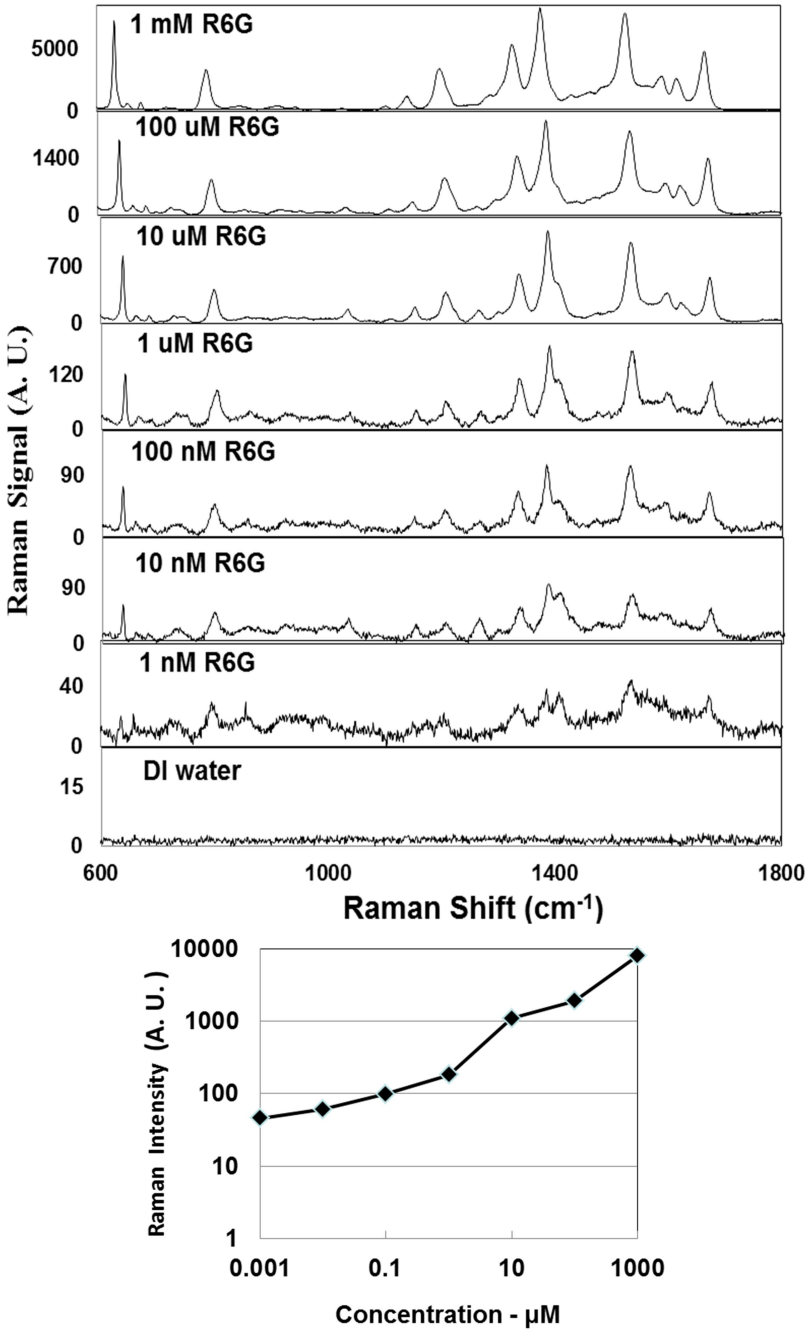

Figure 5.15 Raman Signals were obtained from 20 nm Au on etched-stirred aluminum foil in contact with various Rhodamine 6G solutions from 1 mM to 1 nM. Over a factor of one million changed in R6G concentration, the Raman signal changed by a factor of 250.

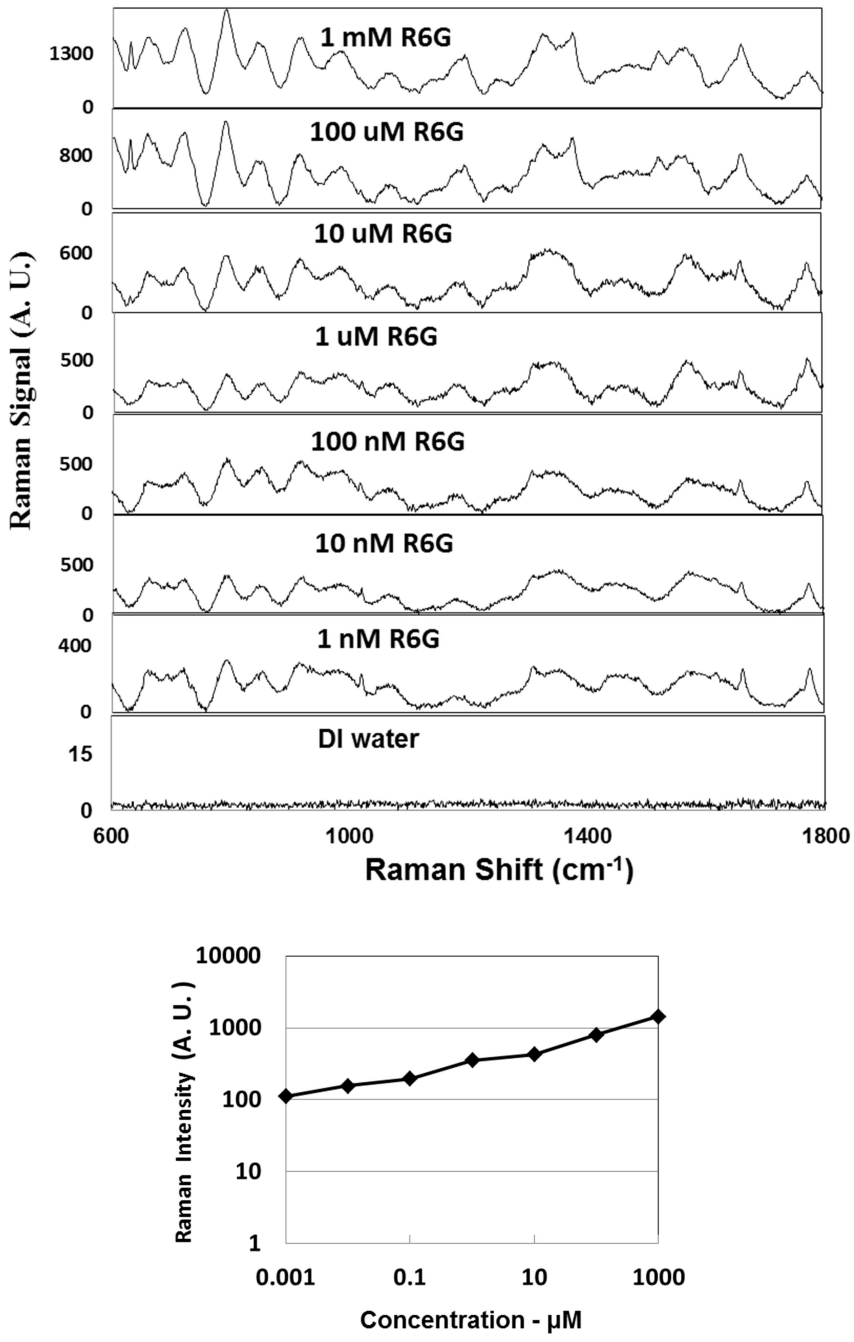

Figure 5.16 Raman Signals were obtained from Au on epoxy substrate in contact with various Rhodamine 6G solutions from 1 mM to 1 nM. Over a factor of one million changed in R6G concentration, the Raman signal changed by a factor of 10.

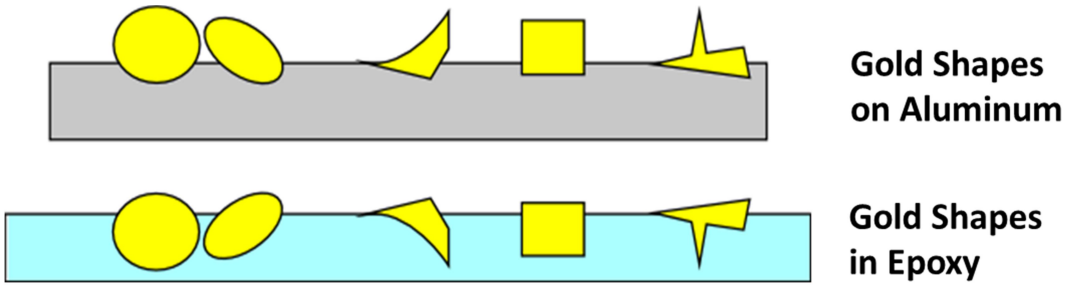

Figure 5.17 Different topographies between Au on etched-stirred aluminum foil and Au on epoxy.

5.8. Reflection and Transmission (Edge)

In the subchapter 5.5, Au was on the aluminum foils. Figure 5.12 shows the Raman signal strength in reflection across the chamber for three different types of aluminum foil with 1 mM Rhodamine 6G. The peak Raman signals are around both edges of the stage.

In this subchapter, the aluminum foils were etched totally. Figure 5.18 shows the Raman spectra in transmission from Au across the chamber on etched and etched stirred aluminum patterned epoxy with Rhodamine 6G. For Au on etched- stirred aluminum patterned epoxy, Raman intensities at 1363 cm^{-1} Raman line are about 2000 at the edges of the sample and 1500 at the center. For Au on etched aluminum patterned epoxy, Raman intensities are about 2500 at the edge of the sample and 1500 at the center. The highest peaks are at 4 to 5 cm and -4 to -5 cm, which is the same result as in reflection. The Raman spectra near the center are relatively uniform for both samples. Au on etched and on etched stirred aluminum patterned epoxy are similar.

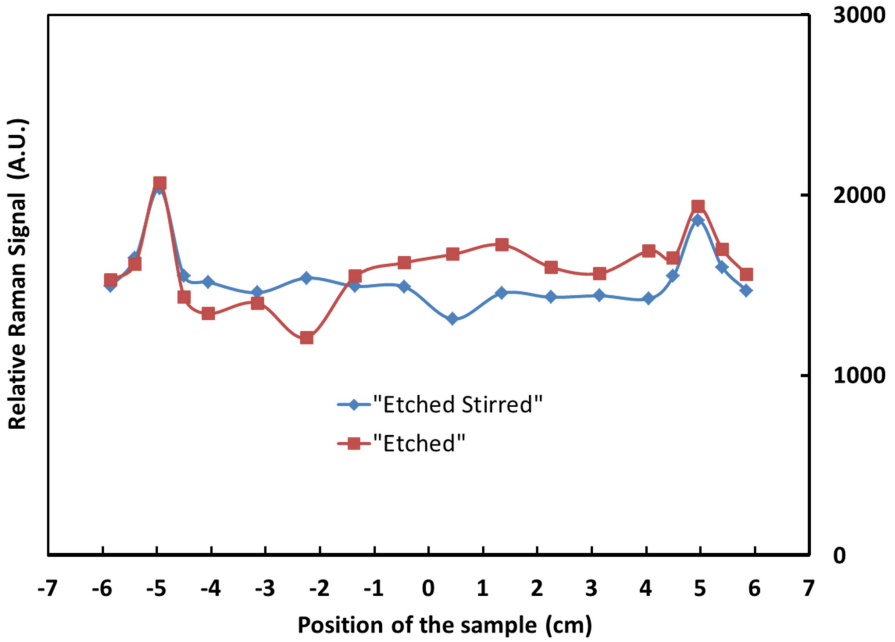

Figure 5.18 Raman spectra at 1363 cm-1 Raman line were obtained from Au nano metallic structures on 12 cm length etched and etched stirred aluminum patterned epoxy with 1mM R6G solution

5.9 Application for biological specimen: chicken cartilage and bone

Chicken cartilage and chicken bone were employed for the biological specimen measurement due to cost efficiency, availability, and easiness to acquire. The main information of the cartilage is tissue and synovial fluid which minimize and prevent the friction from the joint of hands, knees ,neck, and hip [84, 85]. A human with a damaged cartilage/joint disease will be diagnosed as osteoarthritis (OA), which can not be cured. Osteoarthritis may be caused by mechanical stress on a joint under two circumstances. 1. Uneven stress: Injury, obesity, and inherited factors [86, 87]. 2. Senescence: Degenerative cartilage with advancing age [87, 88].

Raman spectra of chicken cartilage and bones were obtained under a 50x microscope objective (figure 5.19) have similar Raman spectra [89, 90] to human cartilage and bone (Osteoarthritis) [90, 91].

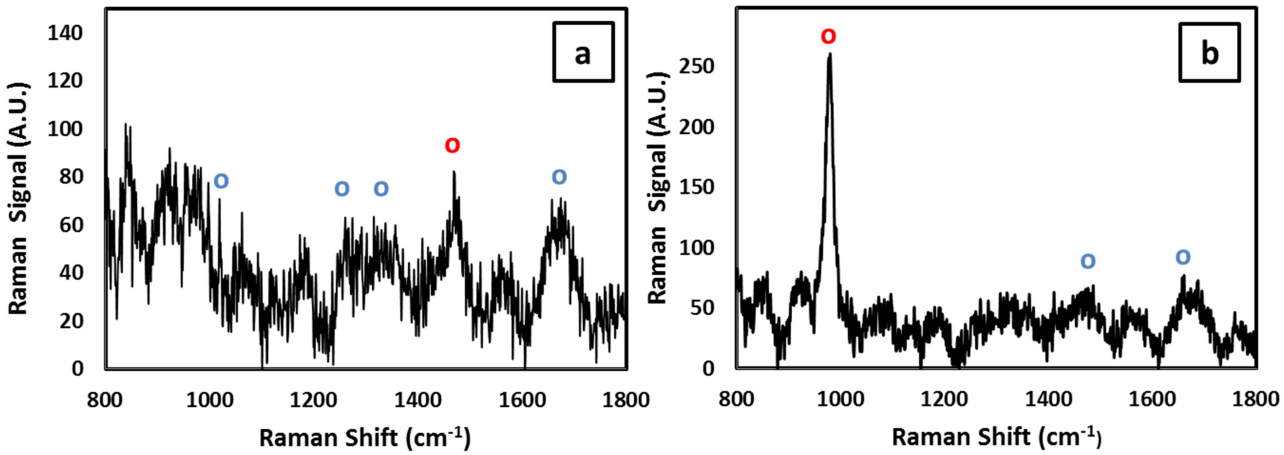

Figure 5.19 Raman spectrum of (a) chicken cartilage and (b) chicken bone under 50x microscope objective.

CHAPTER 6: SUMMARY, CONCLUSION AND FUTURE WORK

6.1. Summary and Conclusion

This research reports a new technique to obtain the nano-rough metallic surface for Surface Enhanced Raman Scattering (SERS) without costly lithographic steps. A series of fabrication methods of low cost, highly sensitive, reusable, and reproducible SERS substrates were characterized and demonstrated. Moreover, a series of Raman measurements from sputtered AuNIs on three different conditions of aluminum foil has been employed for two parts in this work. 1. SERS substrate in the conventional system (*in vitro* application), aluminum foil was acted as a base substrate. 2. SERS substrate in the transmission system (*in vivo* application), aluminum foils was acted as a nano patterned template on a transparent UV epoxy substrate.

These fabrication processes of the SERS system are described in figure 6.1. RMS measurements of AFM images were employed to analyze the different conditions of bare aluminum foils. The results demonstrated that the back side of the aluminum foil was rougher than the front side of the aluminum foil. Base on the results described above, the back side of etched aluminum foil was used as a substrate in this research. In addition, The RMS height variations increased over on small distance but decreased over large distance after Aluminum foils were etched (table 4.2). Etched–stirred aluminum foils were found to be rougher than etched aluminum substrate, and etched aluminum foils were rougher than non-etched aluminum foils (figure 4.7). The SEM and AFM images were taken in order to resolve the effects of nano-gaps and sizes between Au nanoislands (AuNIs) under different conditions of aluminum foils. The nano-gaps and sizes of AuNIs were smaller on etched-stirred aluminum

foils than on etched aluminum foils, and were smaller on etched aluminum foils than on non etched aluminum foils. Table 4.6 shows the RMS from sputtered Au on etched-stirred was rougher than etched aluminum foil, and etched was rougher than non-etched aluminum foil. The Au sputtering procedure made the surface rougher from 12nm (the initial roughness of non etched aluminum foil) to 34nm (Au on etched stirred aluminum foil).

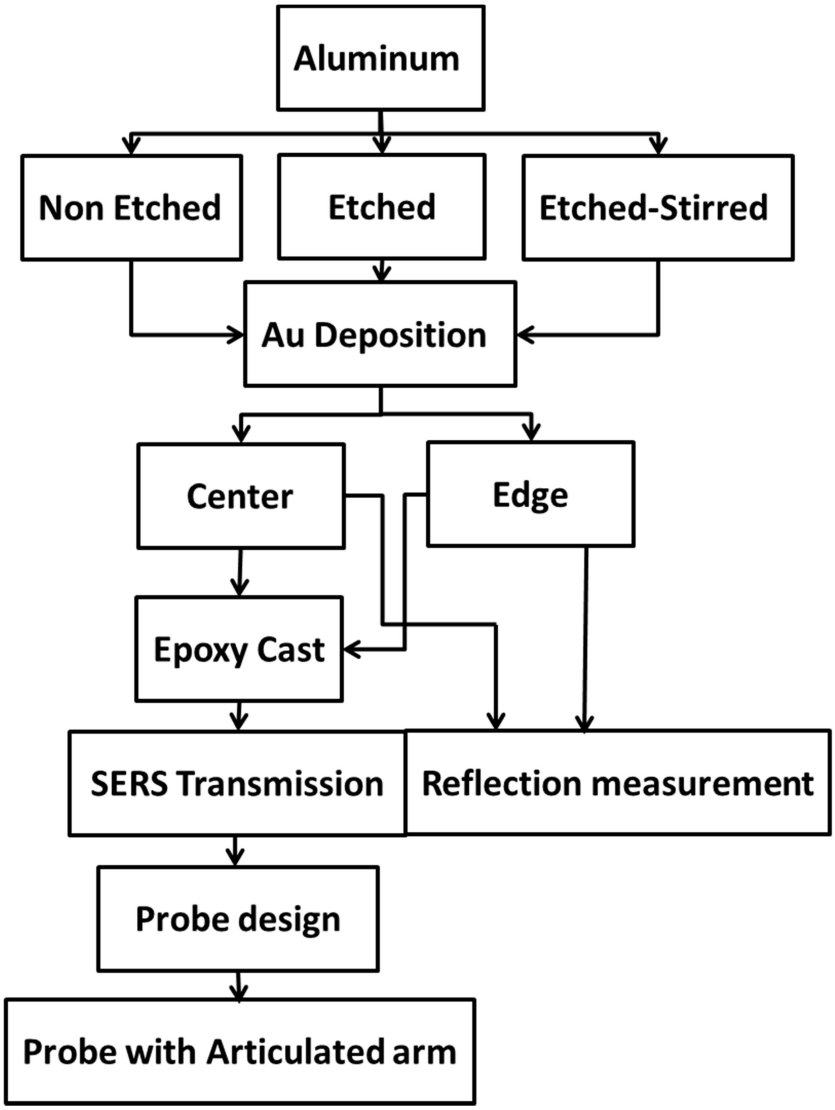

Figure 6.1 The fabrication process of the SERS system.

The Au particle sizes, thicknesses, and structures on the aluminum substrate were assumed to be the same as Au structure on the wafer, because the wafer and aluminum foils substrate were processed simultaneously, so the Au deposition amount at each position should be the same. Au depositions (-7 to 7 cm) on the wafer across the chamber showed the Au thicknesses reducing toward the edge of the chamber. The comparison of Au thicknesses on the wafer with respect to the positions is shown on table 4.4.

The Raman signal results matched the topography results on chapter 4. For the reflection view, the Raman signals from the back side of bare aluminum foils were higher than the front side of bare aluminum foil. Moreover, the Raman signals from back side of aluminum foils, aluminum pellets and shop grade aluminums were all more or less the same. Raman signals from the etched aluminum substrates were higher than non-etched aluminum substrate. We believe that etching process amplifies the Raman effect, because it cleans the surface of the aluminum and makes the surface rougher. The R6G Raman signal from Au on etched- stirred aluminum foil was higher than etched and non-etched aluminum foil. Moreover, a series of Raman measurements (- 7 cm to 7 cm) (figure 5.12 and 5.18) had been employed for two parts in this work. 1. SERS substrate in the conventional system (in vitro application). 2. SERS substrate in the transmission system (in vivo application). The highest Raman signal (reflection and transmission view) were generated around position 4~5 and -4~-5 cm (figure 5.12 and 5.18). Those highest Raman signal were caused by the deposition of angles, deposition of thicknesses, and pre etched times for aluminum substrates.

With 20 nm sputtered Au on etched stirred aluminum foils increases the Raman signal by a factor of 40. A series of measurements in reflection from 1 nM to 1mM R6G is shown in figure 5.15. Over a factor of one million change in R6G concentration, the Raman signal changed by a

factor of 250. A series of measurements in transmission from 1 nM to 1mM R6G is shown in figure 5.16. Over a factor of one million change in R6G concentration, the Raman signal changed by a factor of 10. This difference may result from different topographies between Au on etched-stirred aluminum foil (reflection view) and Au on epoxy, which also was discussed in figure 5.17. Moreover, the first step of biological Raman spectrum measurement for chicken cartilage and bones was demonstrated.

6.2. Future Work

The future work will be divided into four parts. 1. Develop other cost efficient SERS substrates. 2. Couple the probe head and articulated arm system. 3. Further performance for biological specimens under probe head and articulated arm system. 4. Reduce the diameter of the probe head.

The fabrication steps of this SERS substrate can be transferred to other low cost deposition devices such as thermal evaporator, chemical vapor deposition, and electroplating. The SERS effect can be maximized by manipulating parameters such as different sputtering angles, sputtering positions, thicknesses, and pre-etching times. The challenges of developing other low cost SERS substrates are collecting higher signal intensity, obtaining more sensitivity.

The probe head is an important part in our SERS measurement system. The first design of probe head (figure 6.2) has two parts: a threaded housing, and an aluminum head. The threaded housing contains a 2 mm internal diameter probe with a 5.2 mm length gradient-index lens

(GRIN) 2 mm in diameter, to which a transparent SERS substrate is attached. The aluminum head contains a small positive lens. The threaded housing accommodates the GRIN lens (π/2 pitch with 5.2 mm length) and locks the aluminum head. The principle of GRIN lens is continuously changing refractive index. The GRIN lens focuses the intermediate image formed by the positive lens onto the metallic substrate. The GRIN lens was attached to probe by first A-B epoxy. After the first A-B epoxy cured, the transparent SERS substrate was attached to the end of the gradient-index (GRIN) lens by second A-B epoxy which has similar index reflection as glass. The laser beam was focused on SERS substrate by adjusting the nut and thread. The challenges of developing the probe head are listed: A. Minimizing the diameter of probe head. B. Minimizing the thickness of epoxy between SERS substrate and GRIN. C. Permanently attach the SERS substrate to the GRIN lens. D. Focus the laser light on the SERS substrate. The SERS probe head finally is coupled to an articulated arm and performs specimen measurements [71].

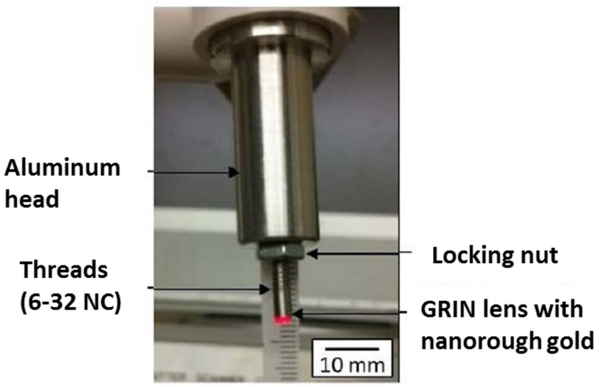

Figure 6.2 The photograph of the probe with light emitting through the rough gold surface. [71, 92]. (COPYRIGHT)

The first evolution draft of the probe head had been demonstrated in this work. The diameters of the probe had been reduced from 2 mm probe size to 0.5 mm needle size. The evolution (figure 6.2) starts at assembling SERS substrate on 2 mm in diameter GRIN lens → on 1mm GRIN lens → on fiber with 1 mm diameter needle → on fiber with 0.5 mm needle. A 5~7 cm length of signal mode fiber (core 8~10.5 μm, cladding 125 μm and jacket 400 μm in diameter) was employed in this work [93]. The fabrication of fiber inside the needle was similar as the GRIN lens inside the probe. A 6~8cm length of fiber was inserted and epoxied inside the needles (1 or 0.5 mm diameter). Then, the SERS substrate was epoxied on the front end of the fiber. Moreover, the thickness of epoxy had been reduced from 380 to 30 μm by evenly distributed pressure.

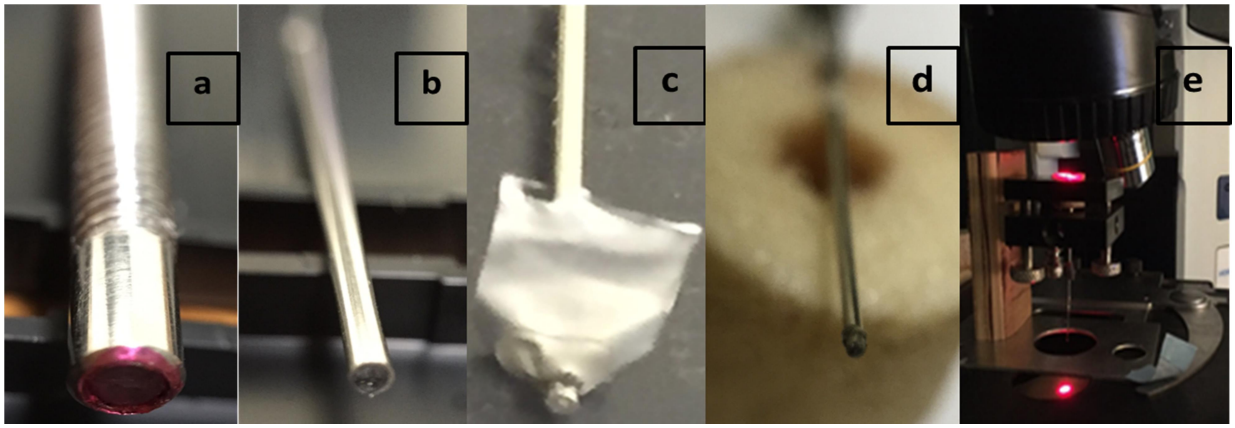

Figure 6.3 The diameter size evolution of the probe head design. (a) A 2 mm GRIN lens. (b) A 1 mm GRIN lens. (c) A fiber in 1 mm needle. (d) A fiber in 0.5 mm needle (e) The laser output from 0.5 mm needle.

Commercial fiber optic Raman spectrometer system has been developed. The probe head can be divided into two parts. 1. Optical collection through lenses at the tip of a probe head. 2. Two fibers for photon transmission following by the optical lenses. Typically, an emitted laser

from the excitation fiber is focused on the specimen by a small positive lens, and the scattering signal is collected by a collection fiber through the same or other small positive lens. Both ends of excitation and collection fibers are coupled to spectrometer [94, 95]. Unfortunately, two disadvantages occur: 1. this method generates strong background signal of glass fiber and blocks the Raman signal due to the long length of the fiber. 2. Two fiber and optical lens make the volume probe head invasive [94, 95]. However, with the SERS substrate on the tip of 5~7 cm one single fiber inside 0.5 mm needle in this work, it not only overcomes the two problems but also enhances the Raman signal.

Final goal is to couple a 0.5 mm remote Raman probe head and a high transmission acritical arm system for clinical diagnosis to obtain spectra of cartilage and bone in clinical environment. Eventually, this system can demonstrate the ability to obtain signals from a patient simply sitting or lying near the SERS spectrometer in a clinical environment.

REFERENCE

[1] B. Stewart and C. P. Wild, "World cancer report 2014," *World,* 2015.

[2] R. L. Siegel, K. D. Miller, and A. Jemal, "Cancer statistics, 2015," *CA: a cancer journal for clinicians,* vol. 65, pp. 5-29, 2015.

[3] R. Doll and R. Peto, "The causes of cancer: quantitative estimates of avoidable risks of cancer in the United States today," *Journal of the National Cancer Institute,* vol. 66, pp. 1192-1308, 1981.

[4] A. Jemal, R. Siegel, E. Ward, Y. Hao, J. Xu, T. Murray*, et al.*, "Cancer statistics, 2008," *CA: a cancer journal for clinicians,* vol. 58, pp. 71-96, 2008.

[5] C. A. Burtis, E. R. Ashwood, and D. E. Bruns, *Tietz textbook of clinical chemistry and molecular diagnostics*: Elsevier Health Sciences, 2012.

[6] M. A. Hamburg and F. S. Collins, "The path to personalized medicine," *New England Journal of Medicine,* vol. 363, pp. 301-304, 2010.

[7] R. Aebersold and M. Mann, "Mass spectrometry-based proteomics," *Nature,* vol. 422, pp. 198-207, 2003.

[8] C. Lock, G. Hermans, R. Pedotti, A. Brendolan, E. Schadt, H. Garren*, et al.*, "Gene-microarray analysis of multiple sclerosis lesions yields new targets validated in autoimmune encephalomyelitis," *Nature medicine,* vol. 8, pp. 500-508, 2002.

[9] K. Schwochau, "Uses of technetium - 99," *Technetium: Chemistry and Radiopharmaceutical Applications,* pp. 87-93.

[10] R. Weissleder and M. J. Pittet, "Imaging in the era of molecular oncology," *Nature,* vol. 452, pp. 580-589, 2008.

[11] M. Gauberti, A. Montagne, A. Quenault, and D. Vivien, "Molecular magnetic resonance imaging of brain–immune interactions," *Front Cell Neurosci,* vol. 8, pp. 1-20, 2014.

[12] J. Hsieh, "Computed tomography: principles, design, artifacts, and recent advances," 2009.

[13] C. J. Pavlin, K. Harasiewicz, M. D. Sherar, and F. S. Foster, "Clinical use of ultrasound biomicroscopy," *Ophthalmology,* vol. 98, pp. 287-295, 1991.

[14] E. Tulving, S. Kapur, F. Craik, M. Moscovitch, and S. Houle, "Hemispheric encoding/retrieval asymmetry in episodic memory: positron emission tomography findings," *Proceedings of the National Academy of Sciences,* vol. 91, pp. 2016-2020, 1994.

[15] K.-H. Krause, S. H. Dresel, J. Krause, H. F. Kung, and K. Tatsch, "Increased striatal dopamine transporter in adult patients with attention deficit hyperactivity disorder: effects of methylphenidate as measured by single photon emission computed tomography," *Neuroscience letters,* vol. 285, pp. 107-110, 2000.

[16] V. Ntziachristos, C. Bremer, and R. Weissleder, "Fluorescence imaging with near-infrared light: new technological advances that enable in vivo molecular imaging," *European radiology,* vol. 13, pp. 195-208, 2003.

[17] A. Rehemtulla, L. D. Stegman, S. J. Cardozo, S. Gupta, D. E. Hall, C. H. Contag*, et al.*, "Rapid and quantitative assessment of cancer treatment response using in vivo bioluminescence imaging," *Neoplasia,* vol. 2, pp. 491-495, 2000.

[18] R. K. Jain, L. L. Munn, and D. Fukumura, "Dissecting tumour pathophysiology using intravital microscopy," *Nature Reviews Cancer,* vol. 2, pp. 266-276, 2002.

[19] S. Prevrhal, J. C. Fox, J. A. Shepherd, and H. K. Genant, "Accuracy of CT-based thickness measurement of thin structures: modeling of limited spatial resolution in all three dimensions," *Medical physics,* vol. 30, pp. 1-8, 2003.

[20] P. K. Saha and F. W. Wehrli, "Measurement of trabecular bone thickness in the limited resolution regime of in vivo MRI by fuzzy distance transform," *Medical Imaging, IEEE Transactions on,* vol. 23, pp. 53-62, 2004.

[21] C. V. Raman and K. S. Krishnan, "A new type of secondary radiation," *Nature,* vol. 121, pp. 501-502, 1928.

[22] E. Le Ru and P. Etchegoin, *Principles of Surface-Enhanced Raman Spectroscopy: and related plasmonic effects*: Elsevier, 2008.

[23] C. Kittel and D. F. Holcomb, "Introduction to solid state physics," *American Journal of Physics,* vol. 35, pp. 547-548, 1967.

[24] G. Elert, "Electromagnetic Spectrum," *The Physics Hypertextbook,* 2013.

[25] A. D. Strickland and C. A. Batt, "Detection of carbendazim by surface-enhanced Raman scattering using cyclodextrin inclusion complexes on gold nanorods," *Analytical chemistry,* vol. 81, pp. 2895-2903, 2009.

[26] M. Pelletier, "Quantitative analysis using Raman spectrometry," *Applied spectroscopy,* vol. 57, pp. 20A-20A, 2003.

[27] R. Mukhopadhyay, "Raman flexes its muscles," *Analytical Chemistry,* vol. 79, pp. 3265-3270, 2007.

[28] M. Sharma, E. Marple, J. Reichenberg, and J. W. Tunnell, "Design and characterization of a novel multimodal fiber-optic probe and spectroscopy system for skin cancer applications," *Review of Scientific Instruments,* vol. 85, p. 083101, 2014.

[29] A. Weber, *Raman spectroscopy of gases and liquids* vol. 11: Springer Science & Business Media, 2012.

[30] J. Kiefer, T. Seeger, S. Steuer, S. Schorsch, M. Weikl, and A. Leipertz, "Design and characterization of a Raman-scattering-based sensor system for temporally resolved gas analysis and its application in a gas turbine power plant," *Measurement Science and Technology,* vol. 19, p. 085408, 2008.

[31] M. Fleischmann, P. J. Hendra, and A. McQuillan, "Raman spectra of pyridine adsorbed at a silver electrode," *Chemical Physics Letters,* vol. 26, pp. 163-166, 1974.

[32] H. Knobloch, H. Brunner, A. Leitner, F. Aussenegg, and W. Knoll, "Probing the evanescent field of propagating plasmon surface polaritons by fluorescence and Raman spectroscopies," *The Journal of chemical physics,* vol. 98, pp. 10093-10095, 1993.

[33] K. A. Willets and R. P. Van Duyne, "Localized surface plasmon resonance spectroscopy and sensing," *Annu. Rev. Phys. Chem.,* vol. 58, pp. 267-297, 2007.

[34] A. J. Haes, C. L. Haynes, A. D. McFarland, G. C. Schatz, R. P. Van Duyne, and S. Zou, "Plasmonic materials for surface-enhanced sensing and spectroscopy," *Mrs Bulletin,* vol. 30, pp. 368-375, 2005.

[35] K. L. Kelly, E. Coronado, L. L. Zhao, and G. C. Schatz, "The optical properties of metal nanoparticles: the influence of size, shape, and dielectric environment," *The Journal of Physical Chemistry B,* vol. 107, pp. 668-677, 2003.

[36] G. H. Chan, J. Zhao, G. C. Schatz, and R. P. V. Duyne, "Localized surface plasmon resonance spectroscopy of triangular aluminum nanoparticles," *The Journal of Physical Chemistry C,* vol. 112, pp. 13958-13963, 2008.

[37] L. J. Sherry, S.-H. Chang, G. C. Schatz, R. P. Van Duyne, B. J. Wiley, and Y. Xia, "Localized surface plasmon resonance spectroscopy of single silver nanocubes," *Nano letters,* vol. 5, pp. 2034-2038, 2005.

[38] H. H. Wang, C. Y. Liu, S. B. Wu, N. W. Liu, C. Y. Peng, T. H. Chan*, et al.*, "Highly raman-enhancing substrates based on silver nanoparticle arrays with tunable sub-10 nm gaps," *Advanced Materials,* vol. 18, pp. 491-495, 2006.

[39] B. Sharma, R. R. Frontiera, A.-I. Henry, E. Ringe, and R. P. Van Duyne, "SERS: materials, applications, and the future," *Materials today,* vol. 15, pp. 16-25, 2012.

[40] S. Lin, W. Zhu, Y. Jin, and K. B. Crozier, "Surface-enhanced Raman scattering with Ag nanoparticles optically trapped by a photonic crystal cavity," *Nano letters,* vol. 13, pp. 559-563, 2013.

[41] E. H. Witlicki, C. Johnsen, S. W. Hansen, D. W. Silverstein, V. J. Bottomley, J. O. Jeppesen*, et al.*, "Molecular Logic Gates Using Surface-Enhanced Raman-Scattered Light," *Journal of the American Chemical Society,* vol. 133, pp. 7288-7291, 2011.

[42] J. Mock, M. Barbic, D. Smith, D. Schultz, and S. Schultz, "Shape effects in plasmon resonance of individual colloidal silver nanoparticles," *The Journal of Chemical Physics,* vol. 116, pp. 6755-6759, 2002.

[43] M. Moskovits, "Surface-enhanced spectroscopy," *Reviews of modern physics,* vol. 57, p. 783, 1985.

[44] X. Li, M. Cao, H. Zhang, L. Zhou, S. Cheng, J.-L. Yao*, et al.*, "Surface-enhanced Raman scattering-active substrates of electrospun polyvinyl alcohol/gold–silver nanofibers," *Journal of colloid and interface science,* vol. 382, pp. 28-35, 2012.

[45] X. Hu, W. Cheng, T. Wang, Y. Wang, E. Wang, and S. Dong, "Fabrication, characterization, and application in SERS of self-assembled polyelectrolyte-gold nanorod multilayered films," *The Journal of Physical Chemistry B,* vol. 109, pp. 19385-19389, 2005.

[46] W. Wu, M. Hu, F. S. Ou, Z. Li, and R. S. Williams, "Cones fabricated by 3D nanoimprint lithography for highly sensitive surface enhanced Raman spectroscopy," *Nanotechnology,* vol. 21, p. 255502, 2010.

[47] I. Baranov, P. Håkansson, S. Kirillov, J. Kopniczky, A. Novikov, V. Obnorskii*, et al.*, "Desorption of nanoclusters (2–40 nm) from nanodispersed metal and semiconductor layers by swift heavy ions," *Nuclear Instruments and Methods in Physics Research Section B: Beam Interactions with Materials and Atoms,* vol. 193, pp. 798-803, 2002.

[48] Y. Li and G. Shi, "Electrochemical growth of two-dimensional gold nanostructures on a thin polypyrrole film modified ITO electrode," *The Journal of Physical Chemistry B,* vol. 109, pp. 23787-23793, 2005.

[49] I. Weppelman, P. Post, C. Heerkens, C. Hagen, and J. Hoogenboom, "Fabrication of narrow-gap nanostructures using electron-beam induced deposition etch masks," *Microelectronic Engineering,* vol. 153, pp. 77-82, 2016.

[50] B. Satpati, D. Goswami, U. Vaishnav, T. Som, B. Dev, and P. Satyam, "Energy spike induced effects in MeV ion-irradiated nanoislands," *Nuclear Instruments and Methods in Physics Research Section B: Beam Interactions with Materials and Atoms,* vol. 212, pp. 157-163, 2003.

[51] P. Matousek and M. Morris, *Emerging Raman applications and techniques in biomedical and pharmaceutical fields*: Springer Science & Business Media, 2010.

[52] M. E. Wieser and T. B. Coplen, "Atomic weights of the elements 2009 (IUPAC Technical Report)," *Pure and Applied Chemistry,* vol. 83, pp. 359-396, 2010.

[53] J. W. Tully, "Aluminum liftoff masking process and product," ed: Google Patents, 1989.

[54] D. Westberg, O. Paul, G. I. Andersson, and H. Baltes, "Surface micromachining by sacrificial aluminium etching," *Journal of Micromechanics and Microengineering,* vol. 6, p. 376, 1996.

[55] R. De Oliveira, D. Albuquerque, F. Leite, F. Yamaji, and T. Cruz, *Measurement of the nanoscale roughness by atomic force microscopy: basic principles and applications*: INTECH Open Access Publisher, 2012.

[56] E. P. DeGarmo, J. Black, R. A. Kohser, and B. E. Klamecki, "Materials and process in manufacturing," *Jolm Wiley and Sons, USA,* p. 974, 2003.

[57] M. J. De Boer, J. Gardeniers, H. V. Jansen, E. Smulders, M.-J. Gilde, G. Roelofs*, et al.*, "Guidelines for etching silicon MEMS structures using fluorine high-density plasmas at cryogenic temperatures," *Microelectromechanical Systems, Journal of,* vol. 11, pp. 385-401, 2002.

[58] K. R. Williams and R. S. Muller, "Etch rates for micromachining processing," *Microelectromechanical Systems, Journal of,* vol. 5, pp. 256-269, 1996.

[59] K. R. Williams, K. Gupta, and M. Wasilik, "Etch rates for micromachining processing-Part II," *Microelectromechanical Systems, Journal of,* vol. 12, pp. 761-778, 2003.

[60] J. Kim, K.-N. Kang, A. Sarkar, P. Malempati, D. Hah, T. Daniels-Race*, et al.*, "Nanorough gold for enhanced Raman scattering," *Journal of Vacuum Science & Technology B,* vol. 31, p. 06FE02, 2013.

[61] A. Seidell, W. F. Linke, A. W. Francis, and R. G. Bates, *Solubilities of inorganic and organic compounds: supplement to the third edition containing data published during the years 1939-1949 inclusive: a compilation of quantitative solubility data from the periodical literature*: American Chemical Society, 1952.

[62] T. J. Bruno and P. D. Svoronos, *CRC handbook of basic tables for chemical analysis*: CRC press, 2003.

[63] L. Soler, J. Macanás, M. Munoz, and J. Casado, "Hydrogen generation from aluminum in a non-consumable potassium hydroxide solution," in *Proceedings International Hydrogen Energy Congress and Exhibition IHEC*, 2005, pp. 13-15.

[64] J. C. Rich, *The materials and methods of sculpture*: Courier Corporation, 1988.

[65] S.-U. Fang, C.-L. Hsu, T.-C. Hsu, M.-Y. Juang, and Y.-C. Liu, "Surface roughness-correlated SERS effect on Au island-deposited substrate," *Journal of Electroanalytical Chemistry,* vol. 741, pp. 127-133, 2015.

[66] M. T. Yaseen, M. Chen, and Y.-C. Chang, "Partially embedded gold nanoislands in a glass substrate for SERS applications," *RSC Adv.,* vol. 4, pp. 55247-55251, 2014.

[67] Z. Kang, J. Chen, S.-Y. Wu, K. Chen, S.-K. Kong, K.-T. Yong*, et al.*, "Trapping and assembling of particles and live cells on large-scale random gold nano-island substrates," *Scientific reports,* vol. 5, 2015.

[68] P. S. McLeod, "Planar magnetron sputtering method and apparatus," ed: Google Patents, 1976.

[69] S. Zimmermann and H. M. Urbassek, "Sputtering of nanoparticles: Molecular dynamics study of Au impact on 20nm sized Au nanoparticles," *International Journal of Mass Spectrometry,* vol. 272, pp. 91-97, 2008.

[70] P. Slepička, Z. Kolská, J. Náhlík, V. Hnatowicz, and V. Švorčík, "Properties of Au nanolayers on polyethyleneterephthalate and polytetrafluoroethylene," *Surface and Interface Analysis,* vol. 41, pp. 741-745, 2009.

[71] J. Kim, "Clinical Probe Utilizing Surface-Enhanced Raman Scattering (SERS) for In-Situ Molecular Imaging Applications," Louisiana State University, 2015.

[72] W. Tan, K. Wang, X. He, X. J. Zhao, T. Drake, L. Wang*, et al.*, "Bionanotechnology based on silica nanoparticles," *Medicinal research reviews,* vol. 24, pp. 621-638, 2004.

[73] J. Widengren, J. Dapprich, and R. Rigler, "Fast interactions between Rh6G and dGTP in water studied by fluorescence correlation spectroscopy," *Chemical Physics,* vol. 216, pp. 417-426, 1997.

[74] C. J. Moon, J. H. Shin, D. W. Kim, S. J. Kee, S. H. Kim, M. G. Shin*, et al.*, "Species-specific differences in Rhodamine 6G accumulation of Candida isolates detected by flow cytometric analysis," *The Korean journal of laboratory medicine,* vol. 29, pp. 127-134, 2009.

[75] C. Eggeling, A. Volkmer, and C. A. Seidel, "Molecular Photobleaching Kinetics of Rhodamine 6G by One-and Two-Photon Induced Confocal Fluorescence Microscopy," *ChemPhysChem,* vol. 6, pp. 791-804, 2005.

[76] A. M. Michaels, M. Nirmal, and L. Brus, "Surface enhanced Raman spectroscopy of individual rhodamine 6G molecules on large Ag nanocrystals," *Journal of the American Chemical Society,* vol. 121, pp. 9932-9939, 1999.

[77] P. Hildebrandt and M. Stockburger, "Surface-enhanced resonance Raman spectroscopy of Rhodamine 6G adsorbed on colloidal silver," *The Journal of Physical Chemistry,* vol. 88, pp. 5935-5944, 1984.

[78] J. Wang, H. Huang, S. Kesapragada, and D. Gall, "Growth of Y-shaped nanorods through physical vapor deposition," *Nano letters,* vol. 5, pp. 2505-2508, 2005.

[79] M. M. Hawkeye and M. J. Brett, "Glancing angle deposition: fabrication, properties, and applications of micro-and nanostructured thin films," *Journal of Vacuum Science & Technology A,* vol. 25, pp. 1317-1335, 2007.

[80] J. M. García-Martín, R. Alvarez, P. Romero-Gómez, A. Cebollada, and A. Palmero, "Tilt angle control of nanocolumns grown by glancing angle sputtering at variable argon pressures," *Applied Physics Letters,* vol. 97, p. 173103, 2010.

[81] H. Tsuge and S. Esho, "Angular distribution of sputtered atoms from polycrystalline metal targets," *Journal of Applied Physics,* vol. 52, pp. 4391-4395, 1981.

[82] R. Kissel and H. M. Urbassek, "Sputtering from spherical Au clusters by energetic atom bombardment," *Nuclear Instruments and Methods in Physics Research Section B: Beam Interactions with Materials and Atoms,* vol. 180, pp. 293-298, 6// 2001.

[83] G. Falcone, "Sputtering yield including anisotropic effects," *Physics Letters A,* vol. 129, pp. 188-190, 1988.

[84] C. E. Anderson, "The structure and function of cartilage," *J Bone Joint Surg Am,* vol. 44, pp. 777-786, 1962.

[85] P. T. Paradowski, "Osteoarthritis of the knee: assessing the disease," *Health Care: Current Reviews,* vol. 2015, 2014.

[86] F. Berenbaum, "Osteoarthritis as an inflammatory disease (osteoarthritis is not osteoarthrosis!)," *Osteoarthritis and Cartilage,* vol. 21, pp. 16-21, 2013.

[87] S. Glyn-Jones, A. Palmer, R. Agricola, A. Price, T. Vincent, H. Weinans*, et al.*, "Osteoarthritis," *The Lancet,* vol. 386, pp. 376-387, 2015.

[88] Y. Zhang and J. M. Jordan, "Epidemiology of osteoarthritis," *Clinics in geriatric medicine,* vol. 26, pp. 355-369, 2010.

[89] A. Carden, R. Rajachar, M. D. Morris, and D. Kohn, "Ultrastructural changes accompanying the mechanical deformation of bone tissue: a Raman imaging study," *Calcified Tissue International,* vol. 72, pp. 166-175, 2003.

[90] M. Orkoula, M. Vardaki, P. Megas, S. Panteliou, C. Kontoyannis, and D. Papachristou, "Raman spectroscopy of articular cartilage and subchondral bone on osteoarthritic human femoral heads," *Πρακτικά 15ου Πανελλήνιου Φαρμακευτικού Συνεδρίου,* 2012.

[91] Y. Takahashi, N. Sugano, M. Takao, T. Sakai, T. Nishii, and G. Pezzotti, "Raman spectroscopy investigation of load-assisted microstructural alterations in human knee cartilage: Preliminary study into diagnostic potential for osteoarthritis," *Journal of the mechanical behavior of biomedical materials,* vol. 31, pp. 77-85, 2014.

[92] J. Kim, D. Hah, T. Daniels-Race, and M. Feldman, "Clinical probe utilizing surface enhanced Raman scattering," *Journal of Vacuum Science & Technology B,* vol. 32, p. 06FD02, 2014.

[93] P. E. Green, *Fiber optic networks* vol. 993: Prentice Hall Englewood Cliffs, NJ, 1993.

[94] R. L. McCreery, M. Fleischmann, and P. Hendra, "Fiber optic probe for remote Raman spectrometry," *Analytical Chemistry,* vol. 55, pp. 146-148, 1983.

[95] Y. Komachi, H. Sato, K. Aizawa, and H. Tashiro, "Micro-optical fiber probe for use in an intravascular Raman endoscope," *Applied optics,* vol. 44, pp. 4722-4732, 2005.

APPENDIX A. PERMISSION TO REPRINT COPYRIGHTED MATERIAL

NATURE PUBLISHING GROUP LICENSE TERMS AND CONDITIONS

Mar 04, 2016

This is a License Agreement between HsuanChao Hou ("You") and Nature Publishing Group ("Nature Publishing Group") provided by Copyright Clearance Center ("CCC"). The license consists of your order details, the terms and conditions provided by Nature Publishing Group, and the payment terms and conditions.

All payments must be made in full to CCC. For payment instructions, please see information listed at the bottom of this form.

License Number	3822071426371
License date	Mar 04, 2016
Licensed content publisher	Nature Publishing Group
Licensed content publication	Nature
Licensed content title	Imaging in the era of molecular oncology
Licensed content author	Ralph WeissledерandMikael J. Pittet
Licensed content date	Apr 3, 2008
Volume number	452
Issue number	7187
Type of Use	reuse in a dissertation / thesis
Requestor type	academic/educational
Format	electronic
Portion	figures/tables/illustrations
Number of figures/tables /illustrations	1
High-res required	no
Figures	Table 1.1 The comparison of molecular imaging system.
Author of this NPG article	no
Your reference number	None
Title of your thesis / dissertation	NANO COST NANO PATTERNED TEMPLATE FOR SURFACE ENHANCED RAMAN SCATTERING (SERS) FOR IN VITRO AND IN VIVO APPLICATIONS
Expected completion date	Aug 2016
Estimated size (number of pages)	110
Total	0.00 USD

APPENDIX B. PERMISSION TO REPRINT COPYRIGHTED MATERIAL

ROYAL SOCIETY OF CHEMISTRY LICENSE TERMS AND CONDITIONS

Mar 04, 2016

This Agreement between HsuanChao Hou ("You") and Royal Society of Chemistry ("Royal Society of Chemistry") consists of your license details and the terms and conditions provided by Royal Society of Chemistry and Copyright Clearance Center.

License Number	3822110217723
License date	Mar 04, 2016
Licensed Content Publisher	Royal Society of Chemistry
Licensed Content Publication	RSC Advances
Licensed Content Title	Partially embedded gold nanoislands in a glass substrate for SERS applications
Licensed Content Author	Mohammad Tariq Yaseen,Minfeng Chen,Yia-Chung Chang
Licensed Content Date	Oct 27, 2014
Licensed Content Volume Number	4
Licensed Content Issue Number	98
Type of Use	Thesis/Dissertation
Requestor type	academic/educational
Portion	figures/tables/images
Number of figures/tables /images	2
Format	electronic
Distribution quantity	1
Will you be translating?	no
Order reference number	None
Title of the thesis/dissertation	NANO COST NANO PATTERNED TEMPLATE FOR SURFACE ENHANCED RAMAN SCATTERING (SERS) FOR IN VITRO AND IN VIVO APPLICATIONS
Expected completion date	Aug 2016
Estimated size	110
Requestor Location	HsuanChao Hou 275 W roosevelt st APT 1258 BATON ROUGE, LA 70802 United States Attn: HsuanChao Hou
Billing Type	Invoice
Billing Address	HsuanChao Hou 275 W roosevelt st APT 1258

	BATON ROUGE, LA 70802 United States Attn: HsuanChao Hou
Total	0.00 USD

APPENDIX C. PERMISSION TO REPRINT COPYRIGHTED MATERIAL

AIP PUBLISHING LLC LICENSE
TERMS AND CONDITIONS

Mar 04, 2016

All payments must be made in full to CCC. For payment instructions, please see information listed at the bottom of this form.

License Number	3822110598614
Order Date	Mar 04, 2016
Publisher	AIP Publishing LLC
Publication	Journal of Vacuum Science & Technology B
Article Title	Clinical probe utilizing surface enhanced Raman scattering
Author	Jeonghwan Kim,Dooyoung Hah,Theda Daniels-Race, et al.
Online Publication Date	Sep 26, 2014
Volume number	32
Issue number	6
Type of Use	Thesis/Dissertation
Requestor type	Student
Format	Electronic
Portion	Figure/Table
Number of figures/tables	3
Title of your thesis / dissertation	NANO COST NANO PATTERNED TEMPLATE FOR SURFACE ENHANCED RAMAN SCATTERING (SERS) FOR IN VITRO AND IN VIVO APPLICATIONS
Expected completion date	Aug 2016
Estimated size (number of pages)	110
Total	0.00 USD

VITA

Hsuan-Chao Hou was born in 1981 at Kaohsiung, located at the south of Taiwan (R.O.C.). He completed his Bachelor of Science (B.S.) degree in 2004 from Mechatronic Engineering at Hua-Fan University. In 2007, he earned his Master of Science (M.S.) degree from photonic at Feng-Chia University with the topic of "Fabrication of 1×3 Fused Tapered Single-Mode Fiber Polarization Beamsplitters and Small Form Birefringence" for fiber coupler system. He has enrolled as a doctoral program in the division of Electrical and Computer Engineering of the school of Electrical Engineering and Computer Science at Louisiana State University, Baton Rouge, Louisiana since fall 2011. In 2015, he completed his second Master of Science (M.S.) degree from electrical engineering from Louisiana State University. He was interested in optical design, optical conference, optical fiber, Raman Enhancement, and MEMS technology. His dissertation "NANO COST NANO PATTERNED TEMPLATE FOR SURFACE ENHANCED RAMAN SCATTERING (SERS) FOR IN VITRO AND IN VIVO APPLICATIONS" was guided by Dr. Feldman until he earned his Ph.D. degree.